Mass Loss from Red Giant Stars in Globular Clusters

A PhD thesis

By Szabolcs Mészáros

Department of Optics and Quantum Electronics
University of Szeged
Faculty of Natural Sciences and Informatics

Thesis Advisor: Dr. Andrea K. Dupree

Harvard-Smithsonian Center for Astrophysics
Cambridge, USA

Advisor: Dr. József Vinkó

Department of Optics and Quantum Electronics
University of Szeged, Hungary

PhD School in Physics
University of Szeged, Hungary
2009

Contents

Acronyms used in the text:

ADU — Analog Digital Unit
AGB — Asymptotic Giant Branch
CMD — Color Magnitude Diagram
HB — Horizontal Branch
HRD — Hertzsprung-Russell Diagram
ICM — Intracluster Medium
ISM — Interstellar Medium
LTE — Local Thermodynamic Equilibrium
MMT — Multi Mirror Telescope
MS — Main Sequence
non-LTE — non-Local Thermodynamic Equilibrium
RGB — Red Giant Branch

Abstract

Mass loss plays a significant role in stellar evolution. The stellar wind of a red giant star is many times stronger than that of a main sequence star. These stars can be found in great numbers in globular clusters, which makes it possible to observe hundreds of them at the same time. In my work, I obtained high resolution spectra of red giant stars in three globular clusters, created semi-empirical models of the Hα line to derive mass loss rates, and examined its relation to the physical parameters of red giant stars.

After a brief introduction in Section 1, I present my observations in Section 2. Observations of a total of 297 red giant stars in M13, M15 and M92 were obtained in 2005 May, 2006 May, and 2006 October with the Hectochelle on the Multi Mirror Telescope (MMT) at a resolution of 34,000. Echelle orders containing Hα and Ca II H & K are used to identify emission lines and line asymmetries characterizing motions in the extended atmospheres and look for possible metallicity dependences. The results of this thesis are presented in Mészáros et al. (2008, 2009a,b).

Discussion of radial, bisector velocities and line statistics is presented in Sections 3 and 4. On the red giant branch, emission in Hα generally appears in metal-poor stars with $T_{\rm eff} < 4500$ K and $\log (L/L_{\odot}) > 2.75$, suggesting that appearance of emission wings is independent of stellar metallicity. The line-bisector for Hα reveals the onset of chromospheric expansion in stars more luminous than $\log (L/L_{\odot}) \sim 2.5$ in all clusters, and this outflow velocity increases with stellar luminosity. However, I found that the coolest giants in the metal-rich globular cluster M13 show reduced outflow in Hα probably due to decreased $T_{\rm eff}$ and changing atmospheric structure. Many stars lying low on the AGB show exceptionally high outflow velocities (up to 10$-$15 km s^{-1}) and more velocity variability (up to 6$-$8 km s^{-1}), than red giant branch stars of similar apparent magnitude. Dusty stars identified as AGB stars from *Spitzer* Space Telescope infrared photometry have very similar Hα profiles to those of RGB stars without dust. If substantial mass loss creates the circumstellar shell responsible for infrared emission, such mass loss must be episodic. The Ca II K_3 outflow velocities are larger than shown by Hα at the same luminosity and signal accelerating outflows in the chromospheres. Stars clearly on the AGB show faster chromospheric outflows in Hα than RGB objects. While the Hα velocities on the RGB are similar for all metallicities, the AGB stars in the metal-poor M15 and M92 have higher outflow velocities than in the metal-rich M13. Comparison of these chromospheric line profiles in the paired metal-poor clusters, M15 and M92 shows remarkable similarities in the presence of emission and dynamical signatures, and does not reveal a source of the 'second-parameter' effect.

I also present chromospheric model calculations of the Hα line for selected red giant branch and asymptotic giant branch stars to derive mass loss rates in Section 5. These stars show strong Hα emissions and blue-shifted Hα cores signaling that mass outflow is present. Outflow velocities of 3$-$19 km s^{-1}, larger than indicated by Hα profiles, are needed in the upper chromosphere to achieve good agreement between the model spectra and the observations. The resulting mass loss rates range from 0.6×10^{-9} to 5×10^{-9} $M_{\odot}$ yr^{-1}. Stars in the more metal-rich M13 have higher mass loss rates by a factor of $\sim$2 than in the metal-poor clusters M15 and M92. A fit to the mass loss rates is given by: $\dot{M}[M_{\odot}\ {\rm yr}^{-1}] = 0.092 \times L^{0.16}[L_{\odot}] \times T_{\rm eff}^{-2.02} \times A^{0.37}$ where $A=10^{[Fe/H]}$. Multiple observations of stars revealed one object in M15, K757, in which the mass outflow increased by a factor of 6 between two observations separated by 18 months.

Chapter 1

Introduction

1.1 Stellar Evolution

Mass loss occurs through the lifetime of a star, and it greatly affects the stellar evolution especially at the late stages. The processes of mass loss and its relation to stellar evolution is currently not fully understood.

The evolution of stars can be understood using the Hertzsprung-Russell diagram (HRD). In an HRD, the luminosity of stars is plotted as a function of effective temperature. The HRD of our Milky Way consists of stars clustering around two main regions; one is the main sequence (MS) and one is the giant branch. Such an HRD were constructed with the Hipparcos satellite and can be seen in Figure 1.1. On the MS, the existence of a simple relation between the luminosity and effective temperature is due to one important parameter: the mass of the star. More massive stars are hotter and more luminous in the MS than stars with lower mass. The existence of the MS in due to the nuclear reactions that convert hydrogen into helium in the core of stars. The analog of HRD is the color-magnitude diagram (CMD). In this diagram, the horizontal axis contains a color (usually B−V, V−I) which relates to effective temperature, while the absolute magnitude is plotted on the vertical axis.

During pre-main-sequence evolution stars evolve from interstellar clouds due to gravitational collapse. This phase is characterized by two time scales: the free-fall time scale at the beginning, and the Kelvin-Helmholtz time scale at later phases of contraction. Once the hydrogen fusion starts in the core of the star, the main-sequence evolution begins on the time scale of nuclear reactions. The main-sequence, and post-main-sequence evolution of a $1M_{\odot}$ mass and metal-poor[1] star in the HRD is plotted in Figure 1.2.

The nuclear time scale is on the order of 10^{10} years. A low-mass star spends nearly 80−90% of its life on the MS. In this stage, the luminosity, radius and effective temperature increases slowly, but steadily. In the core of a low mass star the energy is created via

[1]metal-poor stars contain less heavy elements (Z>2) than the Sun.

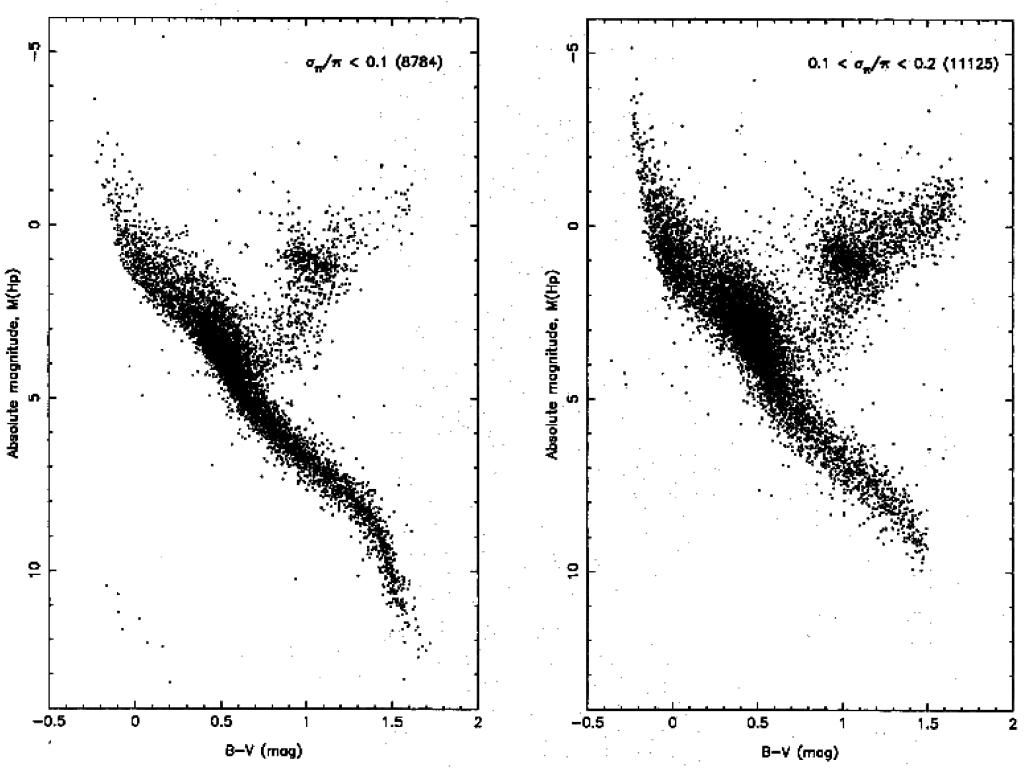

Figure 1.1: *The observational HRD constructed from the preliminary Hipparcos catalog (Perryman et al., 1995). Left panel: The HRD of 8784 stars with less than 10% error in their parallaxes (distance from Sun is smaller than 60−70 pc). Right panel: The HRD of 11125 stars with errors between 10% and 20% in their parallaxes (distance from Sun is between 70 and ∼140 pc).*

proton-proton (pp) cycles. The pp chain converts hydrogen to helium, while the mean molecular weight of the core increases. According to the ideal gas law, if the density or temperature of the core also increases, the gas pressure will not be enough to support the overlying regions of the star. Thus, the core must be compressed and, as a result, the density of the core increases and gravitational potential energy is released, which heats up the core. The pp chain reaction depends on temperature and increases as T^4, which more than offsets the decrease of the mass fraction of hydrogen in the core. This results in an increase of the effective temperature and luminosity. During the MS evolution of low-mass stars the mass loss can be ignored, the mass of the star remains nearly constant.

Eventually, as evolution continues, the hydrogen in the core will be depleted and the energy generation from pp chains stops. However, the core temperature is now so high, that the nuclear fusion becomes possible in a thick hydrogen-burning shell around a small, predominantly helium core. Now, the luminosity is being generated in this thick shell and eventually becomes larger than what was produced by the core during the core-burning phase. Some of this energy goes to expand the inner regions of the star, which results in a lower effective temperature with nearly constant luminosity (Figure 1.2). This hydrogen-burning shell continuously producing helium, thus the mass of the isothermal helium core

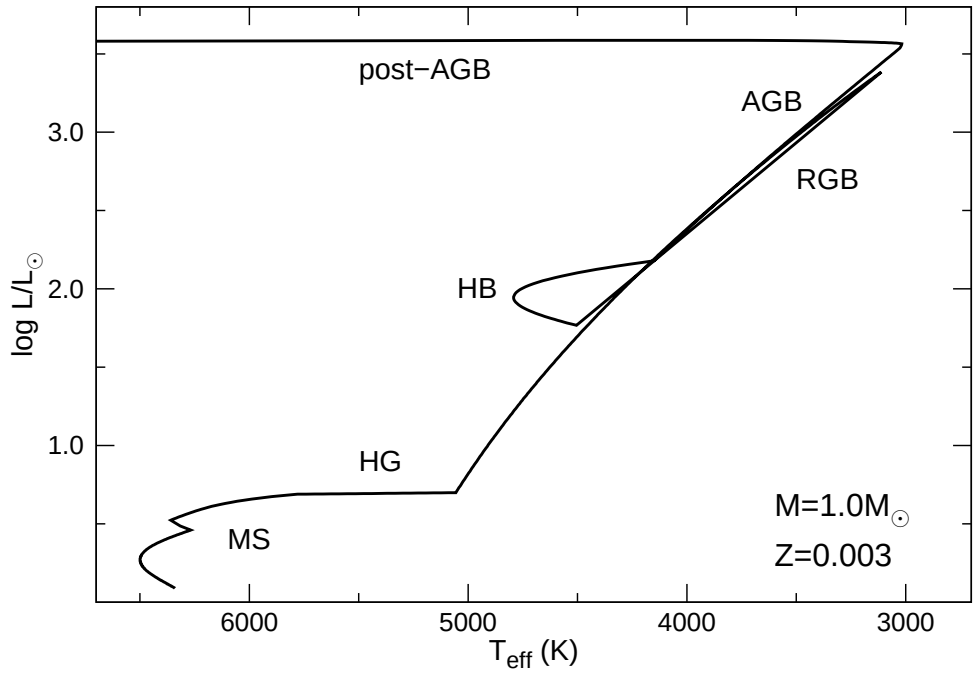

Figure 1.2: *Evolutionary track of a $M=1M_{\odot}$ and Z=0.003 star on the HRD calculated with the Single Star Evolution program developed by Hurley (2000). The stages labeled are the following in the order of evolution: 1. MS: main sequence, 2. HG: Hertzsprung gap, 3. RGB: red giant branch, 4. HB: horizontal branch, 5. AGB: asymptotic giant branch, 6. post-AGB: evolution after the asymptotic giant branch.*

increases.

This phase of evolutions ends when the isothermal core becomes so massive that it cannot support the pressure of material above it. This happens when the mass of the helium core reaches the Schönberg-Chandrasekhar limit, which is around 10% of the star's mass. When the mass of the core exceeds this limit it collapses on the Kelvin-Helmholtz time scale, and the star evolves very rapidly compared to the MS evolution. This occurs in the Hertzsprung gap (HG) on the HRD (Figure 1.2). The release of gravitational potential energy causes the core temperature to rise, and at the same time, the temperature and the density of the hydrogen-burning shell increase. This forces the star to expand rapidly. This continuous until the effective temperature reaches that of the Hayashi track (the path that a fully convective pre-main-sequence stars follows as it approaches the MS).

As the core continuous to contract, the energy production increases significantly from the hydrogen-burning shell. In this phase the evolution proceeds vertically in the HRD, until the star reaches the red giant branch (RGB), and significant mass loss starts by stellar winds. At this time, the core becomes strongly electron-degenerate and when the core temperature reaches 10^8 K to initiate the triple alpha process, the ensuing energy is explosive. This is the helium core flash. However, this energy release lasts for only a

few seconds and never reaches the surface, because the overlying regions absorb it. This phase is the first time when significant amount of mass loss occurs from the surface. Due to the generated energy, the core becomes non-degenerate decreasing the density and temperature, and lowering the reaction rate of the triple alpha process. The star reaches the horizontal branch (HB) phase.

The hydrogen-burning shell continues to produce helium, and the mean molecular weight in the core increases to the point where the core starts to contract while the surface layers expand and cool. The energy required to increase the gravitational potential energy of the hydrogen-burning shell lowers the luminosity. During the phase of HB, almost all stars develop instabilities in their outer envelopes, resulting in periodic pulsations and variations in luminosity, effective temperature and radius.

At the end of the HB phase, the helium core becomes exhausted, just like the hydrogen core did at the end of the MS. As the core temperature further increases, a thick helium-burning shell develops above the core, but below the hydrogen-burning shell. When the helium-burning shell starts to produce energy, the outer envelopes expand and cool, shutting down the hydrogen-burning shell. This shell will eventually reignite and the narrowing helium-burning shell begins to turn on and off periodically as the hydrogen-burning shell dumps helium into deeper regions. This phase is called the asymptotic giant branch (AGB). As the mass of the helium shell increases, it becomes degenerate, but when the temperature starts to increase, a helium shell flash occurs, driving the hydrogen shell outwards and cooling it down. Eventually the burning in the helium shell stops and the whole process starts again. The period between these pulses is a couple of hundreds of thousands of years for low-mass stars.

Mass loss becomes even more significant in the AGB phase, than before. Our understanding of mass loss processes are poor, but it is suggested by many that it is linked to the helium shell flashes. Other proposed mechanisms come from the high luminosity and/or low surface gravity of these stars. Mass loss becomes more and more important as the star evolves in the AGB phase, because as the mass of the star decreases, the surface gravity decreases as well and the surface material becomes less tightly bound. The result of the mass loss is an increasement in the interstellar medium (ISM) and intracluster medium (ICM). Because of the low surface temperature of these stars and the stellar wind being rich in carbon and oxygen, dust production can be significant.

Eventually the mass loss becomes so strong and so much material will be lost, that the helium and hydrogen-burning shells shut down. The previously expanded shells becomes optically thin, revealing the dense core of the star, which purely consists carbon and oxygen. This central objects will then cool and become a white dwarf star, which is the final stage of the low-mass star evolution.

1.2 Globular Clusters

A globular cluster is a spherical collection of stars that orbits a galaxy. These objects are tightly bound by gravity, which gives them their spherical shapes and relatively high stellar densities toward their centers. The Milky Way possesses about 160 known globular clusters. These star clusters play a very important role in astrophysics, mainly in stellar evolution.

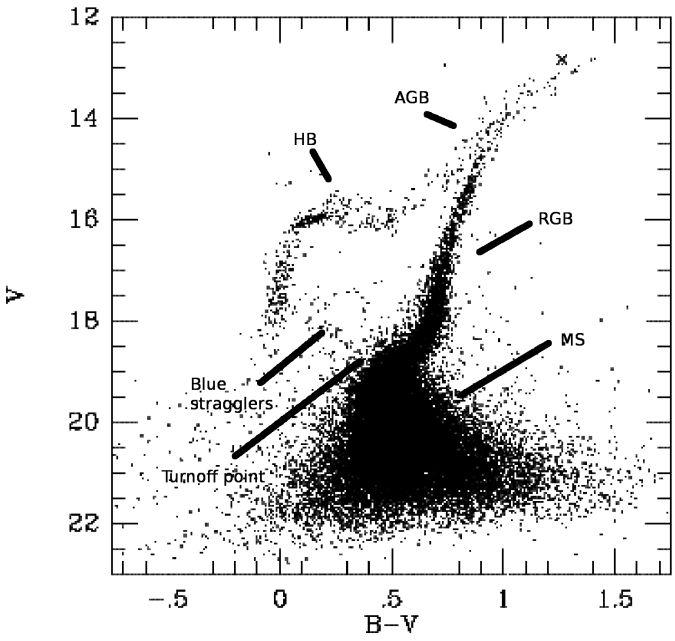

Figure 1.3: *Color-magnitude diagram of stars in M15. The photometry was taken by the WFPC2 camera on the Hubble Space Telescope (van der Marel et al., 2002).*

It is believed that all stars in a globular cluster were produced at the same time, only 2−3 billion years after the Big Bang. These clusters are very metal-poor and one of the oldest objects in the Universe. They are free of gas and dust and it is presumed that all of the gas and dust was long ago turned into stars, although some ICM still remains in some clusters, probably coming from stellar winds of AGB stars (see Section 1.3). Their size is usually couple of hundreds of light years across, and they consists of from several hundreds of thousands of stars to several million.

When the stars of a globular cluster are plotted on the HRD, nearly all of the stars fall upon a relatively well defined curve (Figure 1.3). This differs from the HRD of stars in the Milky Way (Figure 1.1), which consists of stars of different ages and origins. The shape of the curve for a globular cluster is characteristic of stars that were formed at approximately the same time with nearly the same metallicity, differing only in their initial mass. For a population of stars with the same age, as the population ages, the more massive stars will begin to leave the MS, which results in the turnoff point on the

MS moving to lower luminosities. Such an evolutionary trend can be used to estimate the age of a stellar population, because the turn off occurs when nearly all the central fuel is gone in the core of the star. Blue stragglers are stars that are hotter and bluer than other cluster stars having the same luminosity. These stars appear to be merging binary stars.

Two clusters with the same metallicity have to have two very similar HRDs, but observation show that the HB can be very different even in this case.

1.2.1 The Second Parameter Problem

The well-known second parameter problem in globular clusters (Sandage & Wildey, 1967), in which a parameter other than metallicity, affects the morphology of the horizontal branch, remains unresolved. Metallicity, as first noted by Sandage & Wallerstein (1960), remains the principal parameter, but pairs of clusters, with the same metallicity, display quite different horizontal branch morphologies thus challenging the canonical models of stellar evolution and leading to the need for a 'Second Parameter'. Cluster ages have been examined in many studies (Searle & Zinn, 1978; Lee et al., 1994; Stetson et al., 1996; Lee & Carney, 1999; Sarajedini, 1997; Sarajedini et al., 1997) and in addition, many other suggestions for the 'second parameter(s)' have been proposed, including: total cluster mass; stellar environment (and possibly free-floating planets); primordial He abundance; post-mixing surface helium abundance; CNO abundance; stellar rotation; and mass loss (Catelan, 2000; Catelan et al., 2001; Sills & Pinsonneault, 2000; Soker et al., 2001; Sweigart, 1997; Buonanno et al., 1993; Peterson et al., 1995; Buonanno et al., 1998; Recio-Blanco et al., 2006). Many authors (Vandenberg et al., 1990; Lee et al., 1994; Catelan, 2000) have proposed that more than one second parameter may exist in addition to age. One parameter may be mass loss which, as Catelan (2000) notes, remains an 'untested second-parameter candidate'.

An example of paired second-parameter clusters is M15 and M92 ([Fe/H]=−2.26 and −2.28 respectively). Although the metallicities of these two clusters are the same (Sneden et al., 2000), their horizontal branches differ (Buonanno et al., 1985). M92 has a brighter (by about one magnitude) and redder blue HB extension than M15. The color magnitude diagrams of this pair were examined in detail by Cho & Lee (2007). They found that the difference in the HB morphology between the two is probably not a result of deep mixing in their red giant branch sequences, because no significant 'extra stars' were found in their observed RGB luminosity functions compared to the theoretical RGB luminosity functions. Sneden et al. (2000) found that Si, Ca, Ti, and Na abundance ratios of the red giants are nearly the same in both clusters, only the [Ba/Ca] ratio shows a large scatter and the mean value in M15 is twice that found in M92. These studies eliminate deep mixing and subtle abundance variations as possible second parameters. Mass loss

is examined in this thesis in Section 4.3. Detailed observations of red giant stars in M15 are contained in Mészáros et al. (2008), but the comparison between M15 and M92 is described in Mészáros et al. (2009a,b).

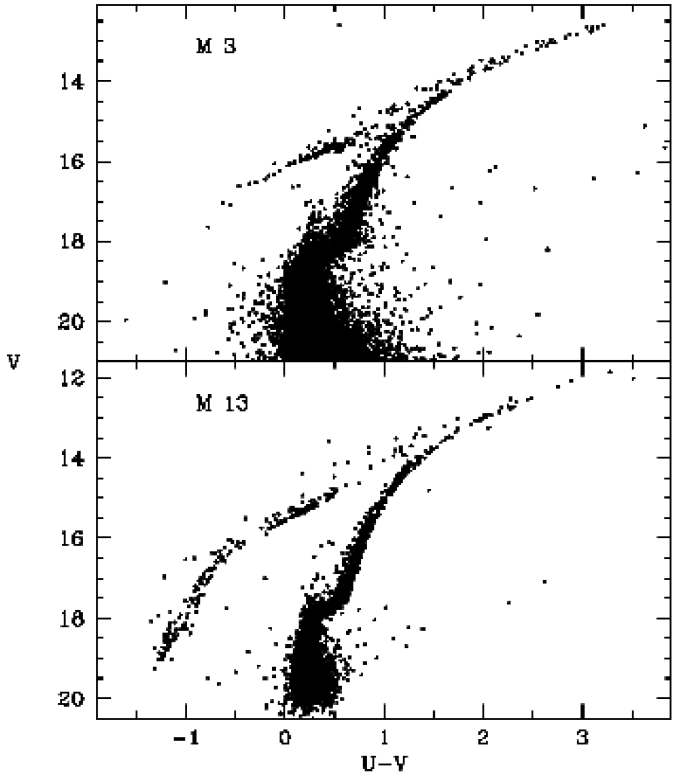

Figure 1.4: *Color-magnitude diagram of stars in the second-parameter clusters M13 and M3. Note the significant difference between the HB of these two clusters. The photometry was taken by the Hubble Space Telescope (Ferraro et al., 1997).*

M13 ([Fe/H]=−1.54) is one of the most studied second-parameter globular clusters. M13 and M3 are almost identical in most respects (metallicity, age, chemical composition), but there are dramatic differences in both the HB and blue straggler populations (Figure 1.4). Analysis of both clusters' CMDs (Ferraro et al., 1997) with the Hubble Space Telescope revealed that neither age nor cluster density, two popular second-parameter candidates, is likely to be responsible for the differences in these clusters. From the analysis of high-resolution, high signal-to-noise ratio spectra of six RGB stars in M3 and three in M13, Cavallo & Nagar (2000) found that the [Al/Fe] and [Na/Fe] abundances increase toward the tip of the RGB. They concluded that the data for both clusters are consistent with deep mixing as a second parameter. Later, Johnson et al. (2005), from medium−resolution spectra of more than 200 stars in M3 and M13, concurred that deep mixing is the best candidate for second parameter in this pair of clusters. Caloi & D'Antona (2005) also examined the second-parameter problem in M3 and M13 in detail and proposed that the overall difference between M3 and M13 CMD morphologies is due

to the different helium content. Since M13 does not have a red clump in its horizontal branch they suggested that it represents an extreme case of self-enrichment of helium, which might come from the massive asymptotic giant branch stars (AGB) in the first ∼100 Myr of the cluster life.

A multivariate study of the CMDs for 54 globular clusters was carried out by Recio-Blanco et al. (2006) from Hubble Space Telescope photometry to quantify the parameter dependencies of HB morphology. They found that the total cluster luminosity (therefore the total mass) has the largest impact on the HB morphology, and as Caloi & D'Antona (2005) speculated, there may be enrichment of helium from an earlier population of stars. D'Antona et al. (2002) modeled the evolution of globular cluster stars and showed that different choices of mass−loss rate affect the distribution of stars on the HB.

1.3 Mass Loss

Although stellar evolution theory predicts that low-mass Population II stars ascending the red giant branch (RGB) for the first time must lose mass (Renzini, 1981; Sweigart et al., 1990), few observations have identified the ongoing mass loss process. Evidence from the period-luminosity relation for RR Lyrae stars suggests that the luminosity variations can be accommodated theoretically if mass loss $\sim 0.2 - 0.4\ M_{\odot}$ has occurred (Fusi Pecci et al., 1993; Christy, 1966). Iben & Rood (1970) conjectured that mass loss on the RGB may increase with metallicity in order to account for colors on the horizontal branch.

For stellar evolution calculations, the mass loss rate from late-type giants is frequently described by "Reimers' law" (Reimers, 1975, 1977) given as $\dot{M}[M_{\odot}yr^{-1}] = \eta \times L_* \times R_*/M_*$, where L_*, R_*, and M_* are the stellar luminosity, radius, and mass in solar units, and η is a fitting parameter equal to 4×10^{-13}. This approximation is based on a handful of luminous Population I stars.

Schröder & Cuntz (2005) offered another semi-empirical relation for the mass loss rate from cool stars by assuming a wave-driven wind and introducing gravity and effective temperature into the formulation. They found consistency with calculations of evolutionary models for abundances as low as [Fe/H]=−1.27 although metallicity does not enter as a parameter in their formulation.

1.3.1 Direct Evidence

Direct observations of the ongoing mass loss process in globular clusters only became possible in the past decade using high resolution spectroscopy and infrared imaging from space.

Circumstellar CO emission in M-type irregular and semi-regular asymptotic giant branch (AGB)-variables implies mass loss rates on the AGB $\sim 10^{-7} - 10^{-8}\ M_{\odot}\ yr^{-1}$

(Olofsson et al., 2002). Indirect evidence of mass loss processes would be detection of an intracluster medium. These efforts have been marginally successful. Diffuse gas ($< 1\ M_{\odot}$) was suggested in NGC 2808 through the detection of 21−cm H line emission (Faulkner et al., 1991), but has remained unconfirmed. Ionized intracluster gas was found in the globular cluster 47 Tucanae by measuring the radio dispersion of millisecond pulsars in the cluster (Freire et al., 2001). The central electron density was derived ($n_e = 0.067\ \pm 0.0015$ cm^{-3}) and found to be two orders of magnitude higher than the ISM in the vicinity of 47 Tuc (Taylor & Cordes, 1993). Freire et al. (2001) determined the electron density in M15 using four millisecond pulsars to be higher ($n_e \sim 0.2$ cm^{-3}) than in 47 Tuc.

Indirect evidence of mass loss processes comes also from infrared observations. Origlia et al. (2002) using ISOCAM images found a mid-IR excess associated with giants in several globular clusters and attributed to dusty circumstellar envelopes. The first detection of intracluster dust in M15 was made by Evans et al. (2003) from the analysis of far infrared imaging data obtained with the ISO instrument ISOPHOT. van Loon et al. (2006) also presented a tentative detection of 0.3 $M_{\odot}$ of neutral hydrogen in M15. Smith et al. (1995) placed an upper limit of 0.4 $M_{\odot}$ for the molecular gas in M15 from CO observations with the 15-m James Clerk Maxwell Telescope on Mauna Kea. Using the *Spitzer* Space Telescope, Boyer et al. (2006) detected a population of dusty red giants near the center of M15. Observations with the Multiband Imaging Photometer for *Spitzer* (MIPS) also revealed the intracluster medium discovered by Evans et al. (2003) near the core of the globular cluster. As Origlia et al. (2002) noted, the infrared detections may only be tracing the outflowing gas and may not be related to the driving mechanisms for the wind. More recently Origlia et al. (2007) identified dusty RGB stars in 47 Tuc and derived an empirical mass loss law for Population II stars. Mass loss rates derived from these observations showed that the mass loss increases with luminosity and possibly it is episodic.

1.3.2 Spectroscopic Studies

High resolution stellar spectroscopy allows the direct detection of mass outflow from the red giants themselves. Emission in the wings of Hα lines in the spectra of globular cluster red giants was first described in detail by Cohen (1976). Later observations revealed that emission in Hα is common in globular clusters and night-to-night variations can occur (Mallia & Pagel, 1981; Peterson, 1981, 1982; Cacciari & Freeman, 1983; Gratton et al., 1984). These studies have shown that most of the stars brighter than $\log (L/L_{\odot}) \approx 2.7$ exhibit Hα emission wings.

The emission itself is likely not a direct indicator of mass loss, because emission can arise from an optically thick stellar chromosphere surrounding the star (Dupree et al.,

1984). Variation of the strength of emission can also be affected by stellar pulsation (Smith & Dupree, 1988). Better mass flow indicators in the optical are the line coreshifts or asymmetries of the Hα or Ca II H&K profiles and emission features. Red giants in globular clusters (M22 and Omega Centauri) were found to have velocity shifts less than 14 km s^{-1} in the cores of Hα relative to the photospheric lines (Bates et al., 1990, 1993). These results were similar to metal-poor field giants, where only giants brighter than $M_V = -1.7$ have emission wings and the line shifts were $<$ 9 km s^{-1} (Smith & Dupree, 1988) indicating very slow outflows and inflows in the chromosphere.

For globular clusters, Lyons et al. (1996) discussed the Hα and Na I D line profiles for a sample of 63 RGB stars in M4, M13, M22, M55, and ω Cen. The coreshifts were less than 10 km s^{-1}, much smaller than the escape velocity from the stellar atmosphere at 2 R_* ($\approx 50-70$ km s^{-1}). Dupree et al. (1994) studied 2 RGB stars in NGC 6752 and found that the Ca II K and Hα coreshifts were also low (less than 10 km s^{-1}). However, asymmetries in the Mg II lines showed a stellar wind with a velocity of $\approx$ 150 km s^{-1}, indicative of a strong outflow in cluster giants and metal-poor field stars (Dupree et al., 1994, 2007; Smith & Dupree, 1988). However, Mg II lines are formed higher in the atmosphere than Hα and Ca II K, which suggests that the stellar wind becomes detectable near the top of the chromosphere. These Mg II lines showed strong outflow velocities ($\approx$ 150 km s^{-1}). Also, high outflow velocities, ($30-140$ km s^{-1}), were found in the He I λ10830 absorption line of metal-poor red giant stars of which 6 are in M13 (Dupree et al., 1992; Smith et al., 2004; Dupree et al., 2009). These outflow velocities are frequently higher than the central escape velocities from globular clusters, namely $20-70$ km s^{-1} (McLaughlin & van der Marel, 2005).

A detailed study was carried out by Cacciari et al. (2004), who observed 137 red giant stars in NGC 2808. Most of the stars brighter than log $(L/L_\odot) = 2.5$ clearly showed emission wings in Hα . The velocity shift of the Hα line core compared to the photosphere is less than $\approx$ 9 km s^{-1} . Outward motions were also found in both Na I D and Ca II K profiles. Another detailed study of Hα line and Ca II K profiles were carried out with the Hectochelle on the MMT at a resolution of 34,000 by Mészáros et al. (2008, 2009a) in M13, M15 and M92. These results are discussed in this thesis in Section 2, 3 and 4.

1.4 Models for Mass Loss

Semi-empirical modeling of spectral features to derive mass loss rates are quite rare in the literature. These kind of studies are the only ones, where the mass loss rate can be determined directly from the spectrum of stars.

In order to evaluate the mass flow, detailed non-LTE modeling with semi-empirical atmospheres is necessary to reproduce the optical line profiles and infer the mass loss rates

from the stars. Such non-LTE modeling was first carried out by Dupree et al. (1984). They showed that the emission wings of the Hα line found in metal-deficient giant stars can arise naturally from an extended, static chromosphere, and emission asymmetry and shifts in the Hα core indicate mass loss. Spherical models with expanding atmospheres suggested the mass loss rates are less than 2×10^{-9} $M_\odot$ yr^{-1} a value which is less than predicted by the Reimer's relationship.

McDonald & van Loon (2007) calculated mass loss rates of two stars in M15 by modeling the Hα and Ca II K lines with simple LTE approximations. They found mass loss rates of several times 10^{-8} and $10^{-7}M_\odot$ yr^{-1}, but the use of LTE models for a chromosphere can not be considered reliable.

Mauas et al. (2006) computed semi-empirical Hα and Ca II K profiles for 5 RGB stars in NGC 2808 including non-LTE effects in spherical coordinates. Their line profiles fit the observations when an outward velocity field is included in the model chromosphere, in agreement with previous calculations (Dupree et al., 1984). The derived mass loss rates exhibited a large range around 10^{-9} $M_\odot$ yr^{-1}. Outflow velocities from 10 km s^{-1} up to 80 km s^{-1} were needed by Mauas et al. (2006) in order to match the observed line profiles.

Mészáros et al. (2009b) presented chromospheric model calculations of the Hα line for selected RGB and AGB stars in M13, M15, and M92 to derive mass loss rates. These results are discussed in Section 5.

1.5 Goals

This thesis discusses high-resolution spectroscopy of the Hα and Ca II H&K lines of red giant stars in M15 ([Fe/H]=−2.26), M13 ([Fe/H]=−1.54) and M92 ([Fe/H]=−2.28) (Mészáros et al., 2008, 2009a). The deep sample of M13, M15, and M92 giants offers a good comparison to other studies of the more metal rich cluster NGC 2808 ([Fe/H]=−1.15) (Cacciari et al., 2004). The high resolution spectrograph Hectochelle gives an excellent opportunity of determine the line bisectors of the Hα line and explore the mass motions in the chromosphere of these stars.

Detailed study of these four clusters allows the examination of a possible dependence between the average cluster metallicity and characteristics of Hα and Ca II K emission, and diagnostics of mass outflow. Observations with the same instrument of the second-parameter pair M15 and M92 offer a good comparison to examine mass loss as a possible second parameter.

I also selected a sample of giant stars to model whose spectra have been obtained previously with Hectochelle (Mészáros et al., 2008, 2009a). They span a factor of 5 in metallicity (from [Fe/H]=−1.54 to −2.28) and a factor of 6 in luminosity [from log $(L/L_\odot)$ =2.57 to 3.38]. Five stars have been observed more than once.

The observation technique, target selection and data reduction is explained in Section 2. Section 3 describes the line statistics, radial velocity measurements and the line bisector characteristics. Section 4 discusses the appearance of Hα and Ca II K emission and bisectors on the CMD. Section 5 contains the details of the non-LTE models in both the static and expanding versions, and compares the calculations with Hα line profiles, and the construction of a mass loss relation and its dependence on temperature, luminosity, and abundance.

Chapter 2

Observations

In this Chapter, I describe how the observations were obtained during 2005 and 2006. The first section contains a brief summary on the Hectochelle spectrograph and the target selection criteria. The second section explains the steps of data reduction in IRAF[1].

2.1 Target Selection

Observations of a total of 297 red giant stars in M13, M15 and M92 were obtained in 2005 May, 2006 May, and 2006 October with the Hectochelle on the Multi Mirror Telescope (MMT) (Szentgyorgyi et al., 1998). The Hectochelle is a fiber-fed, bench mounted echelle spectrograph, which operates on the MMT in wide field mode covering 1 degree on the sky. Hectochelle uses 240 fibers and each of them subtends ~ 1.5 arcsec. These fibers can be placed ~ 2 arcsec apart across the field of view, and can be positioned with an accuracy of 25 μm. Hectochelle operates in a is a single-order mode, when a spectral order is isolated with a bandpass filter, giving $\sim$150 Å width in each order. This way, in optimal case, 240 stars can be observed at the same time having the same spectral range for each star with a resolution about 34,000 in each filter. The CCDs positioned in the focal plane are cooled to -120 Celsius with liquid nitrogen and consist of a pair of 2k $\times$ 4.5k devices with 13.5 μm pixels.

The apparent diameter of M15 is only $\sim$ 12 arc minutes, so that about $50-60$ red giants could be measured in each configuration. The apparent diameter of M13 is $\sim$15 arc minutes, and about $60-70$ red giants in the globular cluster could be selected in the field of view. The apparent diameter of M92 is smaller, and only $30-40$ stars could be measured with one configuration. Observations of a total of 110 red giant stars in M15 were made in 2005 May, 2006 May, and 2006 October, in four different fiber configurations. Two separate input fiber configurations for different stars were made for M13 and M92. A total of 123 different red giant stars in M13 and 64 red giants in M92 were observed in

[1] http://iraf.noao.edu/

2006 March and 2006 May.

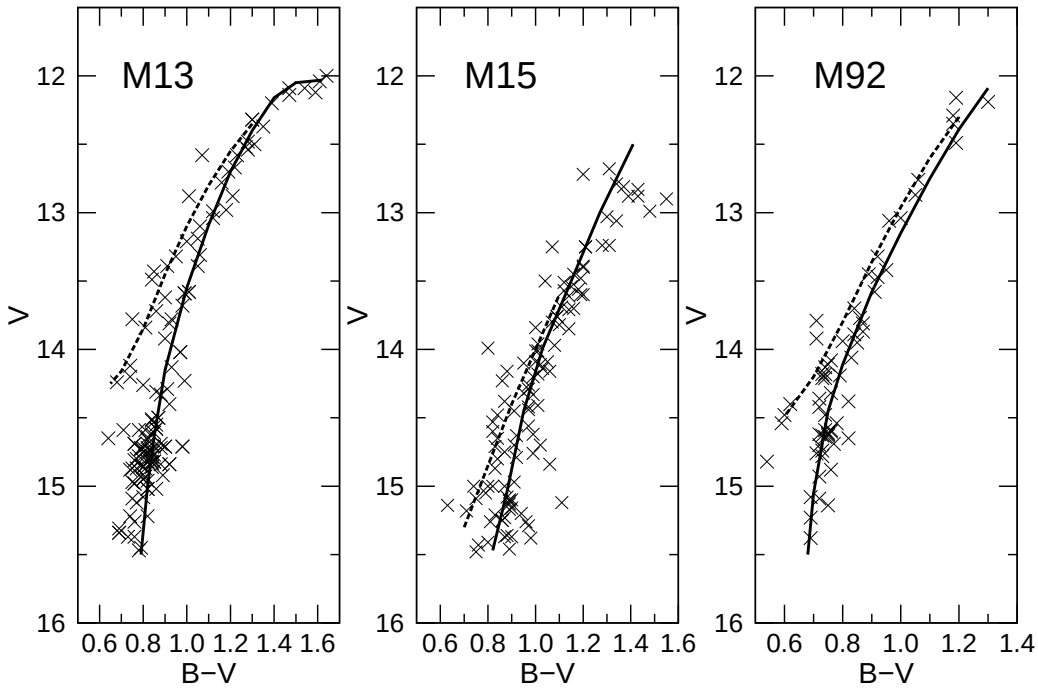

Figure 2.1: *Color-magnitude diagram for all stars observed in M13, M15, and M92. The solid line shows the fiducial curve of the RGB; the dashed line shows the fiducial curve of the AGB for M13 and M92 taken from observations of Sandage (1970), for M15 taken from observations of Durrell & Harris (1993). The absolute magnitudes were calculated using the apparent distance modulus* $(m-M)_V = 14.48$ *for M13,* $(m-M)_V = 15.37$ *for M15, and* $(m-M)_V = 14.64$ *for M92 from Harris (1996).*

The requirement that fibers cannot be placed closer than 2 arcsec apart further constrains the target selection, especially near the cluster's core. To ensure that large number of objects are observed and reduce the possibility of blends, stars from the outer regions of the clusters were mainly selected. In addition, I wanted to search for variability which led to multiple visits for many targets over the 17 month span in M15, thus several stars were chosen multiple times. Software (*xfitfibs*[2]) has been developed at CfA to optimize the fiber configuration with specified priorities and requirements.

Targets brighter than 15.5 magnitude with a high probability ($> 95\%$) of membership were chosen from the catalog of Cudworth (1976) for M13 and M15, and from Cudworth & Monet (1979) for M92 to provide smooth coverage of the RGB and AGB within the constraint of the fiber placement on the sky. The color magnitude diagram (CMD) of the observed cluster members can be seen in Figure 2.1 and they are listed in Appendix Table 7.1 for M15, in Appendix Table 7.2 for M13, and in Appendix Table 7.3 for M92. Coordinates of the stars were taken from the 2MASS catalog (Skrutskie et al., 2006) and used to position the fibers. Additional targets from Cudworth's list with lower

[2]http://www.cfa.harvard.edu/∼john/xfitfibs/

Table 2.1. Hectochelle Observations of M13, M15, and M92

Date (UT)	Total exp. (s)	Wavelength (Å)	Filter Name	Number of Observed Stars
2006 March 14 (M13, Field 1)	3×2400	6475−6630	OB25	70
2006 March 16 (M13, Field 1)	3×2400	3910−3990	Ca41	70
2006 March 16 (M13, Field 1)	1×2400	5150−5300	RV31	65
2006 May 10 (M13, Field 2)	3×2400	6475−6630	OB25	70
2006 May 10 (M13, Field 2)	3×2400	3910−3990	Ca41	63
2006 May 10 (M13, Field 2)	1×2400	5150−5300	RV31	65
2005 May 22 (M15, Field 1)	3×1200	6485−6575	OB25	53
2005 May 23 (M15, Field 1)	3×1200	3910−3990	Ca41	53
2006 May 11 (M15, Field 2)	3×2100	6475−6630	OB25	54
2006 October 4 (M15, Field 3)	3×2100	6475−6630	OB25	58
2006 October 7 (M15, Field 4)	3×2100	6475−6630	OB25	50
2006 May 7 (M92, Field 1)	3×2400	6475−6630	OB25	42
2006 May 7 (M92, Field 1)	3×1800	5150−5300	RV31	40
2006 May 8 (M92, Field 1)	3×2400	3910−3990	Ca41	41
2006 May 9 (M92, Field 2)	3×1800	6475−6630	OB25	36
2006 May 9 (M92, Field 2)	3×2400	3910−3990	Ca41	36

membership probability and field targets from the 2MASS catalog were included for M15.

During the first observations in 2005 few fibers were positioned on the sky, because it was believed that only 20−30 apertures are enough to monitor the sky intensity in the field of view. After the first reductions it turned out that many more sky fibers are necessary (see next Section 2.2), thus in later observations additional field targets and stars with low membership probability were neglected, and the remaining fibers ($\sim$ 150−200) were positioned on the sky. The sky fibers were equally distributed in the observed field to cover a large area around the clusters omitting the cluster core. Exposure times varied between 20 and 40 minutes, which gave a S/N$\sim$15 for the faintest objects. 40 minute exposure times were crucial for the Ca41 filter, because the measured flux is very small for red giant stars in the blue region of the spectrum.

Since Hectochelle is a single-order instrument, three orders were selected with order-separating filters: OB25 (Hα, region used for analysis $\lambda\lambda$ 6475 − 6630)[3], Ca41 (Ca II K region used for analysis $\lambda\lambda$ 3910 − 3990), and RV31 (region used for analysis $\lambda\lambda$ 5150 − 5300). OB25 and Ca41 filters gave 155 Å centered on the principal spectral features in Hα and 80 Å in Ca II H&K. RV31 filter was used to determine accurate radial velocity of the stars in M13 and M92. The spectral resolution was about 34,000 as measured by the FWHM of the ThAr emission lines in the comparison lamp. Exposures in each of the three orders are summarized in Table 2.1. A raw CCD image of Hectochelle with the Ob25 filter can be seen in Figure 2.2.

Bias and quartz lamps for the flat correction were obtained each day. In early observations (2005), exposures with the ThAr comparison lamp were obtained during the

[3]The 2005 May observation had less wavelength coverage.

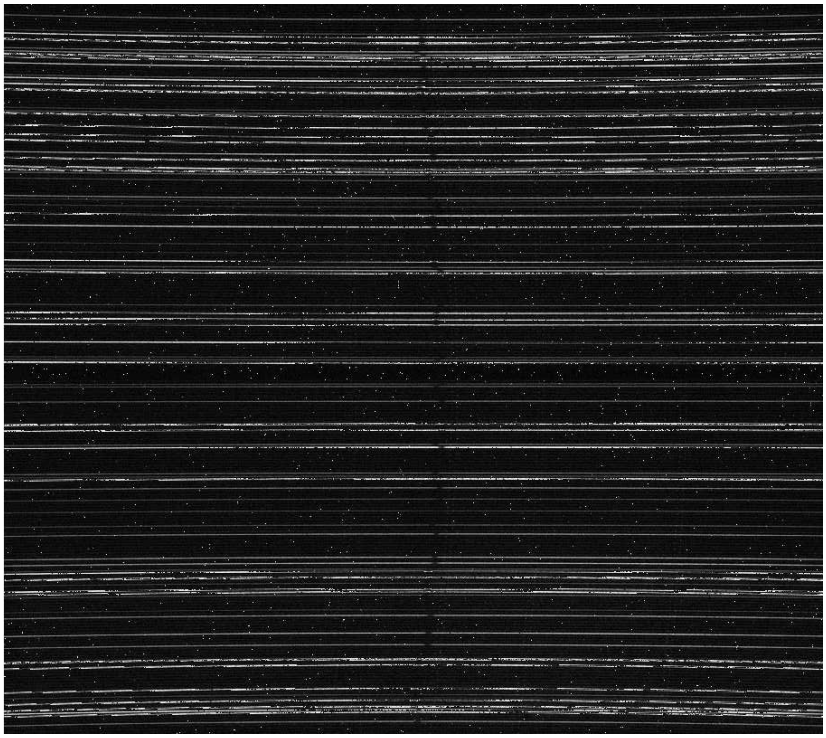

Figure 2.2: *Raw CCD image of Hectochelle with the OB25 filter taken on 2006 March 14 from selected red giants in M13. There are 240 apertures in the CCD, but only the ones with bright stars are visible here.*

afternoon with exposure times of 900 sec. As the observation techniques evolved, exposures with the ThAr lamp were taken with exposure times of 150 sec before and after every observation during the night to determine the wavelength solution. The number of objects observed changed slightly between observations, because fiber positions need to be reconfigured when targets pass the meridian.

In the 2005 May spectra of Hα in M15, the filter's central wavelength was offset by $\sim$ 80 Å placing the Hα line near the long wavelength end of the CCD. Fluxes at wavelengths shorter than Hα were abnormally low, because the grating was so far off the blaze angle. The wavelength regions spanned by the OB25 filter differed between the 2005 and 2006 observations; however both contained the Hα line and photospheric lines.

2.2 Data Reduction

Data reduction was done using standard IRAF spectroscopic packages. The IRAF package *ccdproc* performed the trimming and the overscan correction and made the bad pixel mask using a template created for the CCD camera of Hectochelle. The trimming correction was necessary because a swap of an I/O card in chelle electronics caused an additional pixel at the beginning of each row. The overscan correction was done to target and bias images as well to monitor possible changes in pixel count with time.

The overscanned and averaged bias image was then subtracted from every spectrum. Correcting with the dark images was not necessary because even in the 40 minute dark exposures the intensity was very low [$3 - 4$ analog digital units (ADU) per pixel].

To find and trace the apertures, ten flat images were taken with the continuum lamp of 10 seconds exposure time each. The focal plane of Hectochelle consists of a mosaic of 2 CCDs that are slightly misaligned. The aperture finding algorithm fails near the crack between the two CCDs, so manually editing the apertures and reordering them was necessary. Some apertures were deleted from the edges of the CCD and a total of 240 orders was extracted.

To correct for the pixel-to-pixel variations, the averaged continuum flat exposures for each configuration were fitted with a 21st order spline function (using the IRAF task *apflatten*) and used to divide the corresponding object spectra by the normalized flat. A region 13−pixels wide was carefully selected for the aperture extraction, because apertures are close to each other and scattered light from a bright star can affect the neighboring apertures.

Wavelength standards, using ThAr hollow cathode lamps were taken to define the wavelength scale; each ThAr image obtained in 2005 had 900 seconds of exposure time and was taken at the beginning of the night. For observations taken in 2006, the 150 seconds of exposure time ThAr images taken before and after every scientific exposure were used for determining the wavelength solution. This allowed to eliminate small wavelength shifts coming from the different fiber placements during the night. I identified $15 - 20$ strong ThAr emission lines in the first aperture, then propagated these identifications to every other aperture manually to check the accuracy of the fit. During the calibration the rms of the wavelength fit had to be between $0.01 - 0.002$ Å to reach the theoretical resolution of the spectrograph. If the error of the fit is larger than this, it will be comparable to the expected width of the ThAr features ($0.1 - 0.2$ Å) and increase the error of the wavelength solution.

The continuum flat images were used to correct the throughput for each aperture using a region close to the CCD center containing $5 - 7$ neighboring fibers. An average of the selected continuum flat apertures was taken and divided into all other apertures in the same exposure and was used to correct the vignetting and fiber-to-fiber throughput deviation. An example of a extracted, wavelength calibrated spectrum after the throughtput correction can be seen in Figure 2.3.

The extracted spectra also contain sky background which had to be subtracted. Some of the sky apertures showed weak Hα and other photospheric lines suggesting very faint stars in those positions. Also very bright stars can cause scattered light in the neighboring apertures on the CCD, but this becomes visible only if the aperture has more than $8000 - 10000$ ADUs per pixel. The brightest stars reached 10000 ADUs per pixel in the 40 minute exposures and some apertures contained very low level scattered light.

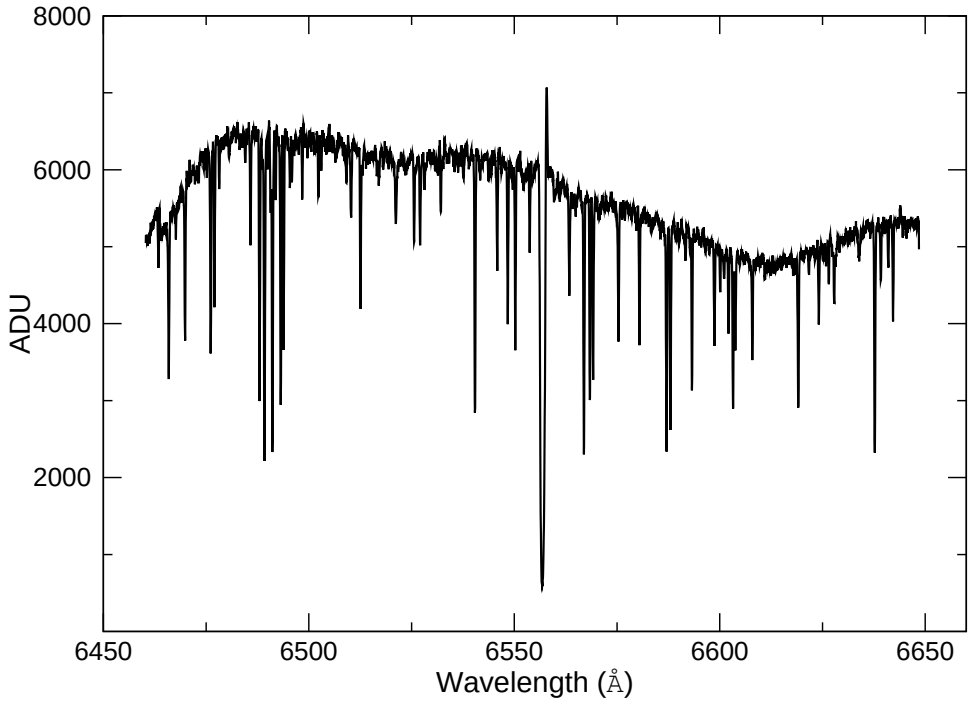

Figure 2.3: *Example of a Hα spectrum taken on 2006 March 14 after all reductions, but before sky subtraction and continuum normalization.*

Every sky aperture was checked carefully and those where faint stars or scattered light were found were discarded. A median filtered sky was used for the subtraction, but sky subtracted skies frequently contained additional counts, which changed aperture by aperture and by wavelength. In Figure 2.4, a sample of sky intensity versus wavelength and aperture is plotted for the Hα filter. Between aperture numbers 100 and 150, especially at longer wavelengths, the apertures have higher intensity. The dark images did not show high intensity features and the intensity pattern in Figure 2.4 is currently not understood. To subtract the sky, the images were divided into 3 different aperture sections, and the sky subtraction was done with the following method. In the first and third segments (corresponding to aperture numbers $0 - 100$ and $150 - 240$), the intensity appears constant as a function of aperture number and wavelength so the median filtered spectrum could be used for subtraction. The middle region spanned aperture numbers 101 to 149, in this region the sky was subtracted from every target aperture using the average of 3 closest sky apertures on the CCD itself.

Continuum normalization was done with the IRAF task *continuum*. A one dimensional, low order Chebyshev function was fit to the continuum of each spectra individually to produce a normalized spectrum. The normalization of the spectra obtained with the OB25 and RV31 filter is well determined, because the continuum is visible and deep lines like the Hα line were omitted from the fit. Continuum normalization is challenging in the Ca41 filter, because hundreds of absorbing lines depress the continuum substan-

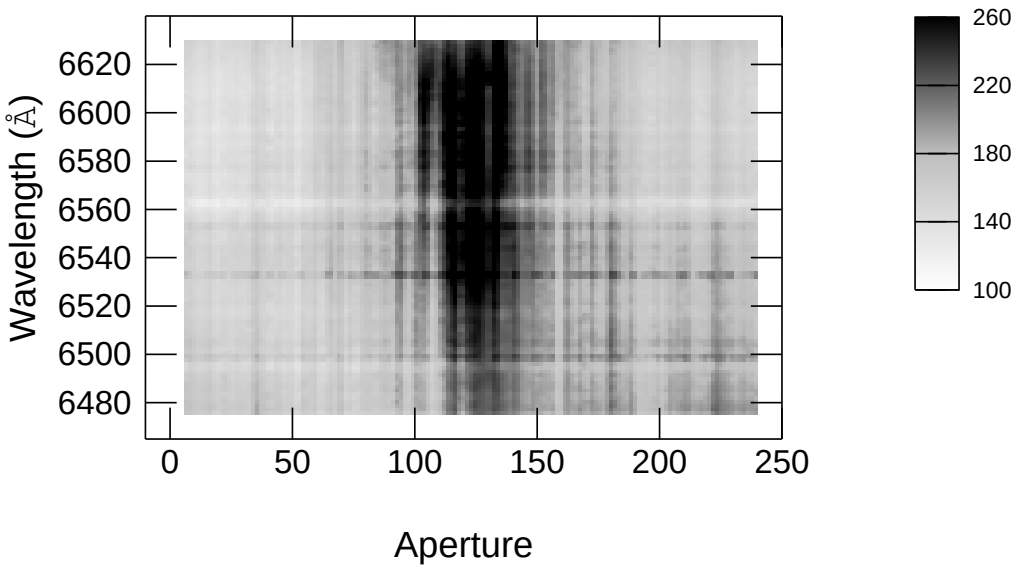

Figure 2.4: *Variations in the intensity of the sky apertures in the Hα filter. Dark area indicates the highest count level. See scale at right. An anomalous intensity pattern occurs, which is currently not understood. Special extraction patterns were used for the sky fibers (see text).*

tially. Here, also a low order Chebyschev function was used to fit and normalize the local continuum away from the strong Ca II lines.

Chapter 3

Line Statistics

In the first section of this chapter I describe how radial velocity measurements were done, which is important to determine which stars are cluster members. In the second section I explain how emission features were identified in the Hα and Ca II K spectrum. In the third section I briefly review the position of stars with Hα emission on the CMD. The fourth section describes the Hα line bisector and its determination, which shows motions in the atmosphere, while the last section explains the Ca II K emission characteristics.

3.1 Radial Velocity Measurements

Radial velocity measurements use the Doppler-effect. The Doppler-effect results in either a redshift, or a blueshift of spectral features of a receeding or an approching light source. The radial velocity of a star can be measured accurately by taking a high-resolution spectrum and comparing the measured wavelengths of known spectral lines to wavelengths from laboratory (rest-frame) measurements. By convention, a positive radial velocity indicates that the object is receding, a negative radial velocity means that the object is approaching. If spectral features are dominating the spectrum of a star, the cross-correlation is the widely accepted method to measure the radial velocity.

The cross-correlation is a measure of similarity of two spectra as a function of a time-lag applied to one of them. The definition of cross-correlation is:

$$f \star g \;=\; \int_{-\infty}^{\infty} f(\tau) g(t+\tau) d\tau \tag{3.1}$$

Consider two functions f and g that differ only by a shift along the x-axis. The equation slides the g function along the x-axis, calculating the integral of their product for each possible amount of sliding. When the two functions match, the value of $f \star g$ is maximized.

The definition of cross-correlation can be given by using Fourier transforms:

$$\mathcal{F}\ (f \star g)\ =\ F^*(\nu)G(\nu) \tag{3.2}$$

where $\mathcal{F}$ denotes the Fourier transform, $F^*(\nu)$ denotes the complex conjugate of $F(\nu) = \mathcal{F}\,[f(\tau)]$. In this case $f \star g$ can be obtained by the inverse Fourier transform $\mathcal{F}^{-1}\,[F(\nu)G(\nu)]$. For discrete and two real valued functions, f and g, the cross-correlation is defined as:

$$(f \star g)[n]\ =\ \sum_{m=-\infty}^{\infty} f[m]\ g[n+m] \tag{3.3}$$

In the case of radial velocity measurement both f and g are spectra, where f is the observed, g is the template spectrum. τ represents the small $\Delta\lambda$, which we use to shift the template. The position of the peak of the cross-correlation function gives the value of radial velocity. It is important to select templates similar to the observed spectra, otherwise the cross-correlation function will not have a well-determined peak.

3.1.1 M15

To measure accurate radial velocities I chose the cross-correlation method using the IRAF task *xcsao*. Using the ATLAS (Kurucz, 1993) code, I synthesized the spectrum of a red giant star, K341, in M15. This is a bright star with a high quality spectrum, thus the comparison between the observed and modeled spectrum is optimum. The physical parameters of the template spectrum were the following: $T_{\rm eff}$ = 4275 K, log g = 0.45, $v_{\rm turb}$ = 0 km s^{-1}, $v_{\rm macro}$ = 0 km s^{-1}, [Fe/H]=−2.45, [Na/Fe]=0.01, [Si/Fe]=0.4, [Ca/Fe]=0.56, [Ti/Fe]=0.57, [Ba/Fe]=0.2 (Sneden et al., 2000). This spectrum is computed in LTE and a chromosphere was not included in the atmospheric model, thus it only contains absorption features. The comparison between the template in our cross-correlation and the observed Hectochelle spectrum can be seen in Figure 3.1. Radial velocity measurements were only possible using the OB25 filter, because observations with the RV31 filter were not obtained for stars in M15. All determined radial velocities are corrected to the solar system barycenter.

The region selected for the cross-correlation spanned 6480 Å to 6545 Å purposely omitting the Hα line. The telluric and photospheric lines were identified using the synthesized spectrum of K341. In this region there are many telluric lines of water vapor. These lines appear in the cross-correlation function profile as an additional peak, well separated from the cluster velocity, and so the measured stellar radial velocity is not affected. To verify our radial velocities, I cross-correlated a narrow region $\lambda\lambda\ 6480-6500$ where no strong telluric lines are found. Cross-correlating this narrow region results in the same radial velocity as from the broader window, but with a larger (1−2 km s^{-1})

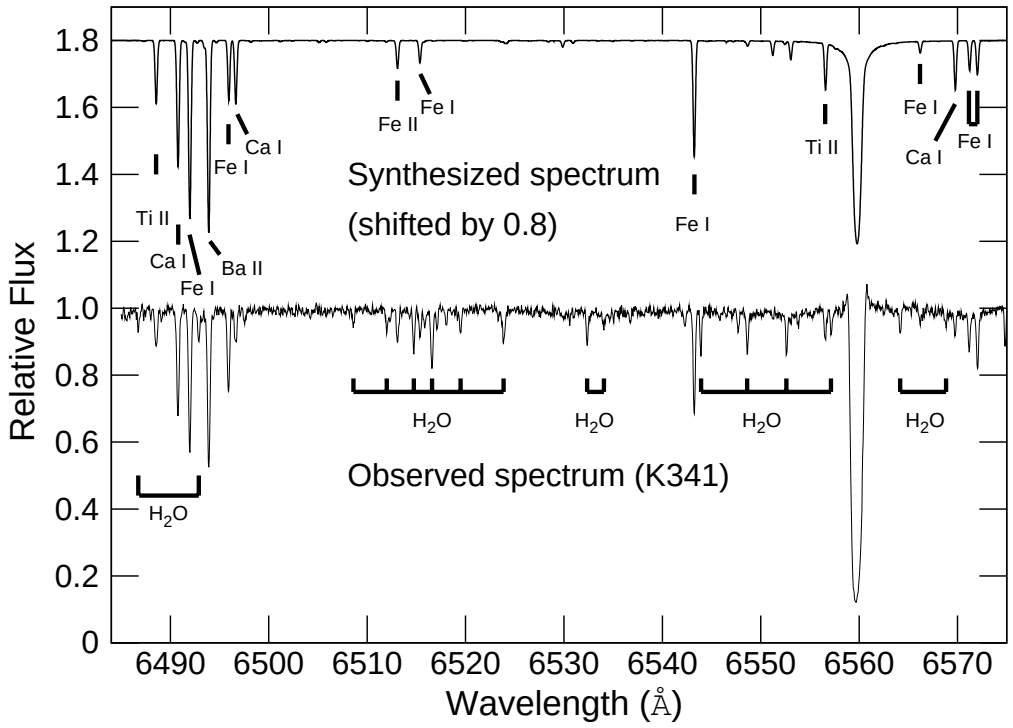

Figure 3.1: *Kurucz synthesized spectrum shifted by 0.8 in relative flux and corrected for the star's radial velocity shown above the observed spectrum of K341 in M15. Atmospheric water vapor and other elements are marked.*

error.

The Hα spectra of our targets were also cross-correlated against several hundred spectra calculated by Coelho et al. (2005) covering temperatures between 3500 and 7000 K and metallicities between [Fe/H]=−2.5 and +0.5. These velocities from the Coelho spectra agreed within 1 to 2 km s^{-1} with our earlier determination using only the K341 template, because the same photospheric Fe and Ti absorption lines can be found in all the spectra.

There is good agreement between our radial velocities from the 2005 data and those of Gebhardt et al. (1997) and Peterson et al. (1989) (see Figure 3.2, top panels). Gebhardt et al. (1997) used an Imaging Fabry-Perot Spectrophotometer with the Sub-arcsecond Imaging Spectrograph on the Canada-France-Hawaii Telescope and observed 1534 stars in M15 with velocity errors between 0.5 and 10 km s^{-1}. Peterson et al. (1989) used echelle spectrographs on the MMT, the 1.5 m Tillinghast reflector of the Whipple Observatory on Mount Hopkins, and the 4−m telescope of Kitt Peak National Observatory. Peterson et al. (1989) quote an average error of 1 km s^{-1}, but the stars in common with our sample have larger errors (1−2 km s^{-1}).

However the Hectochelle velocities from 2006 display a systematic offset from the 2005 measurements of the same stars (see Figure 3.2, lower panels). This offset amounts to +1.9 $\pm$ 0.5 km s^{-1} and +0.9 $\pm$ 0.5 km s^{-1} for 2006 May and Oct 2006 respectively,

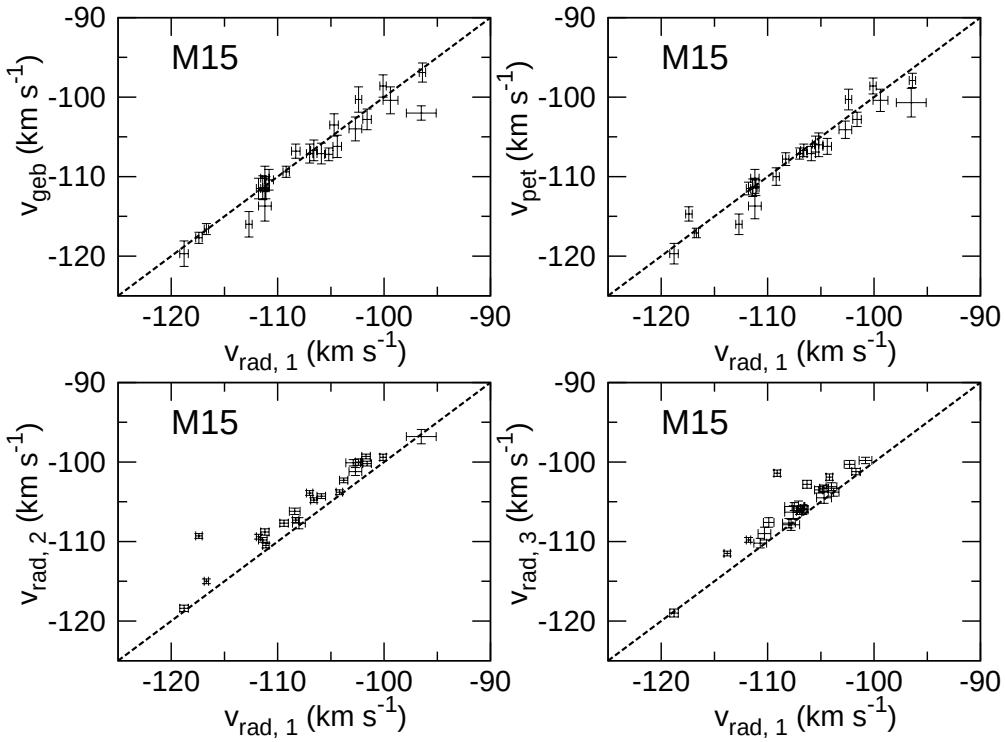

Figure 3.2: *Top left: Radial velocities measured on 2005 May 22 ($v_{\rm rad,1}$) for the same stars observed by Gebhardt et al. (1997) (v_{geb}) in M15. Top right: Radial velocities measured on 2005 May 22 ($v_{\rm rad,1}$) for the same stars observed by Peterson et al. (1989) (v_{pet}). There is good agreement between observations taken on 2005 May 22 and observations for the same stars from Gebhardt et al. (1997) and Peterson et al. (1989). Lower left: Radial velocity measured with Hectochelle for the same stars observed on 2005 May 22 ($v_{\rm rad,1}$) compared to 2006 May 11 ($v_{\rm rad,2}$). The velocity offset between 2006 May 11 and 2005 May 22 is $+1.9 \pm 0.5$ km s^{-1} . Lower right: Radial velocities for the same stars measured with Hectochelle on 2005 May 22 ($v_{\rm rad,1}$) compared to 2006 October 4 ($v_{\rm rad,3}$). The velocity offset between 2006 October 4 and 2005 May 22 is $+0.9 \pm 0.5$ km s^{-1}. The dashed line marks a 1:1 relation. The offsets are applied to our radial velocities for the 2006 May and 2006 October spectra.*

and the data in Appendix Table 7.7 were corrected for this systematic offset. The radial velocities of the sky emission lines show the same effect. In 2005, all of the sky emission lines were at 0 km s^{-1} and in 2006 May were at -2 km s^{-1}, yet the wavelength calibration of the 2006 data appears to be as accurate as 2005. The source of this offset comes from using the ThAr comparison lamp obtained during the afternoon and not before and after the scientific exposures. The telescope is at zenith for the afternoon calibration lamps, however the observed clusters are at a very different position on the sky. When the telescope moves, the position of fibers changes in their chamber, which introduces small linear $1-2$km s^{-1} shifts in the spectra. The amount of the offset is small, and does not affect determination of cluster membership. The average cluster radial velocity was calculated using velocity-corrected data from all four observations. Our value is -105.0 ± 0.5 km s^{-1}, which is slightly lower than the cluster radial velocity (-107.0 ± 0.2 km s^{-1}) quoted in the Harris (1996) catalog.

Previous studies suggested that several of the sample stars are binaries. Significant

Table 3.1. Radial Velocities of Apparent Non-members in M15

ID No.	*RA*(2000) [a]	Dec(2000) [a]	V [b]	B-V [b]	$v_{\rm rad}$ (km s^{-1}) [c]	P [b]	Obs. [d]
B14	21 29 56.70	+12 22 20.1	12.71	0.49	-22.7 ± 0.4	99	1,2,4
B22	21 30 36.04	+12 05 17.6	13.92	0.91	-12.1 ± 0.4	96	1,2,3,4
B25	21 30 39.65	+12 05 23.5	12.39	1.14	-5.4 ± 0.4	99	1,2
C19	21 29 52.30	+11 59 40.2	14.89	0.87	-50.9 ± 0.6	93	1,2,3,4
K7	21 29 27.03	+12 07 26.9	12.83	0.88	-177.4 ± 0.5	98	1,2,4
K28	21 29 35.27	+12 14 40.0	13.67	1.04	-68.5 ± 0.4	90	1,3,4
K44	21 29 58.32	+12 09 56.5	15.36	1.04	-41.4 ± 0.5	67	3
K73	21 29 44.19	+12 09 17.1	13.62	0.74	-38.4 ± 0.6	94	3
K609	21 29 58.84	+12 17 29.4	14.88	0.79	$+4.7 \pm 0.6$	96	1,2,3,4
K996	21 30 06.80	+12 11 10.0	14.29	0.13	$+15.8 \pm 0.5$	99	1
K1095	21 30 20.32	+12 00 42.4	12.67	0.64	-1.7 ± 0.5	99	1,2,4
K1096	21 30 20.45	+12 17 55.9	14.03	0.60	-13.5 ± 0.5	98	1,2

[a] 2MASS coordinates (Skrutskie et al., 2006).

[b] The visual photometry and membership probability from proper motions are taken from Cudworth (1976).

[c] Average radial velocities were calculated from all cross-correlations.

[d] Observations: 1: 2005 May 22, 2: 2006 May 11, 3: 2006 October 4, 4: 2006 October 7.

velocity variations, ≈ 6.5 km s^{-1}, for K47 were found by Soderberg et al. (1999), but our measurements showed only 0.9 km s^{-1} variation between 2005 May and 2006 May. This change lies within the measurement errors (≈ 1 km s^{-1}). K757 and K825 were suggested as binaries by Sneden et al. (1997) from the asymmetric line profiles; weak satellite wings were visible for nearly all spectral lines. I have only one observation of K825, but the radial velocity of K757 changed by 6.2 km s^{-1}, which could indicate that this star is a binary. The detailed study of the Hα line of this star (Mészáros et al., 2009b) revealed that fast motions are present in the chromosphere and most likely this star is pulsating (see Section 5.3 for detailed analysis). Drukier et al. (1998) found 17 cluster members of M15 showing possible radial velocity variability. Four of these stars were observed with Hectochelle, but only one of them, K92, was observed more than once. This star showed 1.4 km s^{-1} variability between 2005 May 22 and 2006 October 7, but the error of these observations was close to 1 km s^{-1}. Five additional stars showed velocity changes larger than 2 km s^{-1}, which could indicate these stars are binaries: B5 (6.8 km s^{-1}), B30 (2.9 km s^{-1}), K1084 (2.6 km s^{-1}), K1097 (2.1 km s^{-1}), and K1136 (3.0 km s^{-1}).

Some of the M15 targets selected from the proper motion study of M15 (Cudworth, 1976) turned out to have substantially different radial velocities from the cluster average (see Table 3.1) and are not likely to be members of the cluster. These stars are not included in the spectroscopic analysis.

3.1.2 M13 and M92

For stars in M13 and M92, also the cross-correlation method was chosen using the IRAF task *xcsao*. Two filter regions, OB25 and RV31, were used for radial velocity measurements. The spectral region on the RV31 filter between 5150 Å and 5300 Å contains several hundred narrow photospheric absorption lines of predominantly neutral atoms and very few terrestrial lines, thus the cross-correlation function is narrower than from the Hα region, which only contains $\sim$10 lines (Figure 3.3). In the OB25 filter, the region selected for the cross-correlation spanned 6480 Å to 6545 Å purposely omitting the Hα line. This results in 100$-$200 m s^{-1} errors with the RV31 filter as compared to 200$-$400 m s^{-1} using the wavelength region earlier described in the Hα filter.

Spectra of our targets from both filters were cross-correlated against 2280 spectra calculated by Coelho et al. (2005) covering temperatures between 3500 and 7000 K, metallicities between [Fe/H]=$-$2.5 and +0.5, and log g between 0 and 5. Radial velocities were corrected to the solar system barycenter. To calculate the radial velocity of a star, the radial velocities from ten templates with the highest amplitude of the cross-correlation function for each filter were collected and averaged together. A sample of the template spectra compared to an observation can be seen in Figure 3.3. The physical parameters of the templates that were used for the radial velocity measurements usually agreed with each other within 200 K in temperature, 1 in log g, and $-$0.5 in [Fe/H] with our calculated physical parameters (Appendix Tables 7.5 and 7.6). For almost every star the radial velocity differences among the 10 highest correlation templates in each filter were less than 0.5 $\pm$ 0.2 km s^{-1}, which is close to the error of the individual measurements.

I compare our results with those found in the literature. In M13, Soderberg et al. (1999) used the Hydra spectrograph on the 4-m Mayall telescope to obtain spectra of 150 stars. Their template for the cross-correlation was an averaged spectrum of all giants for each Hydra observation. Therefore the individual radial velocities were determined as compared to the average cluster velocity. The radial velocity of the averaged spectrum was calculated by cross-correlating it to the solar spectrum. Comparison of the results can be seen in Figure 3.4. Errors spanned 0.5 km s^{-1} to 3$-$5 km s^{-1} in their sample, and there is a systematic 1.1 $\pm$ 0.5 km s^{-1} offset (Figure 3.4, left upper panel) between our radial velocities and those of Soderberg et al. (1999). Hectochelle velocities determined using the Hα region from 2006 March 14 agreed with the observations two days later with the RV31 filter (see Figure 3.4, left lower panel) for the same stars. Radial velocities calculated from the data taken with the RV31 filter in 2006 May also agreed with data taken with the OB25 filter on 2006 March 14 (Figure 3.4, right upper and lower panel). I find the average radial velocity of M13 to be $-$243.5 $\pm$ 0.2 km s^{-1}, which is slightly lower than the cluster radial velocity ($-$245.6 $\pm$ 0.3 km s^{-1}) quoted in the Harris (1996) catalog.

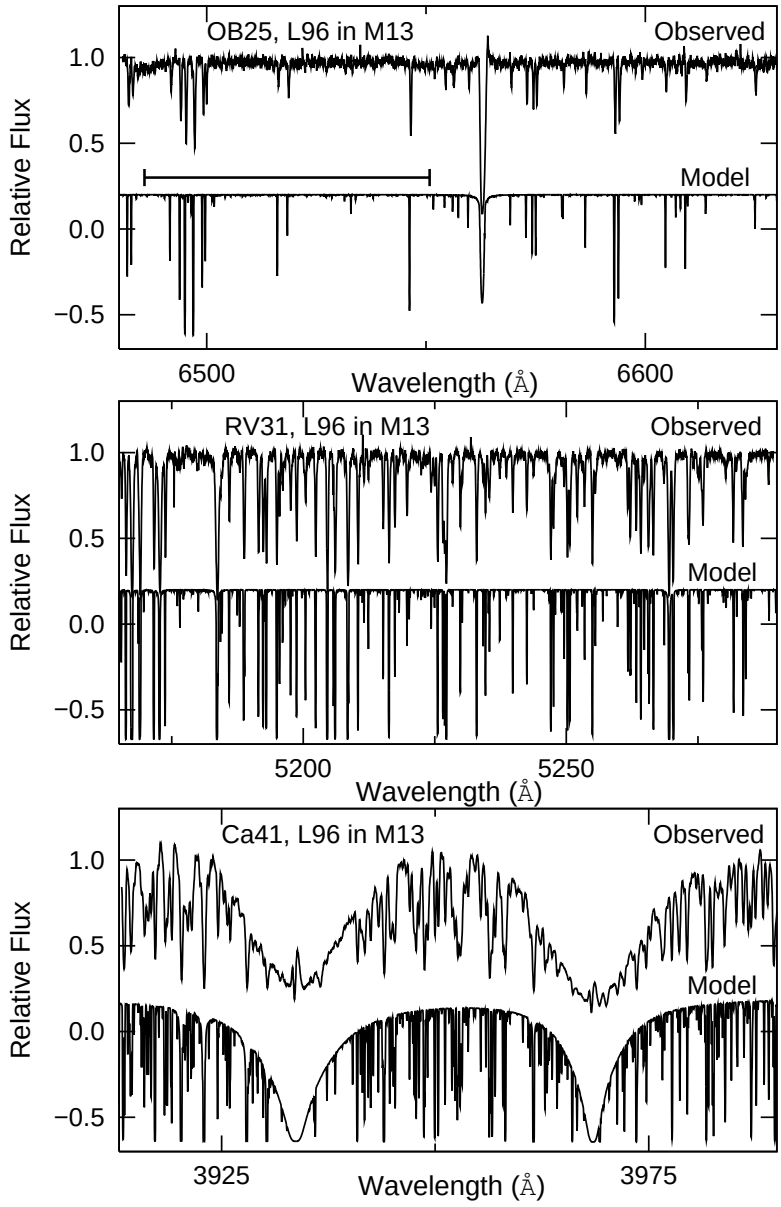

Figure 3.3: *Continuum normalized spectra of a sample star (L96) in M13 showing Hα, RV31, and Ca II H&K spectra after all reductions. Upper spectrum is the observed one, lower spectrum is the model synthesis of a star (Coelho et al. 2005, using Kurucz models) with the highest amplitude of the cross-correlation function from the Hα region. The cross-correlation region used in the OB25 filter is marked in the spectrum and chosen to avoid Hα .*

Five stars observed with Hectochelle in M13 were reported as possible binaries by Shetrone (1994), when the radial velocities measured with the 3-m Shane telescope (Lick Observatory) were compared with velocities determined by Lupton et al. (1987). In all of these stars, differences between the two observations were larger than 4 km s^{-1} which exceeds the measurement errors of ~ 1 km s^{-1} and may reflect intrinsic stellar variability or binary reflex motions. Our radial velocities differ by $4-5$ km s^{-1} compared with Lupton et al. (1987), but agree within $1-2$ km s^{-1} with Shetrone (1994), which also

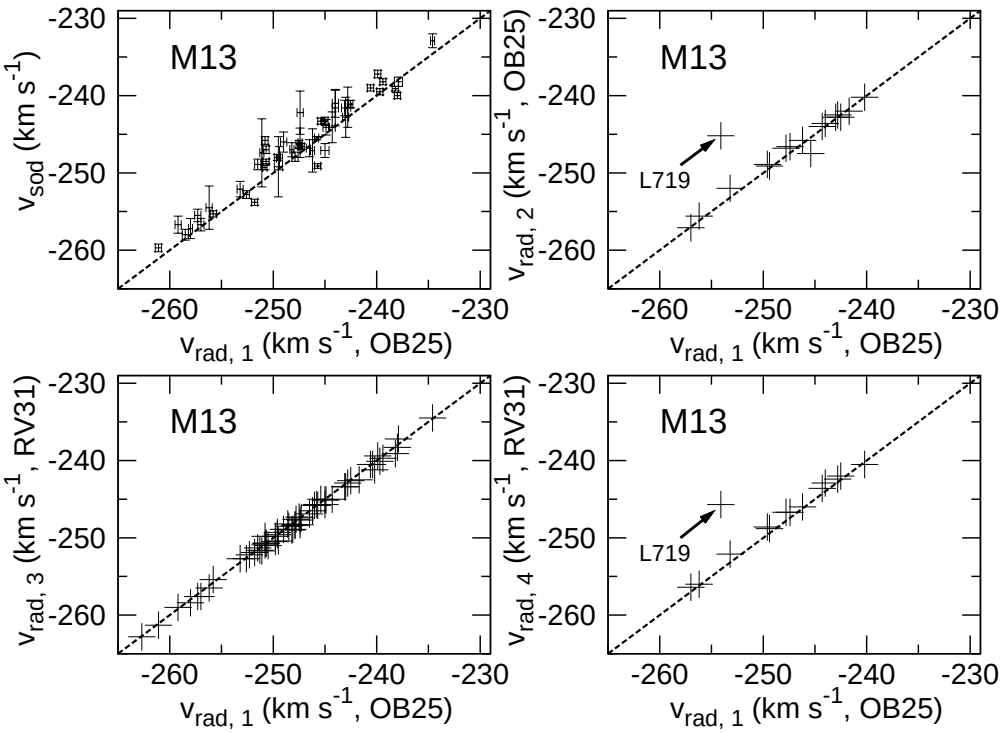

Figure 3.4: *Top left: Radial velocities measured with the Hα filter (OB25) on 2006 March 14 ($v_{\rm rad,1}$) compared to the same stars observed by Soderberg et al. (1999) (v_{sod}) in M13. There is a slight offset (1.1 $\pm$ 0.5 km s^{-1}) between all observations taken in 2006 and observations for the same stars from Soderberg et al. (1999). Top right: Radial velocities measured on 2006 March 14 ($v_{\rm rad,1}$) for the same stars observed on 2006 May 10 with the Hα filter ($v_{\rm rad,2}$). Lower left: Radial velocity measured with Hectochelle for the same stars observed on 2006 March 14 ($v_{\rm rad,1}$) compared to the observations with the RV31 filter on 2006 March 16 ($v_{\rm rad,3}$). Lower right: Radial velocities for the same stars measured with Hectochelle on 2006 March 14 ($v_{\rm rad,1}$) compared to the observations with the RV31 filter on 2006 May 10 ($v_{\rm rad,4}$). The dashed line marks a 1:1 relation in all panels. The error of our measurements was generally smaller than the symbols used in the figure. The anomalous star in M13, L719, lies between the AGB and RGB, and the large velocity change may indicate binarity.*

suggests that long-term changes are present. Among these five stars, I observed one, L72, which showed 2.1 km s^{-1} velocity change between 2006 March and 2006 May. Lupton et al. (1987) identified this star in M13 as a possible binary from variations in radial velocity over several years of observations. L72 is also known as a pulsating variable star with a possible period of 41.25 days (Russeva & Russev, 1980), so the velocity change found here may also relate to pulsation. L719, which marks the faint luminosity limit of stars showing Hα emission, also had radial velocity changes between 2006 March 14 to 2006 May 10 from -254.1 ± 0.3 km s^{-1} to -245.2 ± 0.2 km s^{-1} . If this object were a single line binary, the velocity change allows only lower limits to the period (P>90 days) and semi-major axis (a >10R$_\star$). The putative companion to the red giant could be either a white dwarf or a late main sequence star, and probably the former since the color is bluer than a red giant. No other stars showed significant, larger than 2 km s^{-1}, variations in our sample in M13.

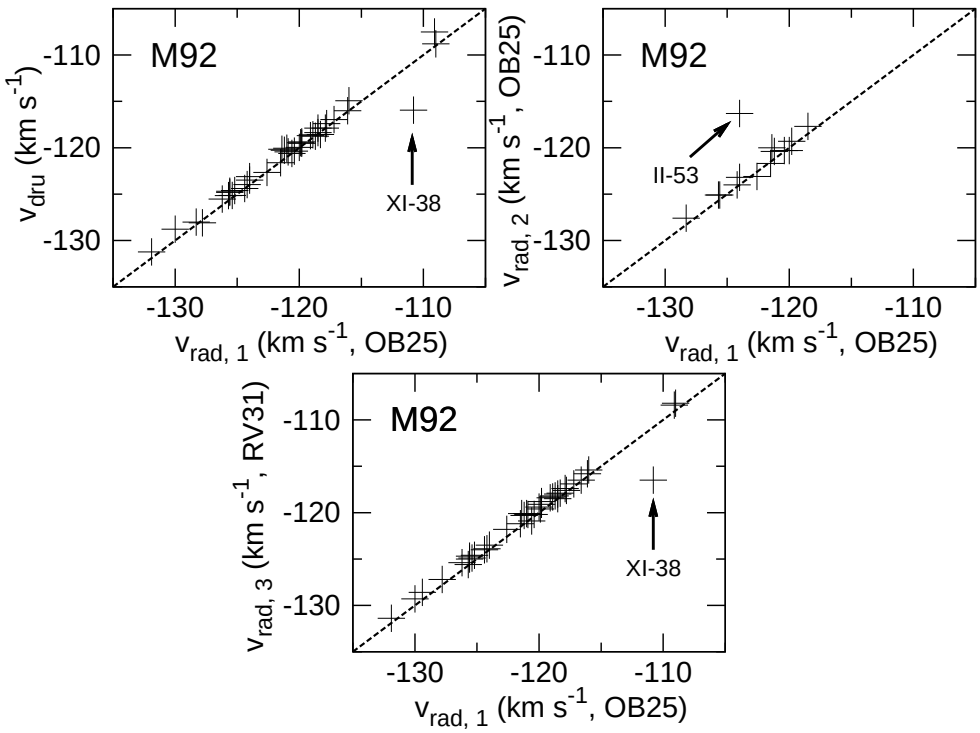

Figure 3.5: *Top left: Radial velocities measured with the Hα filter on 2006 May 7 ($v_{\rm rad,1}$) compared to the same stars observed by Drukier et al. (2007) (v_{dru}) in M92. Top right: Radial velocities measured on 2006 May 7 ($v_{\rm rad,1}$) for the same stars observed on 2006 May 9 with the Hα filter ($v_{\rm rad,2}$). Center: Radial velocity measured with Hectochelle for the same stars observed on 2006 May 7 ($v_{\rm rad,1}$) compared to the observations with the RV31 filter on the same day ($v_{\rm rad,3}$). There is no offset larger than the error of measurements between any observations. The dashed line marks a 1:1 relation in all panels. There is good agreement between all observations taken in May and observations for the same stars from Drukier et al. (2007). The error of our measurements was generally smaller than the symbol I used in the figure. For discussion of the two outlier stars see Section 3.1.2.*

A large sample of stars in M92 was observed by Drukier et al. (2007) using the HYDRA multi-fiber spectrograph on the 3.5-m WIYN telescope. Their errors spanned 0.3−1.2 km s^{-1} . The comparison of results can be seen in Figure 3.5. Radial velocities for the same stars agreed within the errors (Figure 3.5, left upper panel). The Hectochelle spectra give the cluster average radial velocity as -118.0 ± 0.2 km s^{-1}, which is lower than the value (-120.3 ± 0.1 km s^{-1}) quoted in the Harris (1996) catalog. In M92, two stars show radial velocity variations, which usually indicates binarity or pulsation. II-53 had a significant velocity variation of 7.7 km s^{-1} between 2006 May 7 and 2006 May 9. Another star, XI-38, showed a 4.9 km s^{-1} difference between the radial velocity measured by Drukier et al. (2007) and the velocity measured by us on 2006 May 7.

3.2 Determining the Hα Emission

Two methods have been used for the identification of Hα emission. The first selects stars with flux in the Hα wings lying above the local continuum. Strong emission can be easily found, however faint emission comparable to the noise of the continuum can be missed. A second method was introduced by Cacciari et al. (2004) and is illustrated in Figure 3.6. They select a star without emission and the Hα absorption line from this star is subtracted from the other spectra. With this method weak emission can be identified, but it strongly depends on the template selected. The Hα absorption profile depends on temperature, as well as broadening from turbulent velocity and rotation, both of which could introduce features in the subtracted profile. An individual Kurucz model can be made for every star as a template, and the temperature problem can be avoided, but the uncertainty of other physical parameters can introduce similar effects in the subtracted spectrum.

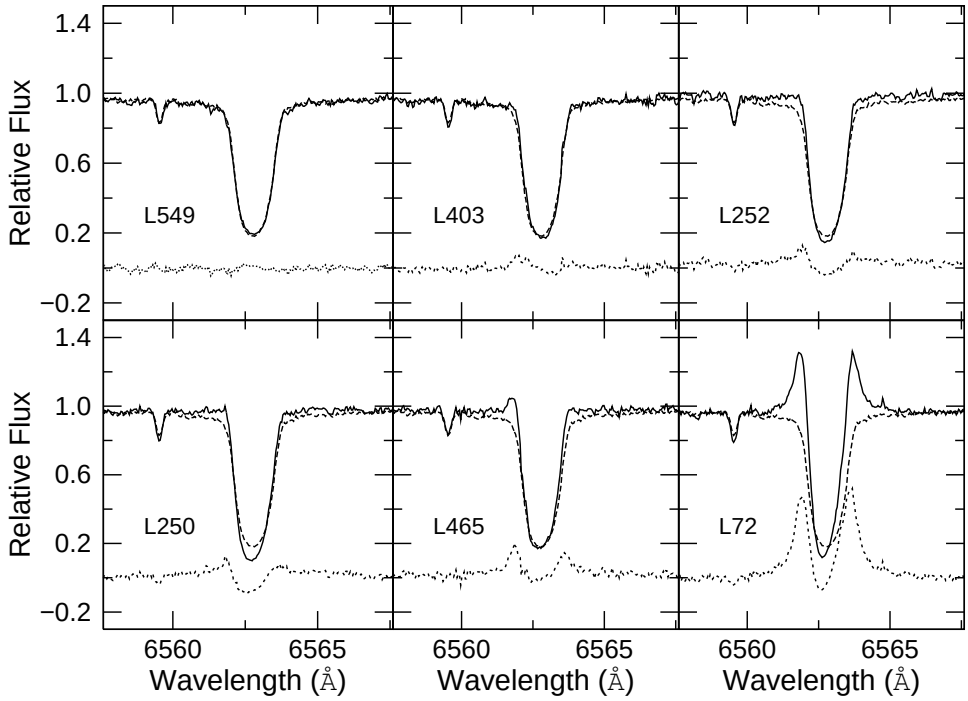

Figure 3.6: *Examples of the effect of subtracting an averaged spectrum (dashed line) from the observed spectra (solid lines) for stars in M13. The difference spectrum is shown by a dotted line below. L549 is a star without any emission; the error of the subtracted spectrum (dotted line) is smaller than 0.02 of the continuum level. In the case of L403, weak emission on the short wavelength is visible, however it is comparable to the noise of the observed spectrum and extends to the core of the line, so it was not identified as emission. L252 is an example of how the continuum normalization can shift the region near Hα making it hard to identify the emission. The blue emission in the spectrum of L250 might be missed by eye, but the subtraction method clearly shows the presence of emission. L465 and L72 are examples of emission that is clearly visible in the spectrum above the continuum level.*

In a continuum-normalized spectrum, the Hα emission appears above the continuum level for the majority of stars (L465 and L72 in Figure 3.6). However in fainter stars only the shape of the Hα line profile is changing and the emission does not appear above the continuum, rather just a small additional flux emerges in the absorption wings (L250 and L252 in Figure 3.6). The identification of this kind of emission can be challenging (L403 in Figure 3.6). In this paper, I used both methods. However, I selected 8 stars with no emission and of different colors and luminosities to make the template. The stars identified with Hα emission are the same with both methods.

No matter which method is used, the detection of faint emission depends on the reduction technique. Continuum normalization and sky subtraction can change the emission flux and move it above or below the continuum level (L252 in Figure 3.6). Continuum normalization was done using a low-order Chebyshev function in the IRAF task *continuum* in order to fit the continuum and filter throughput. The continuum placement strongly depends on the order of the function and the rejection limits below and above the fit. Sky subtraction is especially challenging with Hectochelle because additional counts appear between aperture numbers 100 and 150, possibly due to scattered light. This additional flux depends not only on the aperture but also wavelength, and although a reduction system was developed (Mészáros et al., 2008), all sky background cannot be subtracted in the middle section of the CCD. For these reasons the emission of very faint stars can be hard to identify and this can introduce uncertainties in the statistics of the presence of emission.

3.3 Emission on the CMD

3.3.1 M15

Emission in Hα signals an extended and high-temperature chromosphere; in addition the asymmetry of the emission indicates chromospheric mass motions (Dupree et al., 1984; Mauas et al., 2006). I observed a total of 110 different red giant stars in M15 and found 29 with Hα emission. About half of them were observed more than once. Emission above the continuum in the Hα profile can be seen in Figures 3.7 and 3.8. The color-magnitude diagram (CMD) for each night of observation appears in Figure 3.9. On 2005 May 22, emission is found in stars of V=14.48 and brighter, corresponding to $M_V = -0.89$, using the apparent distance modulus $(m-M)_V = 15.37$ from Harris (1996). Stars in M15 that show emission occurred at different magnitude limits on different dates of observation: $M_V = -1.17$ on 2006 May 11, $M_V = -0.99$ on 2006 October 4 and $M_V = -1.68$ on 2006 October 7. The faintest star on 2005 May 22 showing emission is K582. This star and several others (K158, K260, K482, K875, K979) displaying emission may be located on the AGB as judged by the CMD (Figure 3.9) where they are distinct from the red giant

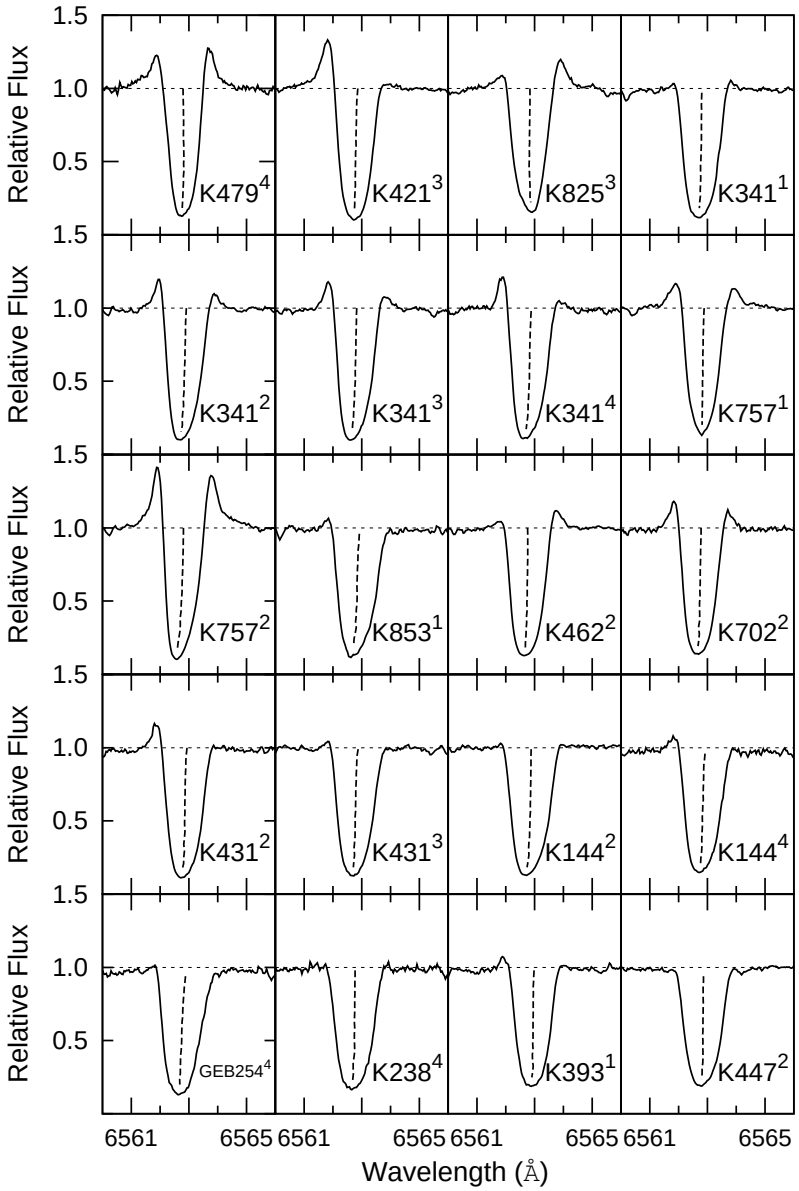

Figure 3.7: *Normalized spectra of red giants in M15 which showed emission in Hα . The dashed line marks the bisector. The spectra are arranged in order of decreasing V magnitude; the brightest is at the top left and the stars become fainter from left to right. The wavelength scale is corrected for heliocentric velocity. K337 is an example of an Hα profile without emission. Stars K260, K341, K757, and K969 showed large variations in Hα emission during the observation period.*

branch, but the separation is not clear from the color-magnitude diagram alone.

Studies of metal deficient field giants found emission in objects brighter than $M_V = -1.7$ (Smith & Dupree, 1988), whereas in the metal rich cluster NGC 2808 the detection threshold for emission was set at $M_V = -1.0$ (Cacciari et al., 2004). It is well documented that the presence of Hα varies with time, and this appears to be the most likely explanation of the differences in the detection level of the Hα emission.

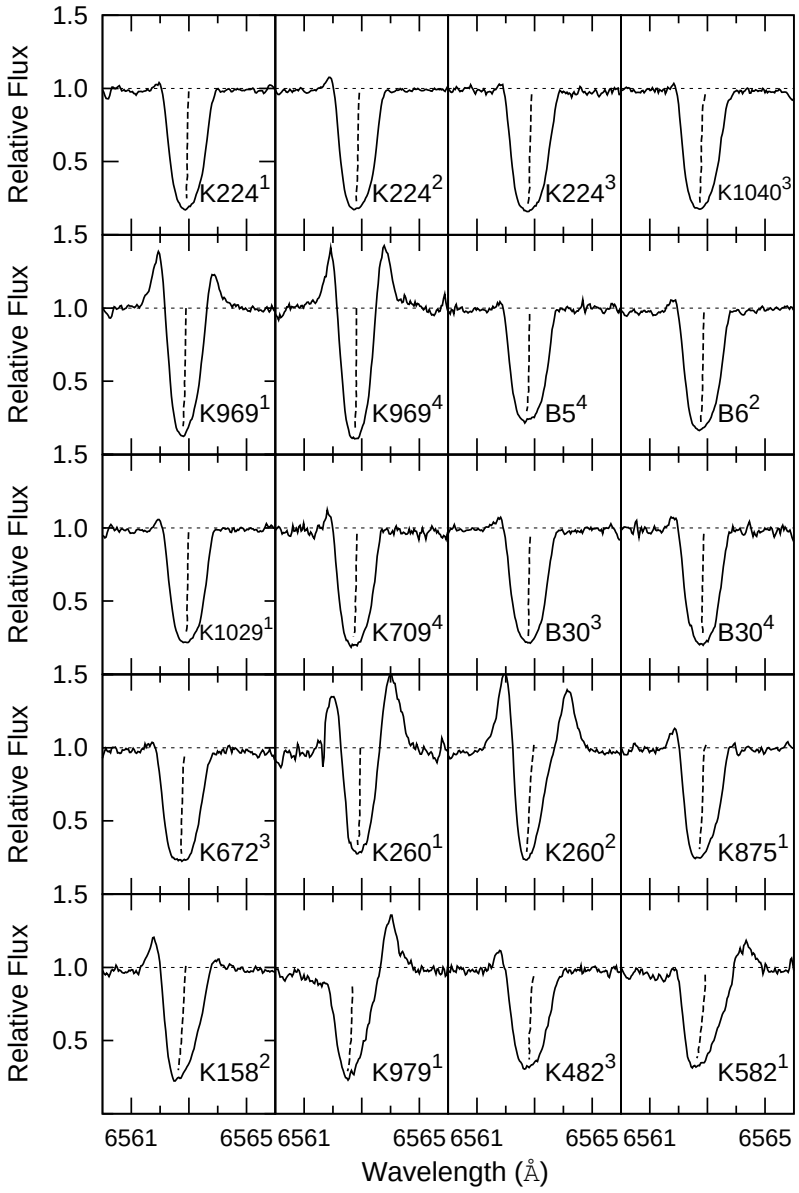

Figure 3.8: *Normalized spectra of red giants in M15 which showed emission in Hα . For explanation please see Figure 3.7. Stars K260, K341, K431, and K757 showed large variations in Hα emission.*

For comparison on a luminosity scale, unreddened colors for M15 stars were calculated taking $E(B-V) = 0.10$, $E(V-K) = 2.75E(B-V)$, and apparent distance modulus $(m-M)_V = 15.37$ (Cardelli et al., 1989; Harris, 1996). The effective temperatures, bolometric corrections, and luminosities were obtained from the $V-K$ visual colors (Table 7.4) using the empirical calibrations by Alonso et al. (1999, 2001) and the cluster average metallicity [Fe/H]=−2.26 (Harris, 1996).

Stars brighter than $\log(L/L_\odot) = 2.36$ can exhibit emission, and all together $\sim 46\%$ of these show Hα emission. The asymmetry of the Hα emission wings was noted for

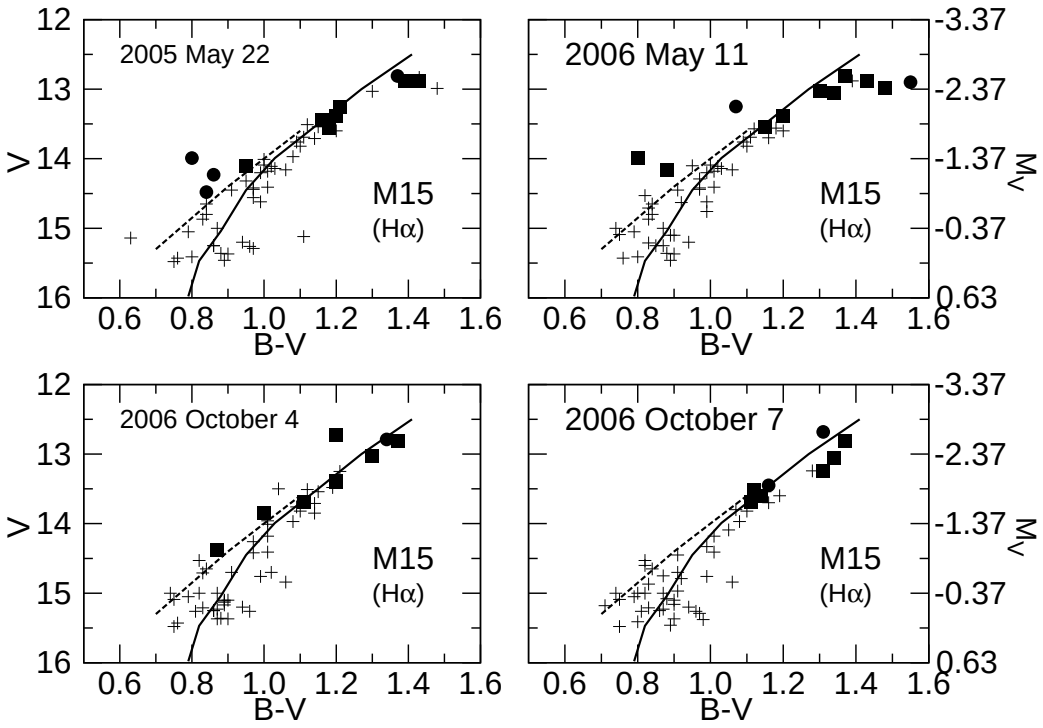

Figure 3.9: *Color-magnitude diagrams for all M15 stars observed in 2005 and 2006. Stars with Hα emission and with B<R (indicating outflow) are marked with circles; stars with B>R emission wings (suggests inflow) are denoted by squares. The solid line shows the fiducial curve of the RGB; dashed lines show the fiducial curve of the AGB for M15 from observations of Durrell & Harris (1993).*

emission above the continuum level where B represents the strength of the short wavelength (blue) emission and R denotes the strength of the long wavelength (red) emission. Figure 3.9 shows the CMD for our targets where the asymmetry of the Hα line is indicated. The frequency of Hα emission increases with the stellar luminosity, however the line asymmetry is not correlated with color and luminosity. Stars with B<R and B>R seem equally distributed in luminosity. Among stars with emission, the majority ($\sim 75\%$) exhibit emission wings with B>R, a signature generally considered to indicate inflow of material.

Spectra of 29 stars with Hα emission were obtained in both 2005 and 2006. All but two of these stars showed significant changes in the line emission which either appeared, or vanished, or changed asymmetry (see Table 3.2, and Figures 3.7 and 3.8).

3.3.2 M13 and M92

I observed a total of 123 different red giant stars in M13 and found 19 with Hα emission. In M92, I found 9 stars with Hα emission out of 64 objects. Emission above the continuum in the Hα profile can be seen in Figures 3.10 and 3.11. For comparison, Figure 3.11 includes a star that exhibits no emission. The color-magnitude diagram

Table 3.2. B/R ratio of Hα Line for Stars with Emission Wings in M15

ID No.	B/R 2005 May 22	B/R 2006 May 11	B/R 2006 October 4	B/R 2006 October 7
B5	no emission	···	no emission	> 1
B6	no emission	> 1	no emission	no emission
B30	no emission	no emission	> 1	> 1
GEB 254	···	···	···	> 1
K144	···	> 1	no emission	> 1
K158	···	> 1	···	···
K224	> 1	> 1	> 1	···
K238	···	···	···	> 1
K260	< 1	> 1	···	···
K341	< 1	> 1	> 1	> 1
K393	> 1	···	···	···
K421	···	···	> 1	···
K431	no emission	> 1	> 1	···
K447	···	< 1	···	···
K462	···	< 1	···	···
K479	···	···	···	< 1
K482	···	···	> 1	···
K582	< 1	···	···	···
K672	···	···	> 1	···
K702	no emission	> 1	···	···
K709	···	···	···	> 1
K757	> 1	> 1	···	···
K825	···	···	< 1	···
K853	> 1	no emission	···	···
K875	> 1	no emission	···	···
K969	> 1	···	···	< 1
K979	< 1	···	···	···
K1029	> 1	no emission	···	···
K1040	···	···	> 1	···

Note. — The parameter B/R is the intensity ratio of Blue (short wavelength) and Red (long wavelength) emission peaks. The symbol ··· indicates the star was not observed. If B/R ratio is > 1 the line profile indicates inflow, if B/R ratio is < 1 the line profile indicates outflow.

(CMD) for each night of observation appears in Figure 3.12 for both clusters. The intensity ratio, B/R, of Blue (short wavelength) and Red (long wavelength) emission peaks for stars showing emission is contained in Table 3.3.

In M13, emission is found in stars brighter than V=14.69, corresponding to $M_V = +0.21$, using the apparent distance modulus $(m - M)_V = 14.48$ from Harris (1996). The star which marks the faint luminosity limit (L719) appears to be either a blend, or a physical binary, and not an RGB star judging from its position on the CMD (bluer than RGB stars at the same absolute magnitude). This star also had a significant radial velocity change between observations (see Section 3.1.2). Among the RGB stars, L1073 at V=12.88 ($M_V = -1.60$) marks the faint luminosity limit of Hα emission. Stars brighter than this are on the RGB or AGB; the evolutionary status cannot be determined from the CMD itself. Stars in M92 that show emission are brighter than V=14.54 ($M_V = -0.1$), using the apparent distance modulus $(m-M)_V = 14.64$ from Harris (1996). However the faintest star (IX-12) showing emission appears to be an AGB star, according to its position on the CMD. Considering stars on the RGB, the star IV-94 (V=13.06, $M_V = -1.58$)

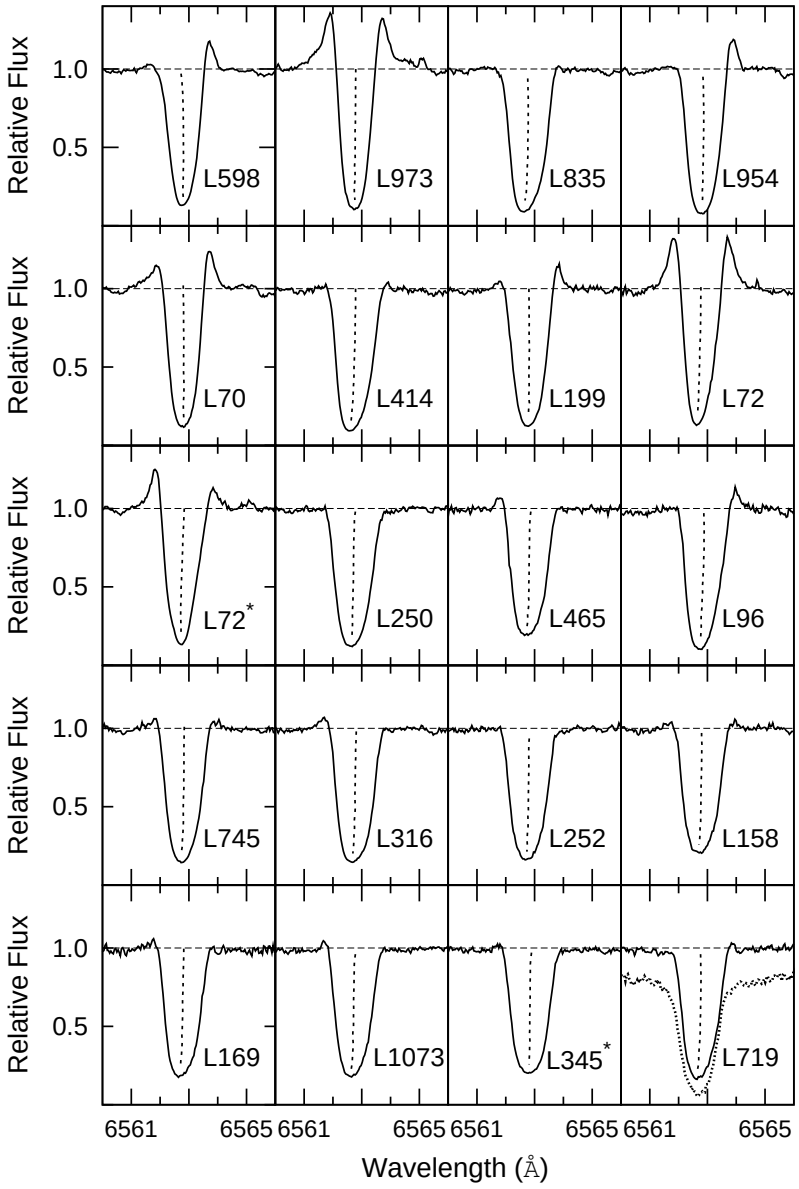

Figure 3.10: *Normalized spectra of red giants in M13 which showed emission in Hα on 2006 March 14. Stars marked with ∗ were observed on 2006 May 10. The dashed line marks the bisector. The emission of one star, L719, disappeared between observations, and the spectrum is overlaid here using a dotted line. The spectra are arranged in order of decreasing brightness; the brightest is at the top left and the stars become fainter from left to right. The wavelength scale is corrected for heliocentric velocity. The radial velocity of M13 is* -243.5 ± 0.2 *km* s^{-1}.

appears to be the faintest RGB star showing emission in M92 (although the differences between the RGB and AGB at that part of the CMD are very small). In M15, the faint luminosity limit showed significant changes between observations; this amounted to a change in the faint magnitude limit of 0.79 magnitudes (Mészáros et al., 2008). One can assume that the emission behaves very similarly in these clusters as well, and that the faint luminosity limit of Hα emission is not constant.

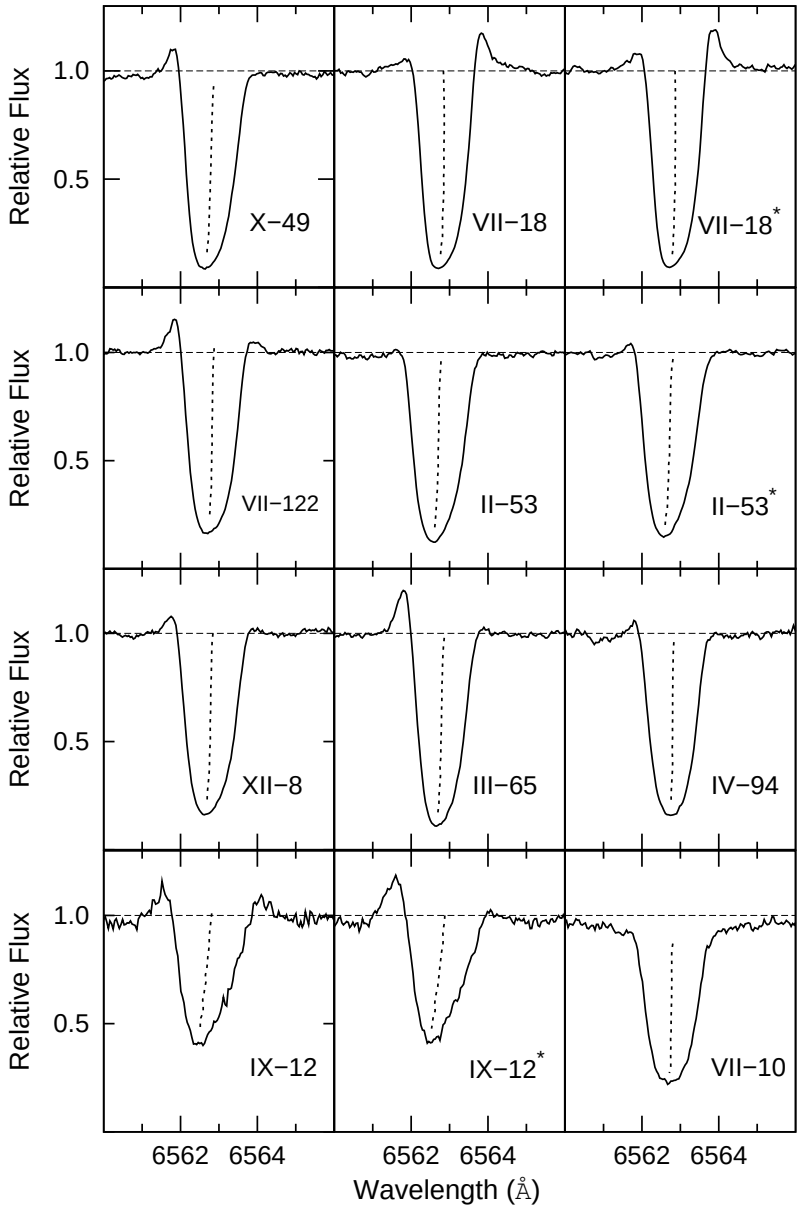

Figure 3.11: *Normalized spectra of red giants in M92 which showed emission in Hα on 2006 May 7. Stars marked with ∗ were observed on 2006 May 9. XI-19 is an example of an Hα profile without emission. For explanation please see Figure 3.10 caption. The radial velocity of M92 is* -118.0 ± 0.2 *km* s^{-1}.

For comparison on a luminosity scale, unreddened colors for M13 and M92 stars were calculated. Foreground reddening [$E(B-V) = 0.02$ for both clusters] and the apparent distance modulus were taken from Harris (1996). The effective temperatures, bolometric corrections, and luminosities were obtained from the $V-K$ colors (Tables 7.5 and 7.6) using the empirical calibrations by Alonso et al. (1999, 2001) and the cluster average metallicity [Fe/H]=−1.54 for M13, [Fe/H]=−2.28 for M92 (Harris, 1996). Thus on the red giant branch alone, emission appears in stars brighter than $\log(L/L_{\odot}) = 2.79$ in M13 and $\sim 78\%$ of these stars (18) show Hα emission. In M92 this luminosity limit is slightly

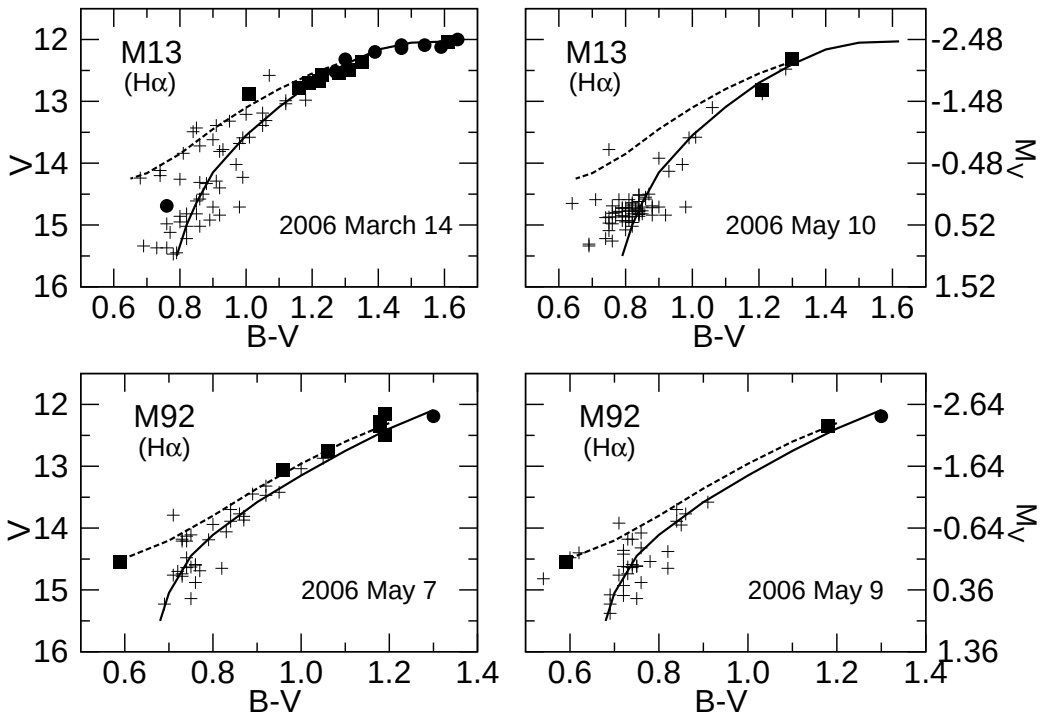

Figure 3.12: *Color-magnitude diagrams for all M13 and M92 stars observed in 2006. Stars with Hα emission and with B<R (indicating outflow) are marked with filled circles; stars with B>R emission wings (suggests inflow) are denoted by filled squares. The solid line shows the fiducial curve of the RGB; dashed lines show the fiducial curve of the AGB for M13 and M92 from observations of Sandage (1970).*

lower than in M13, $\log(L/L_{\odot}) = 2.74$, and also $\sim 78\%$ of these stars (7) show emission.

Although both clusters were observed on two different days, the configurations were chosen to eliminate stars already observed in order to achieve full coverage of stars on the CMD. When it was possible, previously observed stars were configured to the remaining fibers, but the number of stars observed twice for both clusters is very small, only 17 in M13 and 15 in M92. Of the stars showing Hα emission, comparison was possible for only two stars in M13 and three stars in M92. In M13, between 2006 March 14 and 2006 May 10, L72 changed asymmetry (see Figure 3.10), while for the other star, L719, the already weak emission vanished. In M92, all three stars (II-53, VII-18, and IX-12) kept the same emission asymmetry, but the flux level of IX-12 changed in only two days (see Figure 3.11).

3.4 The Hα Line Bisector

3.4.1 M15

The core of the Hα line is formed higher in the stellar chromosphere than the line wings and is expected to give an indication of the atmosphere dynamics. I first measured

Table 3.3. B/R ratio of Hα Line for Stars with Emission Wings in M13 and M92

	M13			M92	
	B/R	B/R		B/R	B/R
ID No.	2006 March 14	2006 May 10	ID No.	2006 May 7	2006 May 9
L70	< 1	···	II-53	> 1	> 1
L72	< 1	> 1	III-65	> 1	···
L96	< 1	···	IV-94	> 1	···
L158	> 1	···	VII-18	< 1	< 1
L169	> 1	···	VII-122	> 1	···
L199	< 1	···	IX-12	> 1	> 1
L250	> 1	···	X-49	> 1	···
L252	> 1	···	XII-8	> 1	···
L316	> 1	···			
L345	···	> 1			
L414	< 1	···			
L465	> 1	···			
L598	< 1	···			
L719	< 1	no emission			
L745	> 1	···			
L835	< 1	···			
L954	< 1	···			
L973	> 1	···			
L1073	> 1	···			

Note. — The parameter B/R is the intensity ratio of Blue (short wavelength) and Red (long wavelength) emission peaks. The symbol ··· indicates the star was not observed. If B/R ratio is > 1 the emission wings indicate inflow, if B/R ratio is < 1 the emission wings indicate outflow.

the position of the Hα absorption line core for stars in M15 relative to photospheric lines using the IRAF task *splot*. I found an error in the wavelength scales depending on the aperture number that prevented measurement of the core offset of Hα to better than $\pm$ 2 km s^{-1} . At present, we believe that the different light path of the ThAr comparison lamp from that of the stellar spectra causes this error, which appeared as a variable 'stretching' of the wavelength scale dependent on aperture and zenith distance of M15. This 'stretching' effect appeared in the spectra of stars in M13 and M92 from observations taken in 2006. Since this discovery, new observational procedures have been instituted with Hectochelle using sky spectra to eliminate these effects. A new reduction method is also being developed at CfA to correct for this effect in spectra taken before the new observational procedures.

Thus, a better approach to the velocity differences consists of measuring the line asymmetry using a line bisector. The difference between the centers of the line core and of the line near the continuum level gives a measure of the atmospheric dynamics through the chromosphere. To accomplish this, the line profile was divided into 20 sectors in normalized flux. The top sector was usually between 0.7 and 1.0 of the continuum in the normalized spectrum, the lowest sector was placed $0.01 - 0.05$ above the lowest value of the line depending on its signal-to-noise ratio. The actual position of the top and the lowest sector depended on the S/N ratio of the spectra, giving the longest bisectors for

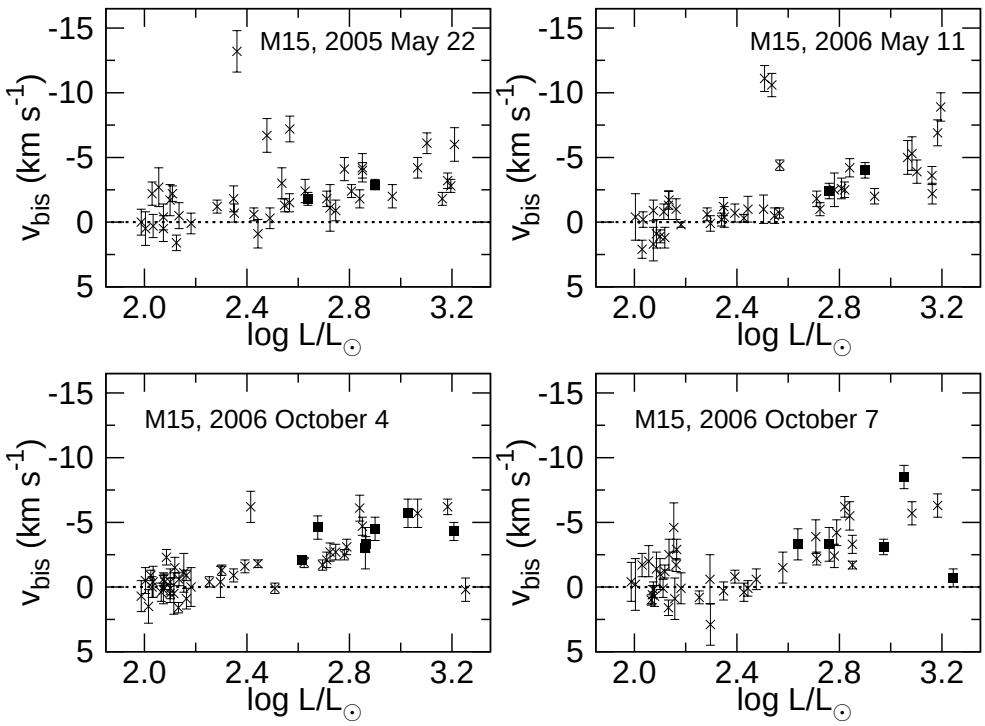

Figure 3.13: *The velocity difference ($v_{\rm bis}$) between the top and the bottom of the bisector of Hα as a function of luminosity for stars in M15. Negative values indicate a blueshifted core (outward motion), positive values denote a red shifted core (inward motion). A predominant outward motion sets in near log $L/L_\odot \approx 2.4$ and increases in velocity towards more luminous stars. Dusty giants identified with Spitzer Space Telescope (Boyer et al., 2006) and observed with Hectochelle, are denoted by squares. See Section 4.1 for discussion of the outlying stars between log $L/L_\odot$=2.3 and 2.6 with velocities more negative than -10 km s^{-1} which appear to be AGB stars.*

the brightest stars. The velocities of the Hα bisector asymmetry ($v_{\rm bis}$) are calculated in the following way: the top and the bottom 3 sectors are selected, the wavelength average of each sector is calculated, then subtracted one from another and changed to a velocity scale. The bisector velocities, $v_{\rm bis}$, are shown in Figure 3.13 and listed in Appendix Table 7.8. A negative value corresponds to an outflowing velocity. Probable errors for these measurements were formally calculated and range from 0.5 km s^{-1} to 1.5 km s^{-1} for the brightest to faintest stars respectively. Stars fainter than log $(L/L_\odot) = 2.5$ (V $\approx$ 14.20) did not show Hα asymmetry and $v_{\rm bis}$ was nearly zero. Stars brighter than log $(L/L_\odot) = 2.5$ (V $\approx$ 14.20) showed asymmetry and in almost every case the line profile was blue shifted. This magnitude limit is comparable to the luminosity limit of stars showing emission, however stars with a blue shifted Hα core did not always show emission wings. The core velocity evidently is a more sensitive diagnostic of outflows. The amplitude of $v_{\rm bis}$ correlates with the luminosity (Figure 3.13). Where AGB stars are well separated in color from the RGB stars, near log $L/L_\odot$=2.3 to 2.6, the AGB stars exhibit larger values of $v_{\rm bis}$ and more variability than RGB stars (Figure 3.15). At higher luminosities, where the AGB and RGB objects can not be distinguished from

one another on the CMD, the bisector velocities are all significantly higher than stars at fainter magnitudes on the RGB.

3.4.2 M13 and M92

To search for mass motions in the chromosphere for stars in M13 and M92, I evaluated the Hα core asymmetry using the bisector method described earlier in Section 3.4.1.

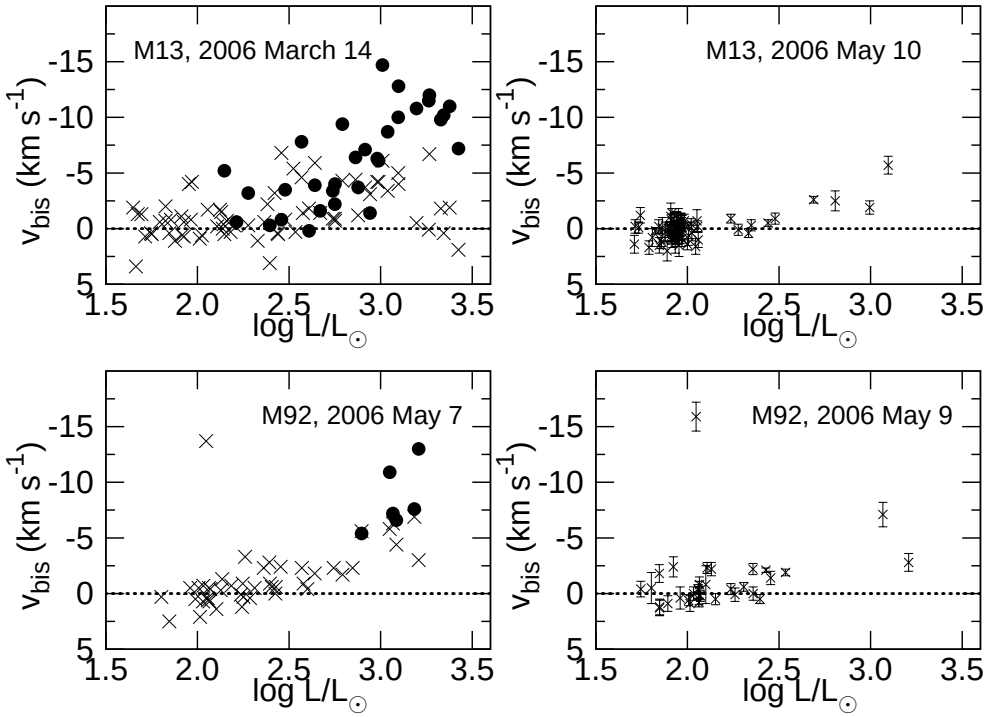

Figure 3.14: *The velocity difference ($v_{\rm bis}$) between the top and the bottom of the bisector of Hα ($\times$) and the coreshift of the Ca II K central reversal absorption (filled circle) as a function of luminosity for stars in M13 and M92. All Ca observations from different days are plotted together on the left side panels. Negative values indicate a blueshifted core (outward motion), positive values denote a red shifted core (inward motion). The error bars in figures on the left side were eliminated to display the differences between Hα and Ca II K. A predominant outward motion sets in near $logL/L_{\odot} \approx 2.5$ in both clusters and increases in velocity towards higher luminosity. The velocity of the Ca II K central reversal formed higher in the chromosphere than the Hα core, is generally larger than the bisector velocity of Hα at the same luminosity, indicating that the expansion velocity increases with height in the chromosphere.*

The bisector velocities, $v_{\rm bis}$, are shown in Figure 3.14 and listed in Tables 7.9 and 7.10. A negative value corresponds to an outflowing velocity. The error of the majority of the measurements spanned 0.5−1.0 km s^{-1} ; only stars fainter than V=15 magnitude exceeded 1.0 km s^{-1} in measurement error. RGB stars fainter than log $(L/L_{\odot}) = 2.5$ did not show asymmetry in the Hα core and $v_{\rm bis}$ was nearly zero. This luminosity is nearly the same for both clusters and also very similar to M15 (Mészáros et al., 2008), which suggests that the luminosity limit of the line core asymmetry marking the onset of expansion does

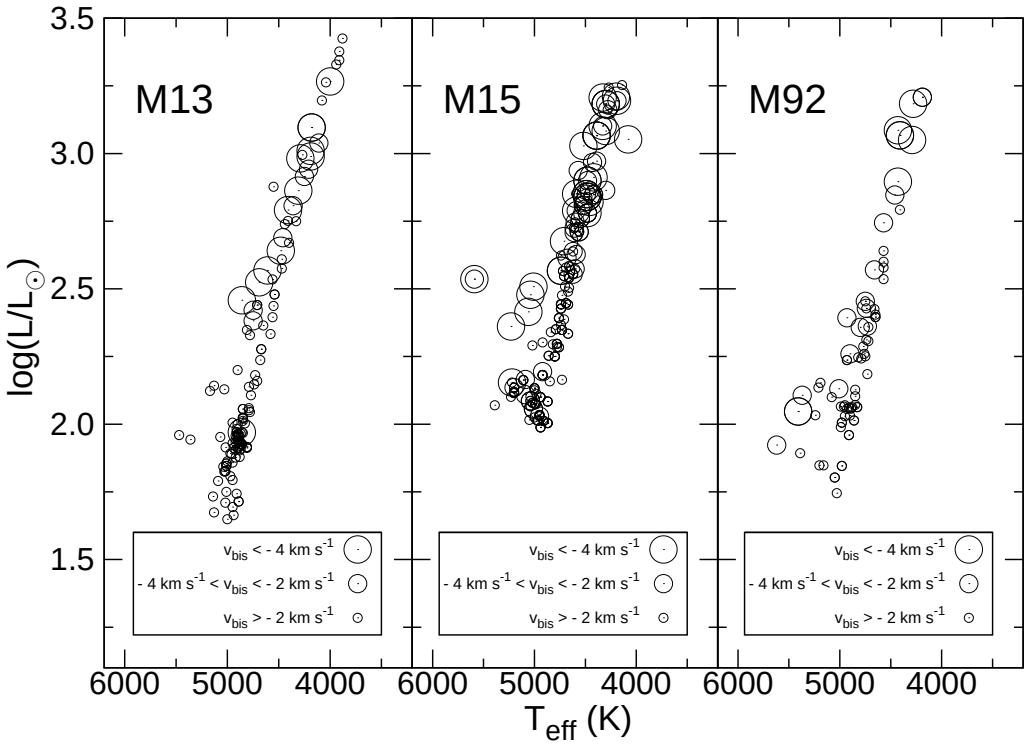

Figure 3.15: *Temperature-luminosity diagram for all stars observed in all clusters, where the size of the circle indicates the velocity of the Hα bisector asymmetry. Big circle:* $v_{\rm bis} < -4$ *km s*$^{-1}$*, medium circle:* -4 *km s*$^{-1} < v_{\rm bis} < -2$ *km s*$^{-1}$*, small circle:* $v_{\rm bis} > -2$ *km s*$^{-1}$ *. Concentric circles indicate multiple observations of the same star.*

not depend on average cluster metallicity. Stars brighter than log $(L/L_{\odot}) = 2.5$ showed core asymmetry and the majority of the bisectors were blue shifted.

The start of chromospheric outflow presumably relates to mass loss. However, the value of $v_{\rm bis}$ appears to depend on luminosity. In the metal-rich cluster M13, $v_{\rm bis}$ increases with luminosity and reaches its maximum value (≈ 5 km s^{-1}) at about log $(L/L_{\odot}) = 3.2$ but the most luminous stars exhibit lower (near zero km s^{-1}) values. In the more metal-poor cluster M92, $v_{\rm bis}$ also increases with luminosity and reaches the maximum value at log $(L/L_{\odot}) = 3.4$ but the decrease in outflow velocity is much smaller. At the same luminosity, $T_{\rm eff}$ for the metal-rich M13 giants is lower than for M92. Thus, the apparent decrease in $v_{\rm bis}$ at high luminosity would appear to be related to the changing atmospheric structure (see Section 4.1).

Where AGB stars are well separated in color from the RGB stars in M92, the AGB stars exhibit larger values of $v_{\rm bis}$ than RGB stars (Figure 3.15). The star IX-12 in M92 shows the largest bisector velocity at $v_{\rm bis} = -15.9 \pm 1.3$ km s^{-1}, and this star is the faintest star showing emission in the cluster (see Figure 3.11). Its position on the CMD suggests that this star is an AGB star (Figure 3.12). AGB stars in M13 generally have lower bisector velocities than AGB stars in M92 which suggests that the metal-rich objects have slower winds.

3.5 Ca II K profiles

3.5.1 M15

Spectra of 53 red giant stars in M15 in the Ca II H&K region were obtained in 2005 and the profiles of the Ca II K core (λ3933) are shown in Figure 3.16 for most stars showing emission.

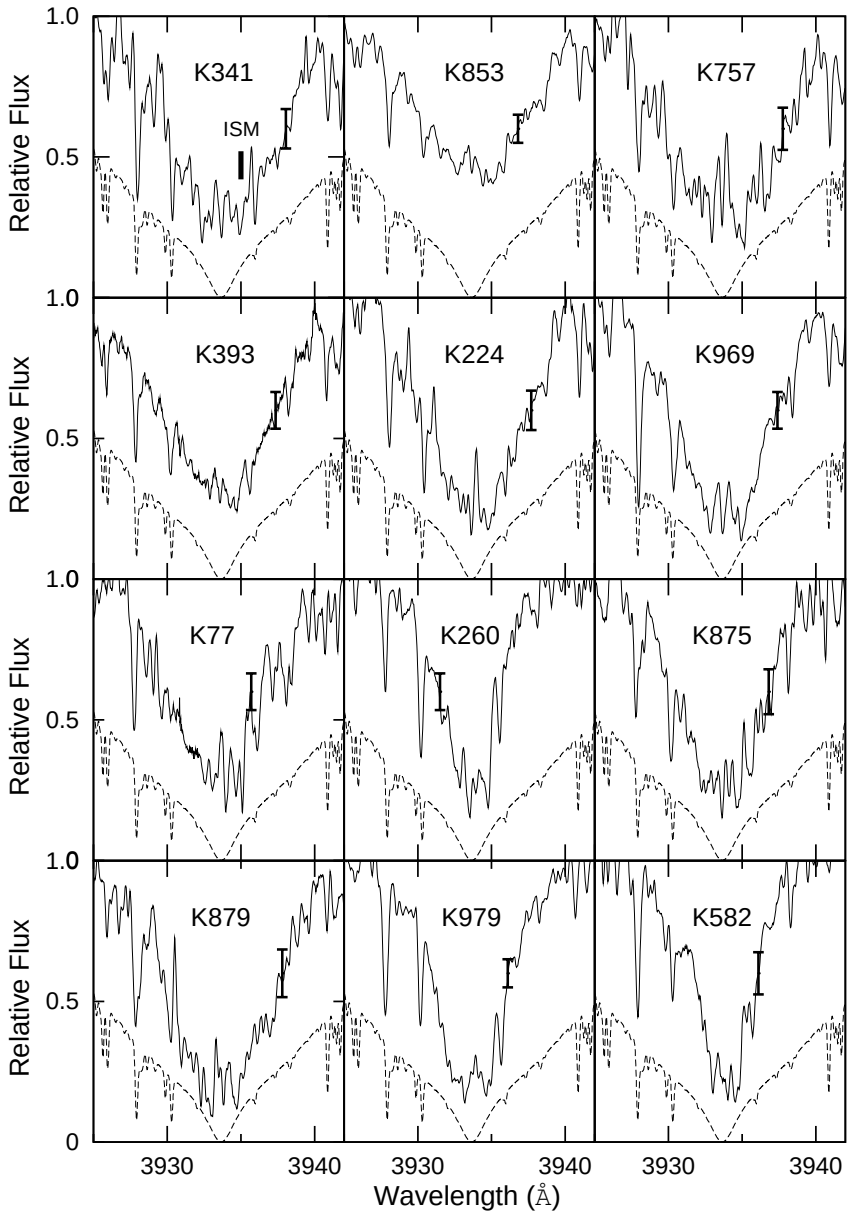

Figure 3.16: *Spectra of some red giants in M15 which showed emission in Ca II K. The observed spectra are shifted up by 0.1. The Kurucz model of K341 is denoted by a dashed line. The spectra are arranged in order of decreasing V magnitude; the brightest is at the top left and the stars become fainter from left to right. The spectra are smoothed to make the spectral features more visible. Error bars show the photon noise in the original, unsmoothed spectra. The line marked ISM denotes absorption by the interstellar medium.*

Table 3.4. B/R ratio of Ca II K Line for Stars Showing Emission in M15

ID No.	B/R 2005 May 23
K77	> 1
K224	< 1
K260	> 1
K341	> 1
K393	> 1
K582	< 1
K702	not clear
K757	< 1
K853	> 1
K875	1
K879	> 1
K969	1
K979	not clear
K1029	not clear

Note. — The parameter B/R is the intensity ratio of Blue (short wavelength) and Red (long wavelength) emission peaks.

Two other stars, K702 and K1029, not shown in these figures, exhibit Ca emission too. The spectra had low signal to noise ratio (S/N $\approx 15 - 20$ in the continuum and $\approx 5 - 10$ in the core) due to the 20 minutes exposure times used, and it is difficult to identify emissions in many cases.

Continuum normalization is challenging in this spectral region because spectral synthesis demonstrates that hundreds of absorbing lines generally depress the continuum substantially. A low order Chebyschev function was used to fit and normalize the local continuum away from the strong Ca II lines. In many stars, the noise may be comparable to the emission in the core of the K line, preventing measurement of the radial velocity of the central self-absorption in almost all spectra.

The presence of emission is determined by eye by comparison to the synthesized spectrum of K341 constructed with the Kurucz code (Kurucz, 1993) using the physical parameters described in Section 3.1.1. This model spectrum contains only photospheric lines and no chromosphere was included in the model, thus making it excellent for detection of emission. It is clear that the stellar spectrum in the line core does not reach zero flux as would be expected in such a deep photospheric line. Some additional counts in the core may come from the inaccurate sky subtraction.

I found fourteen stars out of 53 stars where Ca II K emission is definite or highly likely. Eleven of these stars showed Hα emission when measured one day earlier in 2005. In the 11 stars where the Ca asymmetry is obvious, the ratio of the blue to the red side of the Ca K emission core (the core asymmetry) could be assessed (see Table 3.4) and in 6 out of the 11 cases, the core asymmetry differed from the asymmetry as noted in Hα .

3.5.2 M13 and M92

Spectra in the Ca II H&K region were obtained for 119 red giant stars in M13 and 63 red giants in M92. The profiles of the Ca II K core (λ3933) are shown in Figures 3.17 and 3.18 for all stars exhibiting emission. Identifying emission was easier in these spectra because of the increased exposure times (40 minutes) introduced in 2006 observations.

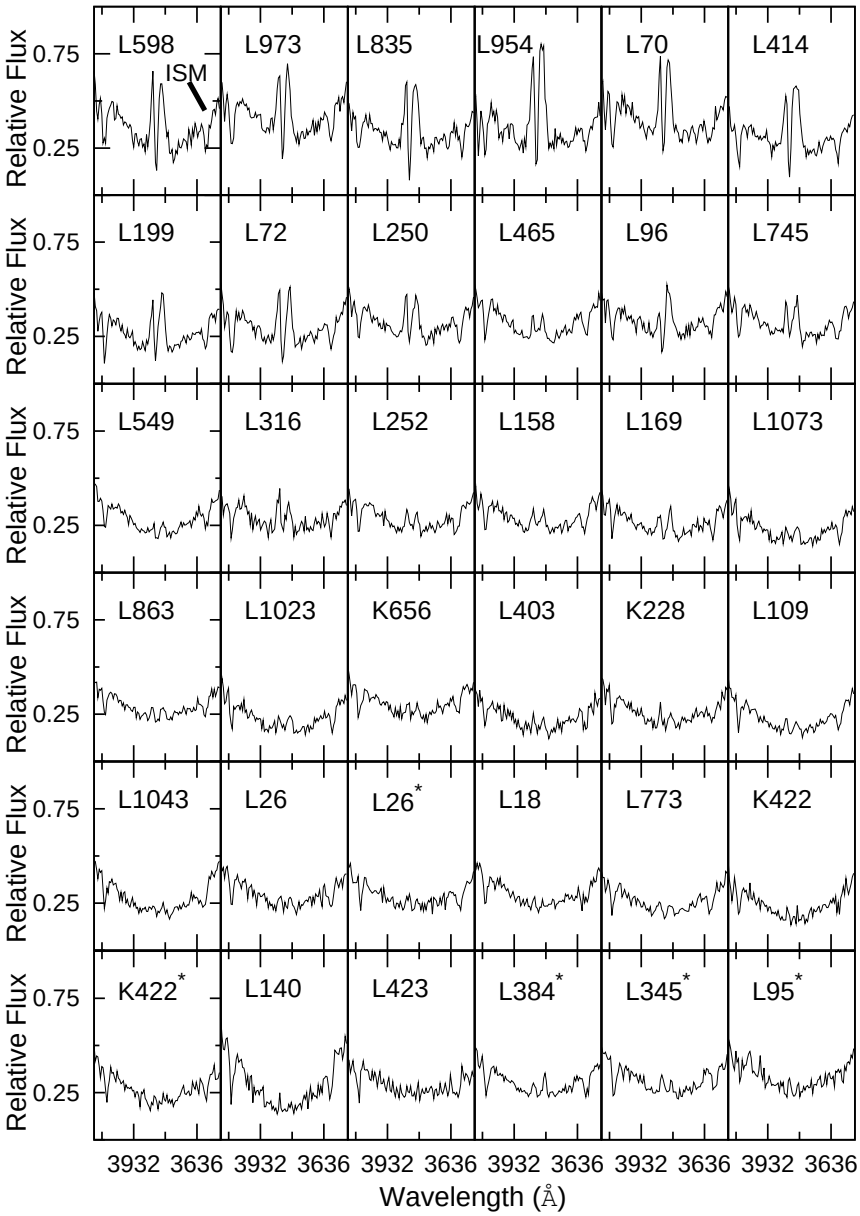

Figure 3.17: *Spectra of the brightest red giants in M13 which showed emission in Ca II K on 2006 March 14. The spectra are smoothed by 3. The spectra are arranged in order of decreasing brightness; the brightest is at the top left and the stars become fainter from left to right for a single date. The object names marked by stars were observed on 2006 May 10. The wavelength scale is corrected for heliocentric velocity. The line marked ISM in the spectrum of L598 denotes absorption by the interstellar medium and can be recognized in the other spectra.*

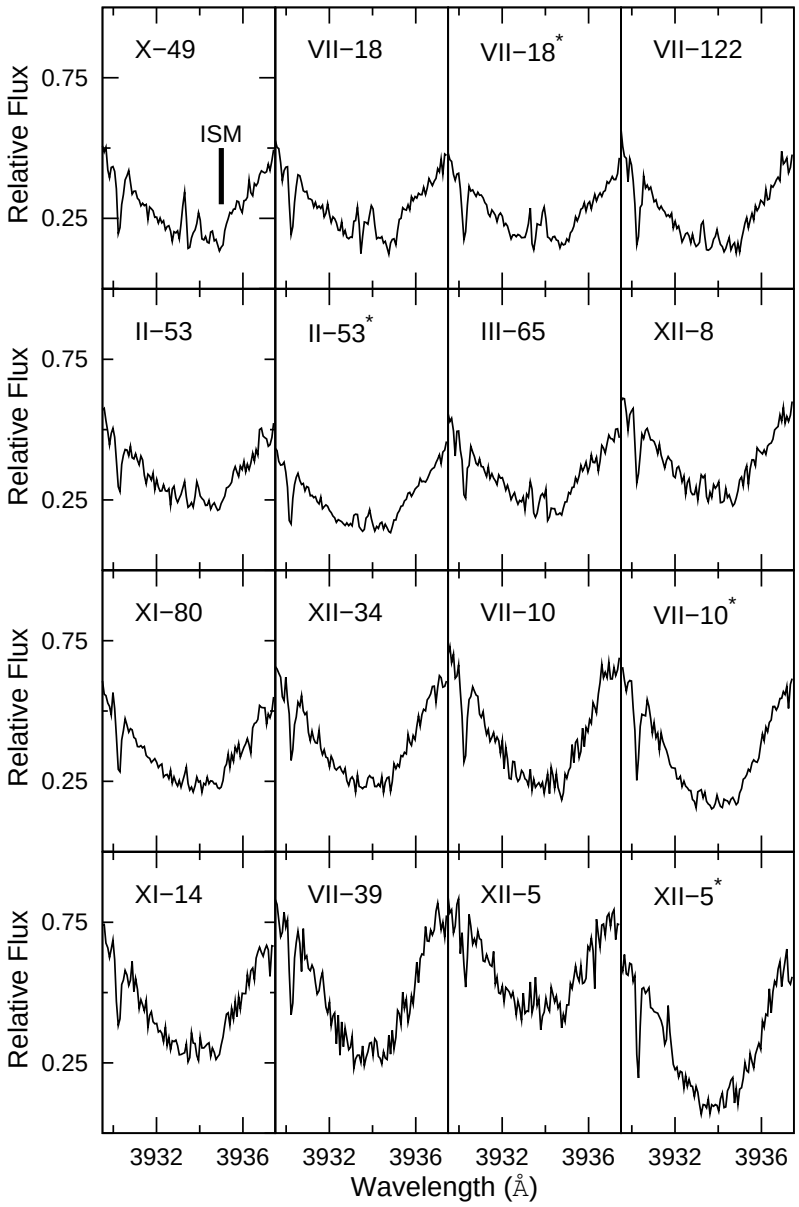

Figure 3.18: *Spectra of the brightest red giants in M92 which showed emission in Ca II K on 2006 May 7. The object names marked by stars were observed on 2006 May 9. Observations obtained on 2006 May 7 have generally lower S/N due to bad sky conditions and resulted in a higher Ca K core of XII-5, the faintest star in our sample. Additional explanation can be found in the caption of Figure 3.17.*

The position of these stars on the CMD can be seen in Figure 3.19. The intensity ratio of the emission core, B/R (B signifies the short-wavelength emission peak and R the long-wavelength emission peak), is summarized in Table 3.5. Because of the high radial velocity of M13 ($v_{\rm rad}$=−243.5 km s^{-1}), absorption by the local interstellar medium (ISM) is well away from the Ca II K core. Although the ISM is closer to the Ca II K emission in M92 ($v_{\rm rad}$=−118.0 km s^{-1}), it does not affect the emission profile. Red giant stars have low flux levels near 3950 Å, hence the deep photospheric absorption in Ca II H&K

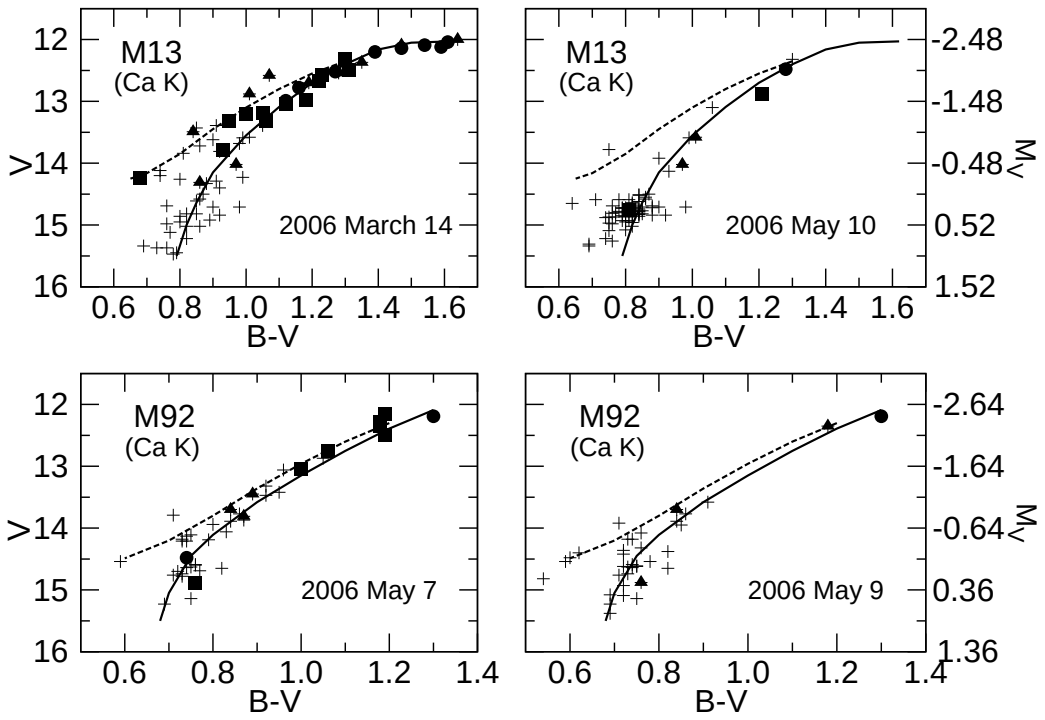

Figure 3.19: *Color-magnitude diagrams for all M13 and M92 stars observed. Stars with Ca II K emission and with B<R (indicating outflow) are marked with circles; stars with B>R emission wings (suggests inflow) are denoted by squares and stars with B≈R are marked with triangles. The solid line shows the fiducial curve of the RGB; dashed lines show the fiducial curve of the AGB for M13 and M92 from observations of Sandage (1970).*

causes the photon noise to become comparable to the flux of the core emission for stars fainter than 14th magnitude. Determining the presence of emission for the faintest stars is challenging. The spectra of our targets were compared to a Kurucz model, [computed by Coelho et al. (2005) without a chromosphere], to verify the emission. Altogether 34 stars showed Ca II K emission in M13 and 12 in M92.

The spectra of Hα and Ca II were obtained on the same night or separated by 1 or 2 days, and the asymmetry of the K-line emissions is similar to that found in Hα for the majority of the stars. The brightest stars in M13 showed stronger Ca II K emission than stars in M92 at the same luminosity. This results because the lower effective temperatures of M13 giants increase the contrast of the emission to the continuum. For stars fainter than V=14, the ratio of the blue to the red side of the Ca II K emission core, or even the presence of the emission is difficult to determine.

The velocity of the central reversal (K_3) was measured for the brightest stars (Table 3.5) using three strong absorption lines closest to Ca II K as a photospheric reference. A Gaussian function using the IRAF task *splot* was fitted to the cores of the photospheric lines and the central reversal absorption of Ca II K. Radial velocities of the photospheric lines were averaged and then subtracted from the radial velocity of the Ca II K_3 feature. The velocity shift of the K_3 absorption lies between 0 km s^{-1} and -16 km s^{-1} (Table 3.5).

Table 3.5. B/R ratio and Relative Radial Velocity of Ca II K Line for Stars Showing Emission in M13 and M92

M13				M92			
ID No.	B/R 2006 March 16	B/R 2006 May 10	v_{rel} (km s^{-1})	ID No.	B/R 2006 May 8	B/R 2006 May 9	v_{rel} (km s^{-1})
K228	> 1	···	$+0.2 \pm 0.8$	II-53	> 1	≈ 1	-7.2 ± 0.9
K422	≈ 1	≈ 1	-3.2 ± 0.9	III-65	> 1	···	-10.9 ± 0.9
K656	> 1	···	-2.2 ± 0.7	VII-10	≈ 1	≈ 1	···
L18	> 1	···	-0.3 ± 0.8	VII-18	< 1	< 1	-13.0 ± 0.4
L26	> 1	≈ 1	-3.5 ± 0.9	VII-39	< 1	···	···
L70	< 1	···	-10.2 ± 0.5	VII-122	> 1	···	-6.6 ± 0.8
L72	< 1	···	-10.0 ± 0.9	X-49	> 1	···	-7.6 ± 1.0
L95	···	> 1	···	XI-14	≈ 1	···	···
L96	< 1	···	-14.7 ± 0.9	XI-80	> 1	···	···
L109	> 1	···	-7.8 ± 1.0	XII-5	> 1	≈ 1	···
L140	> 1	···	-0.6 ± 0.6	XII-8	> 1	···	-5.4 ± 0.8
L158	≈ 1	···	-7.1 ± 0.9	XII-34	≈ 1	···	···
L169	< 1	···	-6.4 ± 0.9				
L199	< 1	···	-10.8 ± 0.8				
L250	≈ 1	···	-12.8 ± 1.0				
L252	> 1	···	-1.4 ± 0.8				
L316	> 1	···	-6.1 ± 0.7				
L345	···	> 1	···				
L384	···	< 1	···				
L403	> 1	···	-1.6 ± 0.9				
L414	< 1	···	-12.0 ± 1.1				
L423	≈ 1	···	-5.2 ± 1.1				
L465	> 1	···	-6.3 ± 0.9				
L549	≈ 1	···	-3.7 ± 1.2				
L598	≈ 1	···	-7.2 ± 0.2				
L745	≈ 1	···	-8.7 ± 0.8				
L773	> 1	···	-3.9 ± 1.1				
L835	≈ 1	···	-11.5 ± 0.9				
L863	> 1	···	-4.0 ± 1.1				
L954	< 1	···	-9.8 ± 1.1				
L973	< 1	···	-11.0 ± 0.6				
L1023	> 1	···	-3.4 ± 1.1				
L1043	≈ 1	···	-0.8 ± 0.9				
L1073	≈ 1	···	-9.4 ± 1.0				

Note. — The parameter B/R is the intensity ratio of Blue (short wavelength) and Red (long wavelength) emission peaks. Relative radial velocities were not possible to calculate where the central absorption was not visible in the spectrum.

Chapter 4

Discussion

In the first section, I discuss several characteristics of the presence of Hα and Ca II emission on the CMD. In the second section I compare the physical parameters of the Hα emission in all three observed clusters and the literature.

4.1 The Hα line

In Mészáros et al. (2008) and Mészáros et al. (2009a), I have presented Hα and Ca II K spectroscopy of 297 red giants in three globular clusters with different metallicities (Harris, 1996): M13 ([Fe/H]=−1.54), M15 ([Fe/H]=−2.26), and M92 ([Fe/H]=−2.28). The presence of emission in these transitions signals an extended, high-temperature chromosphere, and the asymmetry of the emission and the line core indicates chromospheric mass motions. Comparison of the statistics of the profile characteristics among the globular cluster stars could reveal the effects of metallicity on mass loss. Parameters of the three observed clusters and one other (NGC 2808) discussed here in detail can be found in Table 4.1. In Section 4.3, I compare my results with those of Cacciari et al. (2004) who presented similar line profiles for 137 red giants in the globular cluster NGC 2808.

4.1.1 Presence of Hα Emission

On the RGB, Hα emission sets in for all stars with $T_{\rm eff} < 4500$ K and $\log\,(L/L_{\odot}) > 2.75$ in all 3 clusters: M13, M15, and M92. It is perhaps fortuitous that the limits are so similar since the presence of Hα can change by as much as 0.79 magnitudes from observations on one date to another (Mészáros et al., 2008). Stars on the AGB show Hα emission to lower luminosity limits than the RGB objects. The faint limits of emission for AGB stars in M13 and M92 are comparable (Mészáros et al., 2009a), while AGB stars in M15 with emission are brighter. Emission is variable in all giants and again there does not appear to be a systematic dependence of luminosity limits on metallicity. This result

Table 4.1. Characteristics of Emission in Four Clusters

Cluster	[Fe/H] [a]	$log(L/L_{\odot,H\alpha,1})$ [b]	$log(L/L_{\odot,H\alpha,2})$ [c]	$log(L/L_{\odot,Ca\ K})$ [d]	No. [e]	P_1 [f]	P_2 [g]
M13	−1.54	1.95	2.79	1.92	123	45	78
M15	−2.26	2.36	2.78	2.36	110	22.5	83
M92	−2.28	2.05	2.74	1.96	64	18	78
NGC 2808[h]	−1.15	2.5	2.5	2.60	137	7	52

[a]Harris (1996).

[b]The luminosity limit of all stars showing emission in Hα.

[c]The luminosity limit of only RGB stars showing emission in Hα.

[d]The luminosity limit of all stars showing emission in Ca II K.

[e]Number of stars observed.

[f]The percentage of stars from all observations showing outflow in Hα emission wing asymmetry.

[g]The percentage of stars from all observations showing Hα emission above $log(L/L_{\odot,H\alpha,2})$.

[h]Parameters of NGC 2808 for the RGB stars were measured by Cacciari et al. (2004). No AGB stars in that sample are well-separated on the CMD. Thus the RGB limit marks the faint limit for all stars in the cluster.

suggests that whatever mechanism produces the variable emission occurs similarly in all metal-poor red giants.

The percentage of stars showing inflow and outflow in the Hα emission wings[1] varies from cluster to cluster and appears to be related to cluster metallicity. In the metal-poor M92, about 82% of stellar spectra showing emission have an inflow signature (18% show outflow) and the study of M15 (Mészáros et al., 2008) revealed that about 78% of stars with Hα emission displayed an inflow signature (22% outflow). These two clusters show similar behavior in their chromospheric dynamics. M13 has a more equal distribution of the dynamical signature with 55% of the Hα spectra indicating inflow (45% outflow). Since all the luminous stars are losing mass, it might be puzzling why the dominant emission signature in Hα is one of inflow. The line cores generally indicate outflow, which forms higher in the atmosphere. Emission wings forming in deeper regions show different motions probably related to stellar pulsation (see Section 5.3.2).

The fraction of stars showing Hα emission increases with luminosity and decreasing effective temperature. Because of the separation of red giant branches on the CMD due to metallicity, the distribution of the emission with luminosity and effective temperatures differs between clusters. At the same luminosity, the metal rich M13 exhibits more stars with Hα emission than the metal poor M92 or M15, because the effective temperatures are lower in M13 for a constant luminosity. However, at the same stellar effective temperature, M15 and M92 exhibit more stars showing emission than M13. This may appear as a metallicity effect, but it originates in the fact that both high luminosity and low effective temperature produce more Hα emission.

[1]As measured by the ratio of B/R – the short wavelength to long wavelength peaks of the Hα emission wings.

4.1.2 The Hα Bisector Velocity

Inspection of the bisector velocities reveals differences among the red giant stars. None of the stars brighter than V $\sim$ 14.5, log $(L/L_{\odot}) > 2.4 - 2.5$ have red-shifted Hα cores (Figure 3.13) in M15; all are blue-shifted or exhibit no shift at all. This luminosity cutoff corresponds also to the limit of the Hα emission wings which suggests that the blue-shift and the emission are related. The emission wings arise deep in the chromosphere as models have shown (Dupree et al., 1984; Mauas et al., 2006; Mészáros et al., 2009b), and the dynamics of the upper chromosphere are reflected in the line core. Motions start in the lower atmospheric layers and then progress outward through the chromosphere. The amount of the bisector shift increases with stellar luminosity(Figure 4.1).

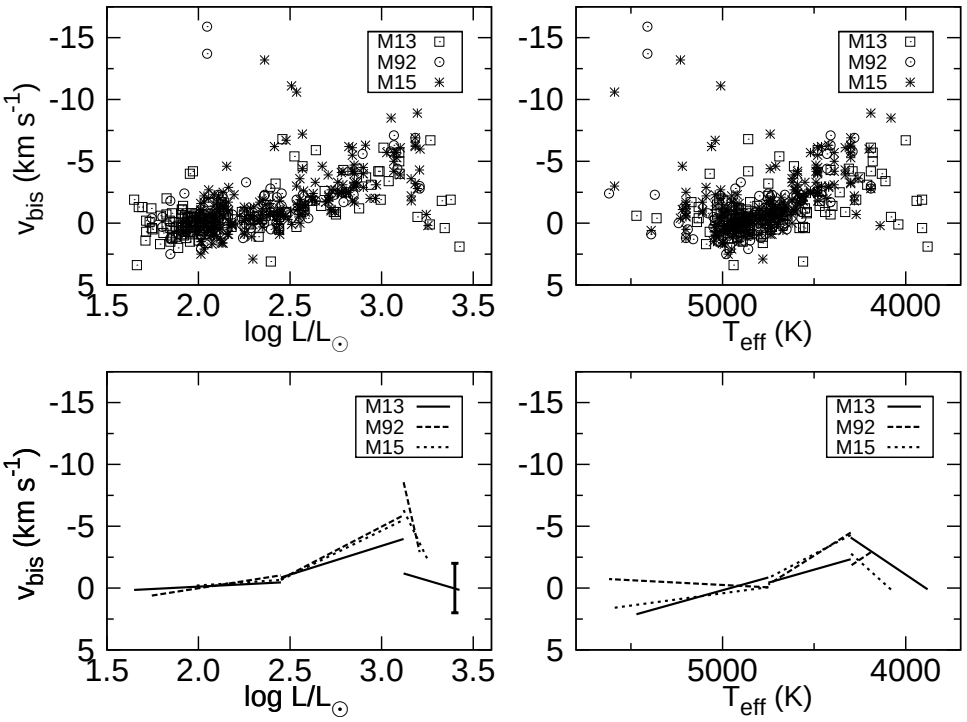

Figure 4.1: *Top left and right: The bisector velocity ($v_{\rm bis}$) of Hα for all observations in M13, M15 and M92 as a function of luminosity and effective temperature. Negative values indicate outflow. Lower left and right: To fit the results with a linear function, luminosity and effective temperature were divided into three different regions: the bottom of the RGB [log $(L/L_{\odot}) = 1.6-2.5$, $T_{\rm eff}$=4750−5700 K], where $v_{\rm bis}$ was close to zero km s^{-1} the RGB stars [log $(L/L_{\odot}) = 2.5 - 3.1$, $T_{\rm eff}$=4300−4750 K], where $v_{\rm bis}$ shows a significant increase; and the top of the RGB [log $(L/L_{\odot}) = 3.1-3.5$, $T_{\rm eff}$=3800−4300 K], where $v_{\rm bis}$ generally shows smaller values than in the middle of the RGB. The stars with high velocity near log $(L/L_{\odot}) = 2.2-2.4$ were omitted from the fit. Error bar of the top of the RGB fit for M13 is displayed in the lower left panel. The errors of the fits span between $\sim$ 1 and 2.5 km s^{-1} for each fit.*

There are several stars that show faster outflow asymmetries than the generally low-speed outflows near log $L/L_{\odot}$=2.3 to 2.6 (Figure 3.13) in M15. These stars, K158, K260, K582, K875, and K979 display bisector velocities ranging from −6.7 km s^{-1} to −13.2 km s^{-1} in comparison to the remainder of stars in that magnitude interval

where bisector velocities are typically less than -5 km s^{-1} . One of these stars, K260 showed the largest change in core-shift velocity measuring -3.0 ± 1.2 km s^{-1} in 2005 and -10.6 ± 0.9 km s^{-1} in 2006. The position of the high-outflow stars on the CMD suggests they are AGB stars since they lie blueward of the fiducial AGB in Figure 3.9. This relatively high outflows mark the presence of a substantial stellar wind in AGB stars. However, as Figure 3.15 shows, other stars near the fiducial AGB do not have high outflow velocities. If these low velocity objects are also AGB stars, then this argues for an episodic outflow.

Stars brighter than log $(L/L_{\odot}) = 2.5$ show a blue-shifted Hα core in both M13 and M92, and outflows become faster with increasing luminosity (Figure 3.14) (Mészáros et al., 2009a). Thus, the luminosity at the onset of outflow, indicated by the Hα line core is independent of metallicity. The behavior of the bisector velocity on the RGB changes at the highest luminosities (Figure 4.1). Giants in M13, the most metal-rich cluster, show lower bisector velocities in the most luminous (and coolest stars). In fact, the velocities of the Hα core approach 0 km s^{-1} with respect to the photosphere, signaling that the outward motions have decreased in the atmospheric region where the Hα line forms. Since the brightest stars in M13 have a lower $T_{\rm eff}$ than those in M15 and M92 (Figure 4.1), I suspect that the decrease in the Hα bisector velocity results from the changing structure of the very extended atmosphere.

The Hα wing asymmetry and Ca II K asymmetry preponderantly signal outflow in the most luminous stars. It is noteworthy that outflow begins at a luminosity, log $(L/L_{\odot}) \sim$ 2.5, and as the stars become more luminous, emission wings occur in the Hα profile in our sample at log $(L/L_{\odot}) \sim 2.75$. I conjecture that the onset of pulsation marked by the observed outward motion leads to a warmer chromosphere producing emission wings in Hα.

Differences in the coreshift between AGB and RGB stars can be seen where these stars are distinct on the CMD in M13 and M92, too. Stars on the AGB, between log $(L/L_{\odot}) =$ 2.0 and 2.7, showed slightly larger bisector velocities than RGB objects in both clusters, although the values are most extreme in M92. AGB stars tend to have lower values of log g and smaller escape velocities in the chromosphere as compared to RGB stars, which makes them more sensitive to mass loss driving mechanisms resulting in faster winds. It is also possible that there is more heating in the hotter AGB stars; it may be that a putative magnetic field is stronger after the stars have been through helium burning enabling enhanced wave motions, heating, and acceleration in the chromosphere as compared with RGB stars. The extremes of outflow velocity on the AGB tend to be larger in the metal-poor clusters, M15 and M92, than in M13 (see Figures 3.15 and 4.1).

There is no evidence here that the outflow velocity is slower at low metallicity. This suggestion resulted from observations of OH/IR stars in the low metallicity Magellanic Clouds (Marshall et al., 2004), and modeling of dust driven winds (Helling, 2000; Wachter

et al., 2008) such as those identified in Omega Centauri by Spitzer Space Telescope observations (Boyer et al., 2008; McDonald et al., 2009). In fact, I find just the opposite. M15 and M92 have generally higher velocities than stars in M13 (see Figure 4.1, lower panels). No evidence for a 'super-wind' (Renzini, 1981; Bowen & Willson, 1991) in the sense of an abrupt high velocity outflow is present in our spectra, although the largest mass-loss rates might be expected for stars with lower T_{eff} than found in this sample (Wachter et al., 2002). Even in the dusty red giants in M15 detected with the Spitzer Space Telescope (Boyer et al., 2006), the bisector velocities have similar values as red giants without an IR excess (Mészáros et al., 2008). These similarities suggest that mass loss and dust production are not correlated, and the triggering of dust production may be an episodic phenomenon (for more details see Section 5.4).

Three stars in M13 exhibit large (>2 km s^{-1}) bisector-velocity changes between observations. The star at the lowest luminosity limit, L719, shows a 4.7 km s^{-1} bisector velocity difference, which is clearly visible on the spectrum (see Figure 3.10) as the Hα emission disappeared. K342 and K658 showed 2.2 km s^{-1} and 4.9 km s^{-1} changes respectively, but these stars are faint and the error due to the low signal-to-noise of the spectra is comparable to the velocity change.

In M92, only 2 stars show a large coreshift in Hα : II-6 is a very faint star and this difference is comparable to the error of our measurements; IX-12 is an AGB star and shows similar $v_{\rm bis}$ values as stars of the same luminosity. However between our 2 observations separated by 2 days, the coreshift changes for other stars are relatively small. In M15 (Mészáros et al., 2008), it is the AGB stars in the log $(L/L_{\odot}) = 2.3 - 3.0$ luminosity region that show large bisector velocity changes (3−7 km s^{-1}) over a time span of one year or more.

On the RGB, the velocities in M15 indicate that systematic outflow (more negative than −2 km s^{-1}) in the Hα core occurs at luminosities, log $(L/L_{\odot}) > 2.5$. The velocity of the outflow increases with luminosity and only the brightest stars show slightly smaller outflow (Figures 3.14 and 4.1). In M92, which is also very metal-poor, stars brighter than log $(L/L_{\odot}) = 2.5$ showed bisector velocities more negative than −2 km s^{-1}, and only the brightest star shows smaller outflow velocities. If there are differences in mass loss between M15 and M92, the shapes of the Hα line profiles do not reflect this. Thus the Hα line by itself cannot help to decide if mass loss is the 'second parameter' in M15 and M92. McDonald & van Loon (2007) found no significant correlation between core asymmetry and luminosity, when they examined Hα and Ca II IR triplet spectra of 47 red giant stars near the RGB tip in 6 globular clusters. Above a certain luminosity the bisector velocity of Hα becomes small and motions are difficult to detect in this region of the atmosphere, independent of cluster metallicity. Possibly another diagnostic such as He I λ 10830 or ultraviolet lines, formed higher in the atmosphere needs to be examined. A He I λ10830 absorption line was detected (Smith et al., 2004) in the star L687 in

M13, with an extension to -30 km s^{-1}, suggesting that when the helium line becomes detectable (apparently for $T_{\rm eff} \sim 4650$ K), it can give an indication of a faster wind. This He I λ10830 velocity is comparable to the higher values of the Hα bisector velocities that are found here in AGB stars. Pilachowski et al. (1996) classifies L687 as an AGB star.

4.1.3 Relating to Pulsation

The asymmetry of the Hα wings indicates that most of the giant stars have inflow motions in the region where the wings are formed in all three clusters. Since it appears likely that these stars are pulsating (Mayor et al., 1984), although this may be controversial for the metal deficient field giants (Carney et al., 2003), it is of interest to compare the asymmetry pattern with that of Cepheids which are known pulsators. One well-studied Cepheid, ℓ Car (HD 84810), shows variable emission wings in Hα similar to those found here (Baldry at al., 1997). The appearance of $B/R < 1$ asymmetry generally coincides with blue-shifted photospheric metal absorption lines; and the converse applies, when $B/R > 1$, the photospheric lines are red-shifted. So a dynamic linking clearly exists between the photosphere and the regions forming the Hα line wings. The radial velocity of this long-period (35 days) Cepheid shows photospheric red-shifts for about half of its pulsation period, and 'inflow' Hα line asymmetries for about 0.35 of its period. Inspection of radial velocity curves from metallic lines shows that longer-period Cepheids have red shifts for a greater proportion of their pulsation period (Nardetto et al., 2006; Petterson et al., 2005). Thus it is not surprising that the Hα profiles in the red giants in these clusters show a dominant inflow asymmetry.

Models for dust-free Mira stars (Struck et al., 2004) indicate that lower levels of the atmosphere can support radial pulsations which develop into a steady outflow at larger distances. A similar behavior is suggested by the outflows detected in the cores of the Hα lines for the M15 giants. Models of the Hα line profiles for metal deficient giants show that the core is formed at a mass column density substantially above the region forming the wings (Dupree et al., 1984; Mauas et al., 2006; Mészáros et al., 2009b). Such models for red giants are needed to explore the dynamics of the atmospheres and to evaluate the mass loss rate (see Section 5).

The different proportions of inflow/outflow signatures may indicate that the pulsation period in M15 and M92 is generally longer than in M13. It is clear that variability is ubiquitous. Almost all stars brighter than V=12.5 are variables in M13, but only one variable red giant exhibits periodic photometric variations, and the remaining ones are semi-regular or irregular (Kopacki et al., 2003).

4.2 Ca II K emission

Fourteen of the red giants in M15 showed emission in Ca II K and 12 spectra are shown in Figure 3.16. The lower luminosity limit is at least the same as found for the presence of Hα emission, namely log $(L/L_{\odot}) = 2.36$. The luminosity limits of Ca II K_2 emission and Hα appear to be related. Calcium emission may well extend to fainter limits; our spectra of fainter stars did not have sufficient signal to identify emission in the center of the deep photospheric Ca II line. However, three of the stars displaying Ca II K emission do not have Hα emission, but this is not surprising since the presence of Hα emission is known to vary (see Table 3.2). While the spectra are noisy, the Ca II K asymmetries seem to include all possibilities: $B < R$, $B = R$, $B > R$. These asymmetries differ in 6 stars from the asymmetries of the Hα wing in each star. Such a difference is not unexpected since the regions of formation of the Ca K core and the Hα wings are separated in the atmosphere of a giant (Ca K_2 emission forms higher in the atmosphere than Hα wings); additionally Hα shows variations in asymmetries over a few days (Cacciari & Freeman, 1983) which could contribute to the differences.

The Ca II K_2 emission appears at lower luminosities than Hα emission in M13 and M92. [log $(L/L_{\odot}) = 1.92$ for M13 and log $(L/L_{\odot}) = 1.96$ for M92] (Mészáros et al., 2009a). In M15 (Mészáros et al., 2008) the Ca II K luminosity limit agrees with the Hα emission limit [log $(L/L_{\odot}) = 2.36$], but the low signal-to-noise ratio of those observations did not allow us to determine the presence of Ca II H&K emission in fainter stars. The lower luminosity limit of Ca II K emission does not appear to be dependent on the cluster metallicity.

The number of stars with Ca II emission in both M13 and M92 exceeds the number of stars showing Hα emission. Stars with Hα emission generally have Ca II K emission, but not all stars with Ca II K emission show Hα emission. This difference is not unexpected since the regions of formation of the Ca II K core and the Hα emission wings are separated in the atmosphere of a giant. Models suggest that Ca II K emission forms lower in the atmosphere than Hα wings (Dupree, 1986). Additionally Hα shows variations in asymmetries over the span of a few days (Cacciari & Freeman, 1983; Mészáros et al., 2008, 2009a) which could contribute to the differences. Some stars in both clusters were observed twice at Ca II. Changes in Ca II K emission were observed in two stars in M13 and four stars in M92 where the line profile of Ca II K, either changed asymmetry or the emission strengthened or weakened, or both.

The outflow velocities of the Ca II K_3 reversal are generally larger than the bisector velocities of the Hα line for the same stars (Figure3.14). Similar behavior was found by Zarro & Rodgers (1983) in Population I giants and supergiants, and they concluded from the similarity of line profiles that Ca II K line is formed higher in the atmosphere and the increased outward velocity reflects a mass-conserving outflow. While models of

the Sun suggest that the Ca II K_3 feature forms in a higher atmospheric region than the core of the Hα line (Avrett, 1998), some chromospheric models of metal-deficient giants (Dupree, 1986; Mauas et al., 2006) locate the approximate depth of formation of the Ca II K_3 feature below that of the Hα core. These models would suggest the opposite conclusion from Population I stars, that the flow is decelerating in the upper atmosphere. Yet another model (Dupree et al., 1992) for the metal-deficient giant HD 6833 finds the contribution function of Ca II K_3 to lie above that of the Hα core and hence signal an accelerating outflow. Some ambiguity may exist in the definition of the region of formation, and in addition it can extend over a substantial height in the chromosphere. In some cases, the He I λ 10830 line, clearly formed above both Ca II K and Hα shows even higher outflow velocities in metal-deficient stars (Dupree et al., 1992; Smith et al., 1995), so the accelerating outflow models appear preferable.

4.3 Globular Clusters

A detailed spectroscopic study (Cacciari et al., 2004) was made of 137 RGB stars in NGC 2808 which extended to $\sim$ 3 magnitudes below the tip of the red giant branch. The majority of their targets were at lower resolution than I have here, however 20 were sampled at high resolution. Emission in Hα was detected down to a limit of $\log(L/L_\odot) = 2.5$ which is about 0.25 magnitude brighter than I find in M15. NGC 2808 is more metal rich ([Fe/H]=-1.15, Harris (1996)) than M15 ([Fe/H]=-2.26, Harris (1996)) which may account for the slight difference. On the other hand, the distance modulus for M15 was recently determined to be 15.53$\pm$0.21 using the zero-age horizontal branch level as a distance indicator (Cho & Lee, 2007) which would bring the luminosities into closer agreement. In the Cacciari et al. (2004) spectra taken at highest resolution, the red giants in NGC 2808 have wing emission in Hα indicative of inflow ($B/R > 1$) in the majority of stars, similar to our results. Other surveys generally contained only the brightest stars in the clusters, and their luminosity limits extend only to $\log(L/L_\odot) = 2.7$ (Bates et al., 1993; Lyons et al., 1996). Smith & Dupree (1988) noted Hα emissions in metal-poor field giants brighter than $\log(L/L_\odot) = 2.5$.

While the luminosity limits of the Hα emission are similar in M15 and NGC 2808, the distribution of the emission with luminosity and effective temperatures differs between the clusters. By comparing the fraction of stars with Hα emission in M15 from this study with NGC 2808 (Cacciari et al., 2004), I find that at the same luminosity, the M15 giants exhibit a lower percentage of Hα emissions than is found in NGC 2808. However, at the same effective temperature, the fraction of stars showing emission is the opposite; fewer stars have emission at the same effective temperature in NGC 2808 than in M15. Although the fraction of stars with emission generally increases with luminosity, the differences result principally because the CMD for NGC 2808 (which is more metal

rich than M15) lies at lower effective temperatures at the same luminosity. Assessing the emission fraction as a function of stellar radius suggests that the fractions are comparable except at large values of the stellar radius. Possibly the coolest stars can not support the thick chromosphere necessary to produce emission (Dupree et al., 1984; Mauas, 2007) and/or the pulsational characteristics of the atmospheres differ.

A better comparison can be made with the metal rich cluster, M13. However, this comparison may be somewhat compromised since NGC 2808 has an extreme case of peculiar horizontal branch morphology (Lee et al., 2005) and a split main sequence with potentially 3 populations (Piotto et al., 2007), making it one of the most persuasive clusters for the existence of possible multiple stellar populations including a super helium-rich component (Lee et al., 2005; D'Antona & Caloi, 2008). These features of NGC 2808 make it quite different from M13 – the metal rich cluster in our sample. M13 has a more chemically homogeneous population, although it is conjectured to consist of predominantly second generation stars (D'Antona & Caloi, 2008). The average metallicity of NGC 2808 ([Fe/H]=−1.15) is higher than M13 ([Fe/H]=−1.54), by a factor of 2.5.

The detection threshold for Hα emission on the RGB in NGC 2808, of log $(L/L_{\odot}) = 2.5$ is fainter by ∼0.2 magnitudes than the limits for M13, M15, and M92 (see Table 4.1). Since the appearance of emission in the Hα line varies with time, these limits are comparable, one with another. However, the percentage of red giants exhibiting emission is less at 52% than I find for M13, M15, and M92 where the value is about 80%. The atmospheres of the NGC 2808 giants may be at lower temperatures since, for the same input energy, radiation losses are greater due to the increased abundance of metals than in metal-poor objects. Differences arise in the Hα outflow signature indicated by the emission wings in NGC 2808 where an exceptionally low percentage (at 7%) is found by Cacciari et al. (2004) in contrast to the 45% of red giants showing outflow in M13 and 18−22% in the metal-poor clusters, M15 and M92.

Cacciari et al. (2004) were able to measure significant core shifts of Hα in 7 stars of their sample of giants in NGC 2808 observed with the high resolution spectrograph UVES. Outflow velocities more negative than -2 km s^{-1} appear for stars brighter than log $(L/L_{\odot}) = 2.9$ but there is little velocity data for the fainter giants. More stars had measurable velocities in the Na D lines, and outflows from 1−4 km s^{-1} became apparent at log $(L/L_{\odot}) = 3.1$ and brighter. It is interesting that the 3 most luminous stars in their sample had core shifts of 1 km s^{-1} or less, similar to our results for M13 (Figure 3.14). M4, another cluster of similar metallicity as NGC 2808 also did not have coreshifts (more negative than -2 km s^{-1}) either in Hα or Na D in any of ≈10 stars that have luminosities log $(L/L_{\odot}) > 3.3$ (Kemp & Bates, 1995). By contrast, the velocities in M15 indicated systematic outflow (more negative than -2 km s^{-1}) in the Hα core occur at lower luminosities, log $(L/L_{\odot}) = 2.5$. Thus there are possible signs of a metal dependency in the outflow with higher velocities in metal poor objects. More complete

sampling of outflows in other clusters is needed.

The luminosity limit in NGC 2808 (Cacciari et al., 2004) for Ca II K emission lines is $\log (L/L_{\odot}) \sim 2.6$ which is higher than the Hα limit in NGC 2808. This result is puzzling since Ca II K is found at lower luminosities than Hα emission in the other clusters, M13, M15, and M92. The resolution of the Calcium spectra studied by Cacciari et al. (2004) was the lowest of all their spectra at R=19600, and the signal-to-noise in the line core for the brightest stars was only 15. So it is possible that Calcium was not detected in the fainter targets. The limit for Ca II K in NGC 2808 is $\sim$0.2 magnitudes brighter than found in M15 which is a metal-poor cluster. The 2 metal poor clusters, M15 and M92 differ in the Ca II K limit by 0.4 magnitudes. At present, there is not sufficient evidence to claim that the B/R ratio of Ca II K emission varies night to night as the B/R ratio of Hα emission. The core shift of Ca II K in NGC 2808 is generally more negative than the value for Hα, similar to that found here for the most luminous stars (Figure 3.14).

Since both the Hα emission and emission wing asymmetries are variable, it is difficult to draw firm conclusions about systematic differences between clusters. In the sample of red giants in NGC 2808 studied by Cacciari et al. (2004), a lower fraction of stars was found with Hα emission and with outflow signatures in the emission wings than in the more metal-poor clusters (M13, M15, M92). However, the dynamical characteristics including the luminosity onset of outflow and wind speeds, appear indistinguishable among these clusters.

Chapter 5

The Stellar Wind

In the first section of this chapter I give a very brief overview of spectral line formation in stellar atmosphere. In the second section I describe my calculations of model spectra, then compare them with observations in the third section. In the fourth and last section I discuss the Hectochelle observations and model calculations of dusty red giant stars in M15 previously discovered by the *Spitzer* Space Telescope.

5.1 Stellar Atmospheres

5.1.1 Basic Equations

A stellar atmosphere is often defined as a transition region from the stellar interior to the interstellar medium. The stellar atmosphere can be described as the temperature change with height. This way there are four main regions often defined: subphotosphere, photosphere, chromosphere, and corona. The major portion of the visible spectrum comes from the photosphere. In the case of the Sun, the temperature drops from the bottom of the photosphere to the top of it, then it increases slightly through the chromosphere, while in the corona the temperature increase is significant compared to the chromosphere. The effective temperature, which is used to characterize a photosphere, is defined in terms of the total power per unit area radiated by the star:

$$\int_0^\infty F_\nu \, d\nu \;=\; \sigma \, T_{eff}^4 \tag{5.1}$$

where $\sigma = 5.67 \times 10^{-5}$ erg/(s cm^2 deg^4) is the Stefan-Boltzmann constant, F_ν is the total flux leaving the stellar surface, $T_{\rm eff}$ is the temperature of a black body having the same power output per unit area as the star.

At the bottom of the photosphere, the density is high enough to prevent any photons from escaping. In this region, the material is close to thermodynamic equilibrium, nearly

as many photons headed into the star as there are headed outwards. This means that the radiation is nearby that of a black body. Higher in the atmosphere the optical depth is lower and as the height increases, more and more photons can escape from the atmosphere. There is a continuous transition between local thermodynamic equilibrium (LTE) deep in the photosphere to complete non-equilibrium (non-LTE) high in the chromosphere.

In order to investigate how spectral lines are formed and how we detect light properties, some basic radiations terms and definitions must be made. The specific intensity of radiation I_ν (erg cm^{-2} s^{-1} Hz^{-1}) is defined as:

$$I_\nu \;=\; \frac{dE_\nu}{dA\ dt\ d\omega\ d\nu\ cos\theta} \tag{5.2}$$

The specific intensity is the monochromatic energy dE_ν passing through unit area (dA) per unit time (dt), per unit solid angle ($d\omega$), and per unit frequency ($d\nu$). In model atmosphere computations, I_ν is obtained from the transfer equation. The mean intensity, J_ν, is defined as the directional average of the specific intensity:

$$J_\nu \;=\; \frac{1}{4\pi}\oint I_\nu\ d\omega \tag{5.3}$$

The flux is defined as the net energy flow across unit area per unit time and unit frequency interval:

$$F_\nu \;=\; \frac{\int E_\nu}{dA\ dt\ d\nu} \tag{5.4}$$

The flux can be related to intensity through Equation 5.2:

$$F_\nu \;=\; \oint I_\nu\ cos\theta\ d\omega \tag{5.5}$$

5.1.2 The Source Function

The intensity of light is exponentially diminishing upon passing through a small thickness of material which is so cool that it does not emit light itself. The amount of lost intensity dI_ν is:

$$dI_\nu \;=\; -\kappa_\nu\ \rho\ I_\nu\ dx \tag{5.6}$$

where ρ is the mass density, κ_ν is the absorption coefficient in units of erg/(s rad^2 Hz g). There are two physical processes contributing to the absorption coefficient. The first is the true absorption, where the photon is destroyed and the energy is thermalized. The second is the scattering, where the photon is deviated in direction and removed from the solid angle being looked at.

The optical depth (τ_v) depends on both dx and $\kappa_\nu\ \rho$ and is defined between distance

0 and l as:

$$\tau_\nu \;=\; -\int_0^l \kappa_\nu \;\rho \; dx \tag{5.7}$$

Note that the optical depth is measured inward from the surface. With the optical depth Equation 5.6 can be written in a simple format:

$$dI_\nu \;=\; I_\nu \; d\tau_\nu \tag{5.8}$$

The emission can be defined very similarly to the absorption. The intensity emitted in a specified direction is:

$$dI_\nu \;=\; j_\nu \; \rho \; dx \tag{5.9}$$

The emission coefficient j_ν has the same units as the absorption coefficient. Similarly to the absorption, there are two physical processes contributing to j_ν: first is the real emission, second the scattering of photons into the direction being considered.

The ratio of emission and absorption coefficients is called the source function:

$$S_\nu \;=\; j_\nu/\kappa_\nu \tag{5.10}$$

This source function is used to calculate the transfer of radiation and it can be extremely complicated.

5.1.3 The Transfer Equation

The majority of energy transported through the photosphere is done via radiation. The radiative energy transport problem describes how the physical parameters of the material are contributing to the observed spectrum. Putting both absorption and emission together, one gets the change in specific intensity (dI_ν) over an increment of path length (dx):

$$dI_\nu \;=\; -\kappa_\nu \; \rho \; I_\nu \; dx \;+\; j_\nu \; \rho \; dx \tag{5.11}$$

By dividing this by the optical depth, $\kappa_\nu \; \rho \; dx$, and using Equation 5.9, the equation of radiative transfer becomes,

$$dI_\nu/d\tau_\nu \;=\; I_\nu \;-\; S_\nu \tag{5.12}$$

The transfer equation has a formal solution, which can be written in the form of:

$$I_\nu(\tau_\nu) \;=\; \int_0^{\tau_\nu} S_\nu(t_\nu) \; e^{-(\tau_\nu - t_\nu)} \; dt_\nu \;+\; I_\nu(0) \; e^{-\tau_\nu} \tag{5.13}$$

This equation means that at a point of τ_ν, the original intensity, $I_\nu(0)$, suffers an ex-

ponential extinction $e^{-\tau_\nu}$, and at the same time, intensity generated at any point of t_ν, which is called $S_\nu(t_\nu)$ here, also undergoes an exponential extinction $e^{-(\tau_\nu - t_\nu)}$ before being summed at the point τ_ν. In order to solve this equation, $S_\nu(t_\nu)$ must be known, which is in a general case a complicated function. If we suppose LTE, then S_ν becomes the Planck function, $B_\nu(T)$, and knowing T as a function of τ gives the solution to the transfer equation.

5.1.4 Plane-parallel Atmosphere

In most stars, the photosphere is very thin compared to the radius of the star. If this is true, then a plane-parallel approximation can be made, which means that the θ angle is constant with height along the direction of I_ν. With introducing the parameter $\mu = cos\theta$, the transfer equation in a plane-parallel atmosphere becomes:

$$\mu \; dI_\nu/d\tau_\nu \;=\; I_\nu \;-\; S_\nu \tag{5.14}$$

The formal solution to this equation can be separated to inward ($\mu < 0$) and outward ($\mu > 0$) directions:

$$I_\nu^-(\tau_\nu, \mu) \;=\; -\int_0^{\tau_\nu} S_\nu(t_\nu) e^{-(t_\nu - \tau_\nu)/\mu} \; dt_\nu/\mu \tag{5.15}$$

$$I_\nu^+(\tau_\nu, \mu) \;=\; \int_{\tau_\nu}^{\infty} S_\nu(t_\nu) e^{-(t_\nu - \tau_\nu)/\mu} \; dt_\nu/\mu \tag{5.16}$$

In most model atmospheres hydrostatic equilibrium is assumed, which means that the atmosphere is not undergoing large-scale accelerations compared to the surface gravity. The hydrostatic equation is defined as:

$$\frac{dP}{d\tau_\nu} \;=\; \frac{g}{\kappa_\nu} \tag{5.17}$$

where P is the pressure, g is the surface gravity.

5.1.5 Line and Continuum Transitions

The bound-bound transitions between the lower l and upper u energy levels of a an atom, ion or molecule are described by the Einstein coefficients. There are five Einstein coefficients defined:

- A_{ul}: the transition probability for spontaneous deexcitation from state u to state l per sec per particle in state u,

- B_{lu}: the transition probability for radiative excitation from state l to state u per sec per particle in state l,
- B_{ul}: the transition probability for induced radiative deexcitation from state u to state l per sec per particle in state u,
- C_{lu}: number of collisional excitations from state l to state u per sec per particle in state l,
- C_{ul}: number of collisional deexcitations from state u to state l per sec per particle in state u.

If collosional processes can be ignored, the source function can be given as a function of the Einstein coefficients through the absorption and emission coefficients:

$$S_\nu \;=\; j_\nu/\kappa_\nu \;=\frac{n_u A_{ul}\psi(\nu-\nu_0)}{n_l B_{lu}\phi(\nu-\nu_0)-n_u B_{ul}\chi(\nu-\nu_0)} \tag{5.18}$$

where $\psi(\nu-\nu_0)$ is the area−normalized profile shape for absorption, $\phi(\nu-\nu_0)$ is the area-normalized profile shape for spontaneous emission, $\chi(\nu-\nu_0)$ is the area-normalized profile shape for induced emission.

The meaning of these profile shapes is shown through the spontaneous absorption. In the absence of collisions and any other transitions, the mean lifetime of particles in state u is $\Delta t = 1/A_{ul}$, the corresponding energy spread is $\Delta\nu = \gamma^r/(2\pi)$, where $\gamma^r = 1/\Delta t$ is the radiative damping constant. The broadening process defines an emission probability distribution $\psi(\nu-\nu_0)$ around the line center at $\nu = \nu_0$, which is given by the area-normalized Lorentz profile:

$$\psi(\nu-\nu_0) \;=\; \frac{\gamma^r/4\pi^2}{(\nu-\nu_0)^2+(\gamma^r/4\pi)^2} \tag{5.19}$$

Bound−free transitions occur when ions are present in the atmosphere. For hydrogen and hydrogen−like ions, the bound-free transition is given by Kramers' formula:

$$\sigma_\nu^{bf} \;=\; 2.815\cdot 10^{29}\frac{Z^4}{n^5\nu^3}g_{bf} \tag{5.20}$$

where n is the principal quantum number of the level i from which the atom is ionized, Z is the ion charge, and g_{bf} is the dimensionless Gaunt factor. For more complex ions than hydrogen-like ones, the bound-free cross-sections do not have such a simple dependence of frequency, but peaks occur at resonances caused by other electrons of the same shell.

The free-free transitions also contribute to the continuum, where the emission or absorption of radiation by free electrons, when they are accelerated or decelerated, respectively, can occur at any frequencies.

5.1.6 LTE

The definition of LTE is to assume the validity of all thermodynamic equilibrium distribution laws at local temperature. In LTE, all atomic level populations are given by the Saha-Boltzmann statistics defined by the local temperature. The Boltzmann distribution is given by:

$$\frac{n_{(r,s)}}{n_{(r,t)}} = \frac{g_{(r,s)}}{g_{(r,t)}} e^{-(E_{(r,s)}-E_{(r,t)})/kT} \tag{5.21}$$

where $n_(r,s)$ the number of atoms per cm^3 at energy level of s of ionized stage r, $g_(r,s)$ is the statistical weight of level s in ionized stage r, $E_(r,s)$ is the excitation energy of level s of ionized stage, r measured from the ground level.

The Saha distribution gives the population ratio between the ground levels of successive ionization stages:

$$\frac{n_{(r+1)}}{n_r} = \frac{2g_{(r+1)}}{N_e g_r} (\frac{2\pi m_e kT}{h^2})^{3/2} e^{-E_r/kT} \tag{5.22}$$

where N_e is the electron density, m_e is the electron mass, $n_{(r+1)}$ and n_r are the population densities of two successive ionization stages, E_r is the ionization energy (minimum energy needed to free an electron from the ground state) of stage r.

The Saha-Boltzmann distribution gives the LTE population ratio between a particular level i and ion state c to which it ionizes:

$$\frac{n_c}{n_i} = \frac{2g_c}{N_e g_i} (\frac{2\pi m_e kT}{h^2})^{3/2} e^{-E_{ci}/kT} \tag{5.23}$$

where n_i is the total population density of level i, n_c is the number of ions in ionization level c, and E_{ci} is the ionization energy from level i to state c.

Because these distributions hold in LTE, the source function becomes the Planck function:

$$S_\nu = B_\nu(T) = \frac{2h\nu^3}{c^2(e^{h\nu/kT}-1)} \tag{5.24}$$

Knowing the source function in LTE, the spectrum emerging from a plan-parallel atmosphere can be calculated from Equation 5.14, if one knows the temperature distribution as a function of optical depth.

5.1.7 non-LTE

LTE holds only in deep photospheres, where the photons fully participate in the thermodynamics of the gas. This is possible if the radiation field in Planckian and the source function is dominated by collisions. Since outward energy transport is present in every star, true thermodynamic equilibrium does not exist in nature.

In non-local thermodynamic equilibrium the populations are permitted to differ from

the Saha-Boltzmann distribution values at any point through the atmosphere. For simplicity statistical equilibrium is assumed, which means that the level populations and the radiation field do not vary with time:

$$\frac{dn_i}{dt} \;=\; \sum_{j\neq i}^{N} n_j P_{ji} \;-\; n_i \sum_{j\neq i}^{N} P_{ij} \;=\; 0 \tag{5.25}$$

where n_i is the population on level i, N is the total number of levels. The transition rates P_{ij} for radiative and collisional processes are given per particle in state i or j by:

$$P_{ij} \;=\; R_{ij} + C_{ij} \tag{5.26}$$

where R_{ij} is the radiative rate per particle, which for bound−bound transitions is given by:

$$R_{ij} \;=\; A_{ij} + B_{ij} J_{\nu 0} \tag{5.27}$$

The rates P_{ij} depend on J_ν, thus I_ν in other directions, while the source function depends on the populations of lower and upper levels involved in the transitions. Further more, the populations may depend on other transitions and other populations again, thus any transition may be influenced by other transitions in the same, or in any other atoms. This is why the source function can be very complex, because the coupling between populations and radiation is non-linear and non-local.

The general line source function is usually described with the help of the departure coefficients. The departure coefficients are defined as:

$$b_l \;=\; n_l / n_l^{LTE} \qquad b_u \;=\; n_u / n_u^{LTE} \tag{5.28}$$

where n_l and n_u are the actual populations of lower and upper levels, and n_l^{LTE} and n_u^{LTE} are the populations in LTE given by the Saha-Boltzmann distribution. For bound-bound transitions, the source function becomes:

$$S_\nu^{bb} \;=\; \frac{2h\nu^3}{c^2} \; \frac{\psi\phi}{\dfrac{b_l}{b_u} e^{h\nu/kT} - \dfrac{\chi}{\phi}} \tag{5.29}$$

For bound−free transitions:

$$S_\nu^{bf} \;=\; \frac{2h\nu^3}{c^2} \; \frac{\psi\phi}{\dfrac{b_i}{b_c} e^{h\nu/kT} - \dfrac{\chi}{\phi}} \tag{5.30}$$

5.2 Modeling with Pandora

Semi-empirical models discussed in this section were calculated with the program PANDORA[1] (Avrett & Loeser, 2003). This program deals with time-dependent and one-dimensional atmosphere in either plane-parallel or spherical case. This model atmosphere is divided into layers specified by the user; these layers can be stationary or can be moving relative to each other.

The general calculations needs a temperature and density distribution given through the atmosphere. If these are set, the non-LTE energy level populations of various atoms and ions can be calculated. The statistical equilibrium equations determine the populations at any layer in the atmosphere. Through the radiative transfer equation, the radiation in that layer depends on the populations throughout a large surrounding volume. The coupled transfer and statistical equilibrium equations are solved for the populations and the radiative intensities at any point in the atmosphere. For a single line transition, this is the two-level transfer problem, for more difficult atoms with more interacting line transitions, this is the multi-level transfer problem.

PANDORA proceeds by iterations. It solves the non-LTE radiative transfer, the statistical and hydrostatic equilibrium equations for a specified multi-level transfer problem in every iteration, then stops. This way the solution can be supervised closely and further changes to the input model can be applied to achieve a better solution. In semi-empirical modeling one calculates an input atmosphere model, then compares the output spectrum with the observation. A good solution usually requires many new iterations, restarts after changing the input model.

5.2.1 Target Stars

Observations of Hα in a total of 297 red giant stars in M13, M15, and M92 were obtained in 2005 May, 2006 May, and 2006 October with the Hectochelle on the MMT (Mészáros et al., 2008, 2009a) with a spectral resolution of about 34,000. To investigate the dependence of the mass loss rate on luminosity, temperature, and metallicity, I chose RGB stars from each cluster that had clear Hα emission and a range of at least a factor of two in luminosity. The sample of stars includes different intensity ratios of the Hα emission wings, B/R^2, and the bisector velocities varied ($v_{\rm bis}$) from -0.7 to -8.9 km s^{-1}. To monitor the mass loss changes in time, one star in M13 (L72), one in M92 (VII-18), and three stars in M15 (K341, K757, and K969) were selected which have multiple observations. One star without Hα emission was also selected from each cluster to extend the sample to lower luminosities and higher temperatures. In the study of M15 Mészáros

[1]A detailed description of the program can be found on the following website: http://www.cfa.harvard.edu/ avrett/pandora.html.

[2]B signifies the short-wavelength emission peak and R the long-wavelength emission peak.

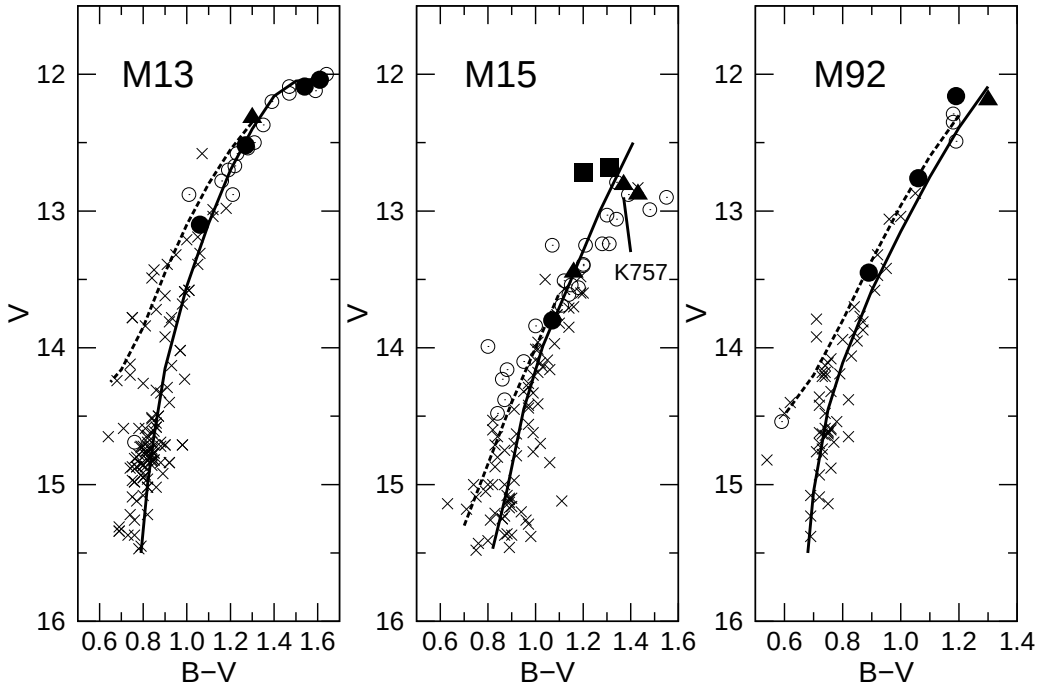

Figure 5.1: *Color-magnitude diagram for all stars observed in M13, M15 and M92. Stars with Hα emission are marked by open circles. Filled symbols mark the stars modeled in this paper, where stars observed once are marked by filled circles, stars observed more than once are marked by filled triangles, and stars observed with Spitzer (Boyer et al., 2008) are marked by filled squares. The solid line shows the fiducial curve of the RGB; the dashed line traces the fiducial curve of the AGB for M13 and M92 taken from observations of Sandage (1970), and for M15 taken from observations of Durrell & Harris (1993).*

et al. (2008) found no signature of different outflows or chromospheric structure between the 'dusty' stars identified by the *Spitzer* Space Telescope (Boyer et al., 2006) and normal RGB objects. Modeling of the Hα profile could reveal dynamical differences, if present. Two AGB stars in M15 with excess dust (K421, K479) were selected for modeling to investigate whether the mass loss of these stars differs from the rest. The color magnitude diagram (CMD) of the cluster members and targets for modeling can be seen in Figure 5.1; target stars are listed in Table 5.1.

A total of 15 stars was selected including from 4 to 6 in each of the 3 globular clusters; five stars had multiple spectra so that I could estimate changes in the mass loss rate from the Hα profiles. Unreddened colors for M13, M15, and M92 stars were calculated using the foreground reddening and the apparent distance modulus from the catalog of Harris (1996). The effective temperatures, bolometric corrections, and luminosities were obtained from the V−K colors using the empirical calibrations by Alonso et al. (1999, 2001) and the cluster average metallicity (Harris, 1996) [Fe/H]=−1.54 for M13, [Fe/H]=−2.26 for M15, [Fe/H]=−2.28 for M92 [see Mészáros et al. (2008, 2009a) for more details].

Table 5.1. Physical Parameters of Modeled Stars

ID No. [a]	Cluster	[Fe/H]	B−V	V	T_{eff} (K)	log $L/L_\odot$	$R/R_\odot$	log g [b] (cm s^2)
L72	M13	−1.54	1.30	12.32	4180	3.096	65.7	0.71
L96	M13	−1.54	1.27	12.52	4190	3.010	59.1	0.80
L592	M13	−1.54	1.06	13.10	4460	2.689	36.0	1.23
L954	M13	−1.54	1.54	12.09	3940	3.329	96.6	0.38
L973	M13	−1.54	1.61	12.04	3910	3.377	103.0	0.32
K87	M15	−2.26	1.07	13.80	4610	2.708	34.5	1.27
K341	M15	−2.26	1.37	12.81	4300	3.183	68.6	0.67
K421	M15	−2.26	1.20	12.72	4330	3.207	69.5	0.66
K479	M15	−2.26	1.31	12.68	4270	3.244	74.6	0.60
K757	M15	−2.26	1.43	12.88	4190	3.195	73.2	0.61
K969	M15	−2.26	1.16	13.45	4590	2.851	41.1	1.11
VII-18	M92	−2.28	1.30	12.19	4190	3.208	76.3	0.41
X-49	M92	−2.28	1.19	12.16	4280	3.184	71.2	0.48
XII-8	M92	−2.28	1.06	12.76	4430	2.896	47.7	0.83
XII-34	M92	−2.28	0.89	13.45	4660	2.570	29.6	1.24

[a]Ludendorff (1905) is the identification for stars in M13, Kustner (1921) is the identification for stars in M15, and Sandage & Walker (1966) is the identification for stars in M92.

[b]The gravity was calculated assuming M=0.8$M_\odot$ for each star.

5.2.2 Static Chromosphere

Two separate photospheric models were calculated with ATLAS (Kurucz, 1993), one for stars in M13 and one for stars in M15 and M92. In order to create the initial photospheric models, I used log g=0.45, [Fe/H]=−2.45, T=4275 K for the metal poor stars, and log g=0.5, [Fe/H]=−1.5, T=4500 K for the metal rich stars. Although the photospheric parameters of the target stars are different, this does not affect the calculated line profiles, because the Hα line forms in the extended warm chromosphere. The model atmospheres were represented by 72 depths, where the photospheric distribution was given by the original Kurucz values at the innermost 12 points.

For the emission line calculations, I changed the parameters at the outer depths to represent a chromosphere with the temperature increasing linearly with decreasing mass column density [ZMASS (g cm^{-2})]. Examples of these chromospheres can be seen in Figure 5.2 (*upper panels*) as a function of depth index. In every model I assumed the stellar radius to be equal to 70$R_\odot$ and a microturbulent velocity of 4 km s^{-1} at each point of the atmosphere. I assumed that every star has a mass of 0.8 $M_\odot$, and g is also a constant parameter. This way the models depend on three free parameters: 1) the column mass and temperature where the chromosphere starts; 2) the slope of the T−ZMASS function; 3) the highest temperature (T_{max}) and the lowest ZMASS values of the chromosphere, where the transition region starts. For further simplicity, the column mass and temperature where the chromosphere starts, and the mass column density where the chromosphere stops were also fixed. A transition region with a maximum temperature 2×10^5 K was added to every model in the last 10 points to obtain small optical depths as

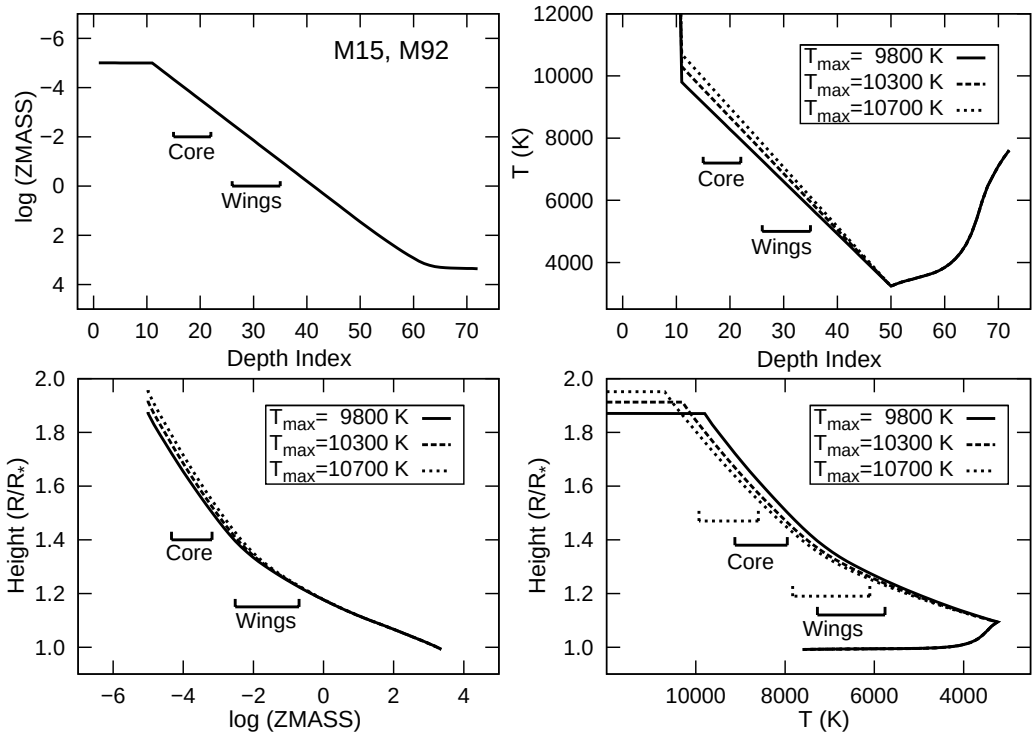

Figure 5.2: *Top left and right: The mass column density and temperature of three selected input models as a function of depth index. The atmosphere was sampled with 72 points, the mass column density was kept the same in every input model. The depth index equals 0 at the top of the chromosphere and increases downward through the chromosphere and the photosphere. The line formation regions were determined from the maximum values of the contribution to the line profile. Lower left and right: The height of the chromosphere as a function of mass column density and temperature. The height was calculated assuming a R=70$R_\odot$ radius. The Hα core forms between depths 16-21 (8000−9900 K, depending on T_{max}); the wings form between depths 24-35 (5800−7800 K, depending on T_{max}).*

hydrogen becomes completely ionized. The chromosphere was represented at 50 points linearly distributed in T vs. log ZMASS, which was sufficient to sample in detail the region where the Hα wings and core form.

For every T-ZMASS distribution, I solved the non-LTE radiative transfer and the statistical and hydrostatic equilibrium equations, using the program PANDORA (Avrett & Loeser, 2003). By keeping the starting T-ZMASS point, and the ending ZMASS point of the chromosphere the same, the only control parameter of the input models was the T_{max} value, which established the slope of the T-ZMASS distribution. This parametrization allowed us to handle easily many different input models for the PANDORA program. These chromospheric models can be seen in Figure 5.3, and they are listed in Table 5.2. I computed the non-LTE populations of a 15−level hydrogen atom assuming the same value of the gravity, g, and [Fe/H] used in the photospheric models. All heavy elements were scaled using the metallicity used in the photospheric models and assuming the solar abundance distribution. For the continuum calculations I included all 15 bound-free transitions, and the most important bound-bound transitions and scattering that

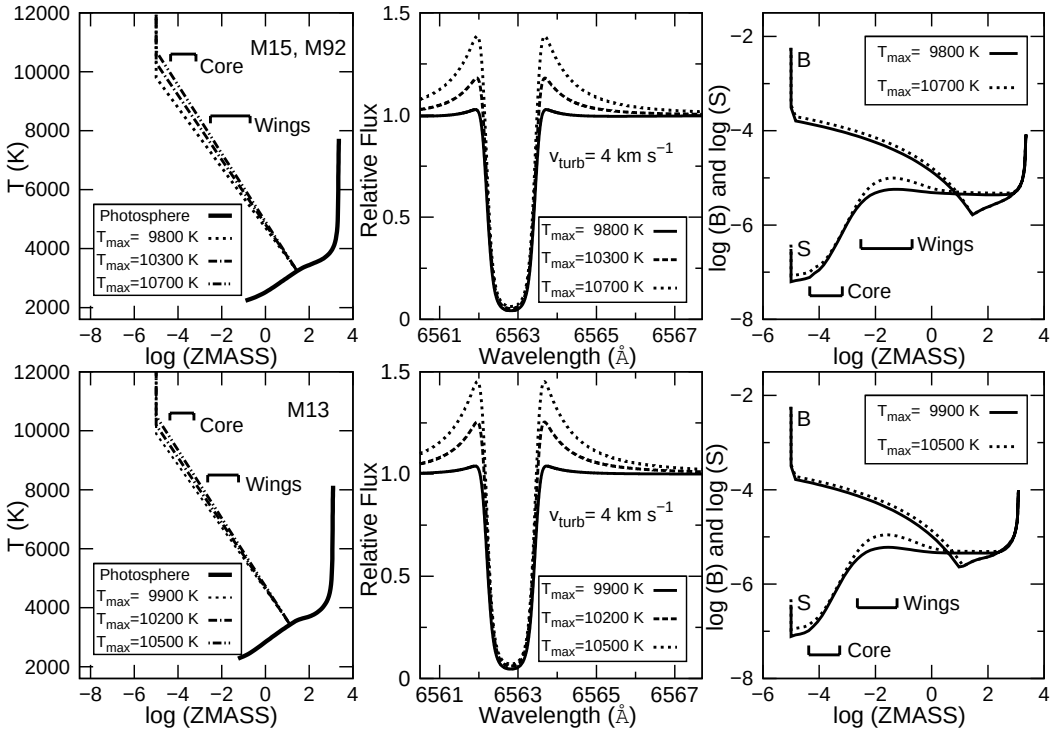

Figure 5.3: *Top left: The temperature distribution of the chromosphere as a function of mass column density for three of the input models for M15 and M92. The solid line is the Kurucz model without any chromosphere. In all cases the chromosphere extends to ZMASS=*1×10^{-5} *(g cm*$^{-2}$*), where the transition region starts.* T_{max} *is the maximum temperature of the chromosphere. The regions of formation for the H*α *wing and core are marked. Top middle: H*α *profiles for 3 models. Only a few hundred K differences in the maximum temperature result in large changes in the emission. The three static input models use 4 km s*$^{-1}$ *for the turbulent velocity, constant with depth. Top right: The Planck (B) and source (S) functions for two models as a function of mass column density. Lower three panels: The same results for the models of stars in M13.*

contribute to the photoionization of hydrogen. In every model I assumed a microturbulent velocity of 4 km s^{-1} in each point of the atmosphere.

Calculations were carried out in two phases for all models: in the first phase a plane-parallel approximation was used in order to calculate the scale of the atmosphere and the total H density from the initial and fixed ZMASS values, the Kurucz scale height, and total hydrogen density. A run was considered converged if the new height scale and total hydrogen density did not change by more than 1% as compared to the previous run. After this, the plane-parallel atmosphere was replaced with a spherical atmosphere with the same stratification, and this spherical model was used to calculate the emergent spectrum. To check the accuracy of our input approximations, I changed the input radius, gravity, and [Fe/H] each by a factor of 2 for one model. Changing the [Fe/H] does not affect the line profiles, but the radius and gravity do. A smaller radius (and larger gravity) leads to stronger emission. Although the line profile changes, the changes in radius and gravity do not affect the derived mass loss rates by more than our errors from the velocity-field

determination (see Section 5.2.3).

The emission wings of the Hα line can arise from an extended, static chromosphere if the temperature is high enough. The Hα line core forms between depths 16−21 (8000−9900 K), the wings from between depths 24−35 (5800−7800 K) in every model, depending on T_{max}. The strongest emission comes from the regions in the chromosphere where the electrons in the hydrogen are excited, but not ionized. In these places, the number density of hydrogen in the N=3 and N=2 states is the highest. The emission strength depends on T_{max}, because with higher temperature the N=3 and N=2 states are more populated. In deeper regions (depths $>$ 36, $<$ 5800 K) the gas is optically thick, in higher regions (depths $<$ 24, $>$ 8000 K) the hydrogen number density is too low to cause significant emission. At around 8000 K, the hydrogen becomes fully ionized and the scattering due to free electrons increases significantly, causing a deep absorption line.

5.2.3 Expanding Chromosphere

From Figure 5.3, one can see that emission wings arise in warm, static chromospheres. However, the static atmosphere cannot explain the asymmetry of the emission wings and the 'banana-shaped' bisector of the observed profiles (Dupree et al., 1984). Thus, flow velocities must be present in the atmosphere. Accordingly, the regions where the core and wings of the Hα line are formed were put in motion. I constructed velocity distributions in order to produce asymmetrical line profiles to match the observed line asymmetries. This velocity field is included when calculating the line source function. The line-forming regions were determined from the depths where the maximum contributions to the spectrum occur. The Hα line core forms between 8000−9900 K, the wings from between 5800−7800 K in the chromosphere in every model, depending on T_{max}. The rest of the atmosphere does not affect the line profile, thus we do not have information on the velocity field outside these regions. The velocity was changed usually between −14 and 20 km s^{-1}, where the negative number means an inward velocity and the positive number means an outward velocity relative to the photosphere.

In order to match the line profiles, three characteristics of Hα were considered: 1) the bisector velocity ($v_{\rm bis}$) and the position of the Hα core, 2) the width of the Hα absorption line, and 3) the ratio of of the strength of the blue and red emission wings (B/R). The velocities of $v_{\rm bis}$ are calculated in the following way (Mészáros et al., 2008): the absorption line is divided into about 20 sectors of equivalent depth; the top and the lower 3 sectors are selected and the wavelength average of the top and lower sectors is calculated, subtracted one from another and changed to a velocity scale.

The fitting was done by, first, taking a well converged spherical run in which the modeled emission matched the observation. The strength of the emission has an important effect on the calculated mass loss rate, because in our approximations it scales the

Table 5.2. Physical Parameters of Calculated Chromospheric Models

ID No.	Obs[a] Date	T_{max} [b] (K)	$v_{\rm bis,1}$ (km s^{-1})	v_{max} [c] (km s^{-1})	v_{esc} [d] (km s^{-1})	MLR ($M_\odot yr^{-1}$)
M13						
L72	2	10300	-5.0 ± 0.6	13.0	54.0	3.3e-09
	5	10100	-5.7 ± 0.8	9.0	54.0	2.3e-09
L96	2	9900	-6.1 ± 0.9	19.0	57.0	4.8e-09
L592	5	8000	-2.6 ± 0.3	8.5	69.0	2.6e-09
L954	2	10000	-1.8 ± 0.6	12.0	48.0	3.1e-09
L973	2	10300	-1.9 ± 0.4	6.5	46.0	1.6e-09
M15						
K87	8	8000	-3.9 ± 1.3	9.0	65.0	1.4e-09
K341	1	9900	-3.2 ± 0.6	12.0	51.0	2.2e-09
	6	10000	-6.9 ± 1.0	13.0	51.0	2.4e-09
	7	10300	-6.2 ± 0.6	13.0	51.0	2.4e-09
	8	10200	-6.3 ± 0.9	13.0	51.0	1.7e-09
K421	7	10250	-4.3 ± 0.7	10.0	66.0	1.9e-09
K479	8	10400	-0.7 ± 0.7	12.0	64.0	2.3e-09
K757	1	10200	-2.8 ± 0.5	3.0	50.0	5.7e-10
	6	10600	-8.9 ± 1.1	16.0	50.0	3.0e-09
K969	1	10500	-4.0 ± 0.6	6.0	57.0	1.1e-09
	8	10700	-1.7 ± 0.3	9.0	57.0	1.7e-09
M92						
VII-18	3	10150	-3.0 ± 1.0	15.0	49.0	2.0e-09
	4	10200	-2.8 ± 0.8	15.0	49.0	2.0e-09
X-49	3	9950	-6.9 ± 0.8	15.0	50.0	1.9e-09
XII-8	3	9900	-5.6 ± 0.8	11.0	57.0	2.0e-09
XII-34	3	8000	-2.3 ± 1.3	8.0	66.0	1.2e-09

[a]Observations: 1: 2005 May 22, 2: 2006 March 14, 3: 2006 May 7, 4: 2006 May 9, 5: 2006 May 10, 6: 2006 May 11, 7: 2006 October 4, 8: 2006 October 7.

[b]The maximum mass column density of all models is 1×10^{-5} (g cm^{-2}) in the chromosphere, the stellar radius for each model is R=70R$_\odot$.

[c]The maximum expansion velocity used in the models.

[d]Escape velocity calculated at the level with the highest expansion velocity assuming M=0.8M$_\odot$.

atmosphere. Higher $T_{\rm max}$ corresponds to a larger height scale (Figure 5.2, lower panels), and smaller hydrogen density, because the mass column density is the same in every model. Then, the previously measured bisector velocity of the Hα absorption line gave an estimate of the expanding velocity in the core. However, in almost every case this velocity did not yield the same bisector and position of the core in the calculated profile as in the observed one. Higher values of the velocities were required indicating that the measured Hα bisectors are a lower limit to the actual velocity fields present in the star. Nearly a factor of 2 higher velocities were necessary in the models in every case. The value of velocity in the region where the wings form influences the B/R ratio. In most cases, if B/R>1, then an inward velocity was needed; when B/R<1, an outflowing velocity was required. Our observations show that the Hα line cores are either at rest or moving outward from the star. Moreover, the line asymmetries can change from one observation to another, thus a complex time-dependent velocity field must be present in these chromospheres.

The microturbulent velocity was also changed from 4 km s^{-1} (used in the generic spherical calculations) in order to match the width along the Hα line with the observation. The assigned microturbulent velocity varied between 6 and 14 km s^{-1} in the region where the wings of the Hα line form, and 0 km s^{-1} where the core forms in order to better match the width of the core. After the calculation was completed, the model profile was compared with the observation by eye and further adjustments were made to the velocity field. This was continued until the modeled and observed line profiles matched each other as well as possible. The mass loss was then estimated with a simple formula based on mass outflow:

$$\dot{M}(M_{\odot}\ yr^{-1}) = 2.33 \times 10^{-26} \times m_H \times N_H \times 4\pi \times R^2 \times V_{exp} \tag{5.31}$$

where m_H(g) is the mass of the hydrogen atom, N_H(cm^{-3}) is the total hydrogen density, R(cm) is the distance from stellar center, and $V_{\rm exp}$(cm s^{-1}) is the velocity of the outermost layer. In our calculation the velocity, distance, and hydrogen density of the outermost layer forming the line core gave the mass loss rate for each star.

To obtain an estimate of the error of the mass loss rates, the expanding velocity in the wing and core forming regions was changed by ± 1 km s^{-1} in every depth. In both cases the mass loss changes by less than a factor of 2 and the line profile changes are not visible by eye. Changing every depth by ± 2 km s^{-1} usually gave a worse fit to the observation; thus I conclude that the error in the derived mass loss rates appears to be a factor of 2.

5.3 The Calculated Profiles

5.3.1 Spectra in General

The comparison of observed and calculated spectra is shown in Figures 5.4 to 5.4, and the derived mass loss rates are listed in Table 5.2. The spectra were computed at high resolution, and were convoluted with a Gaussian distribution corresponding to the spectral resolution of ∼34000. I aim to match several of the line parameters: the central core depth, the core velocity shift, the line width, the strength and the asymmetry of the emission wings. Changing the model usually produces changes in more than one line parameter, and so our final model, the 'best fit', is frequently a compromise solution. In some cases the continuum level of the observed spectrum was shifted to match the calculated one, and I were able to match the observed profiles fairly well.

The main difference between calculations and observations is that the computed Hα profiles are slightly broader and deeper in the core; similar systematic differences were found by Mauas et al. (2006). This suggests that in our models there is either slightly

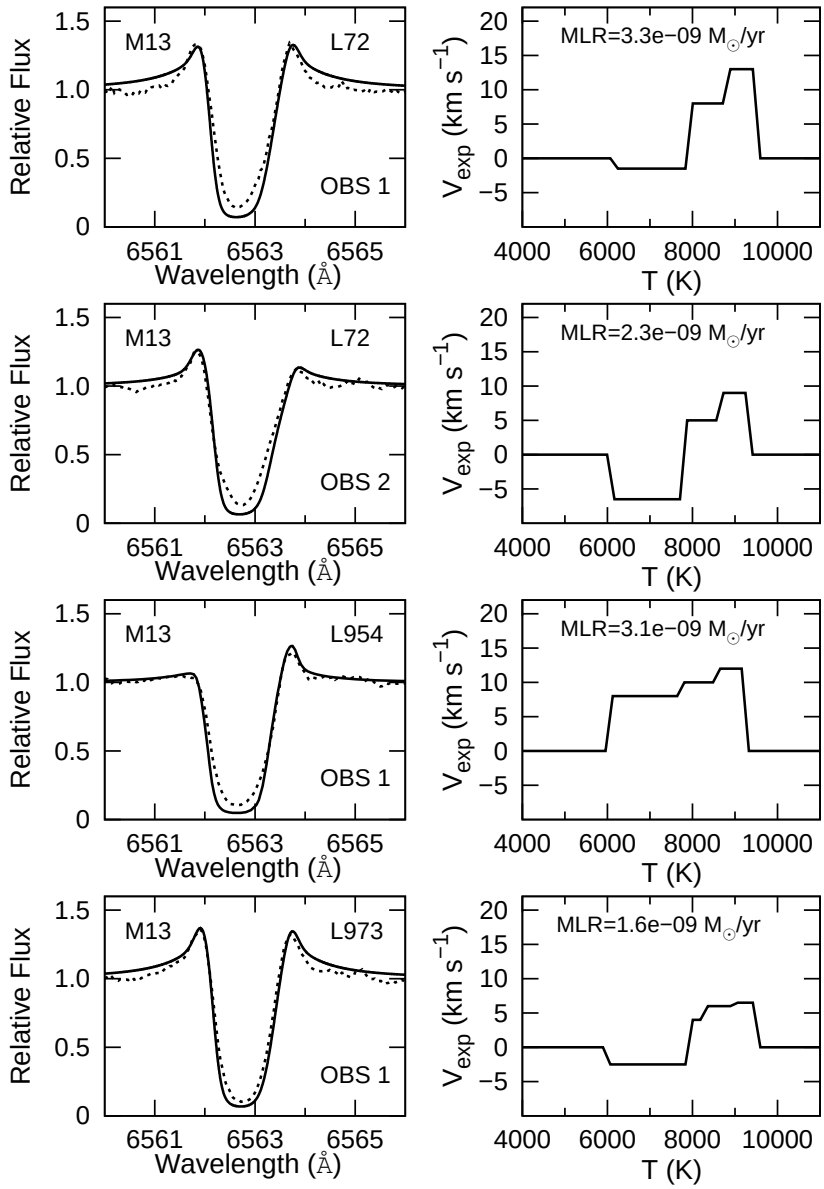

Figure 5.4: *Left panels: Calculated spectra compared to the observations of stars in M13. The solid line shows the calculated line profile; the broken line marks the observation. Right panels: The expansion velocity (v_{exp}) used to match the line profile as a function of temperature in the chromosphere. The height increases with increasing chromospheric temperature. The expansion velocity is positive for a outwardly moving flow and negative for a inwardly moving flow. The chromospheric temperature is increasing with increasing stellar radius. The derived mass loss rate is indicated for each model.*

more hydrogen in the atmosphere where the Hα core forms, or the chromosphere is hotter, thus increasing scattering from the core. The calculated atmospheres are homogeneous in every case, so that the difference in the core might also come from inhomogeneities in the atmosphere. This, however, does not affect the mass loss rate calculations by more than a factor of 2, because the wing asymmetry, bisector, and the position of the core are taken into account in fitting the observed profiles, and these characteristics are more

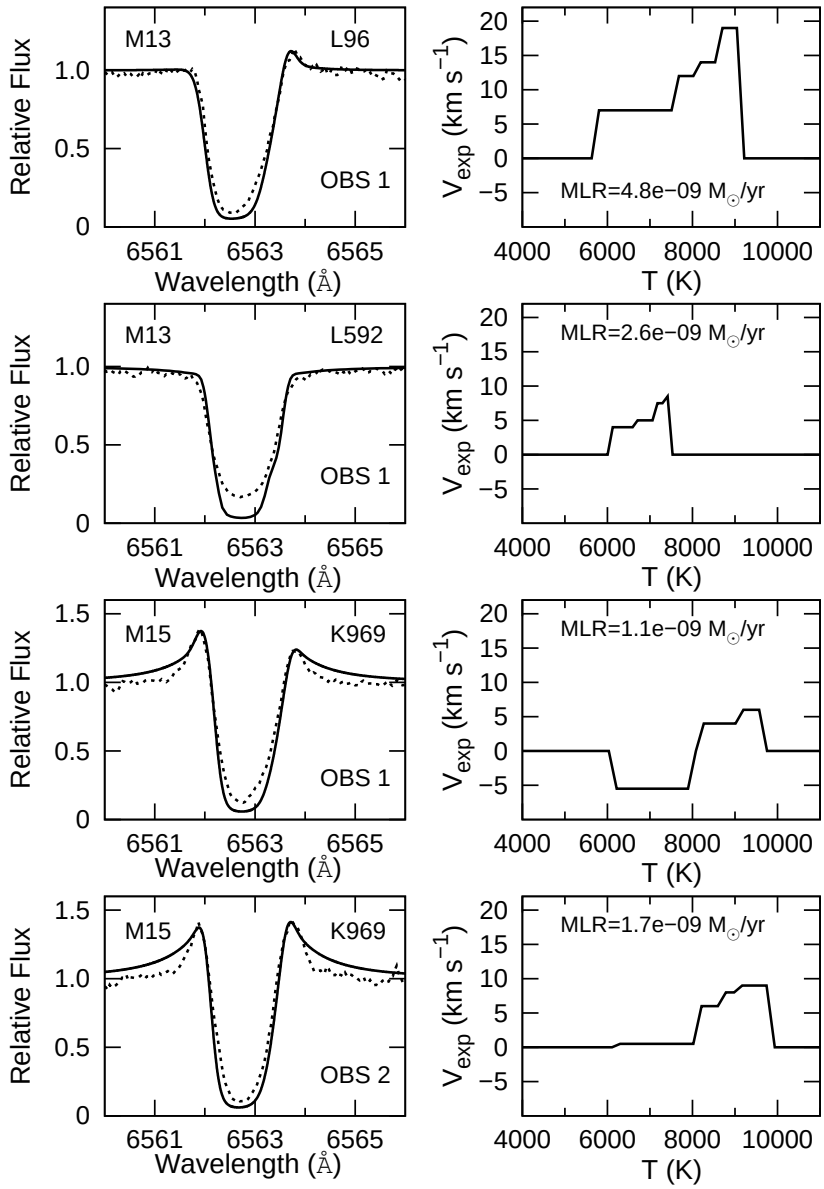

Figure 5.5: *Left panels: Calculated spectra compared to the observations. Right panels: The expansion velocity used to match the line profile as a function of temperature. For additional explanation see the caption of Figure 5.4.*

important in determining the calculated mass loss.

This homogeneous chromosphere approximation gives better results for brighter objects (for example L973 in M13, Figure 5.4) and only the faintest stars in each cluster (L592 in M13, K87 in M15 and XII-34 in M92) show major differences in the Hα core. In some cases an inward velocity had to be used where the emission wings formed in order to match the wing asymmetry, but in all cases an outward velocity was necessary to fit the core.

The stars, L592, K87, and XII-34 did not show any emission in Hα and have lower

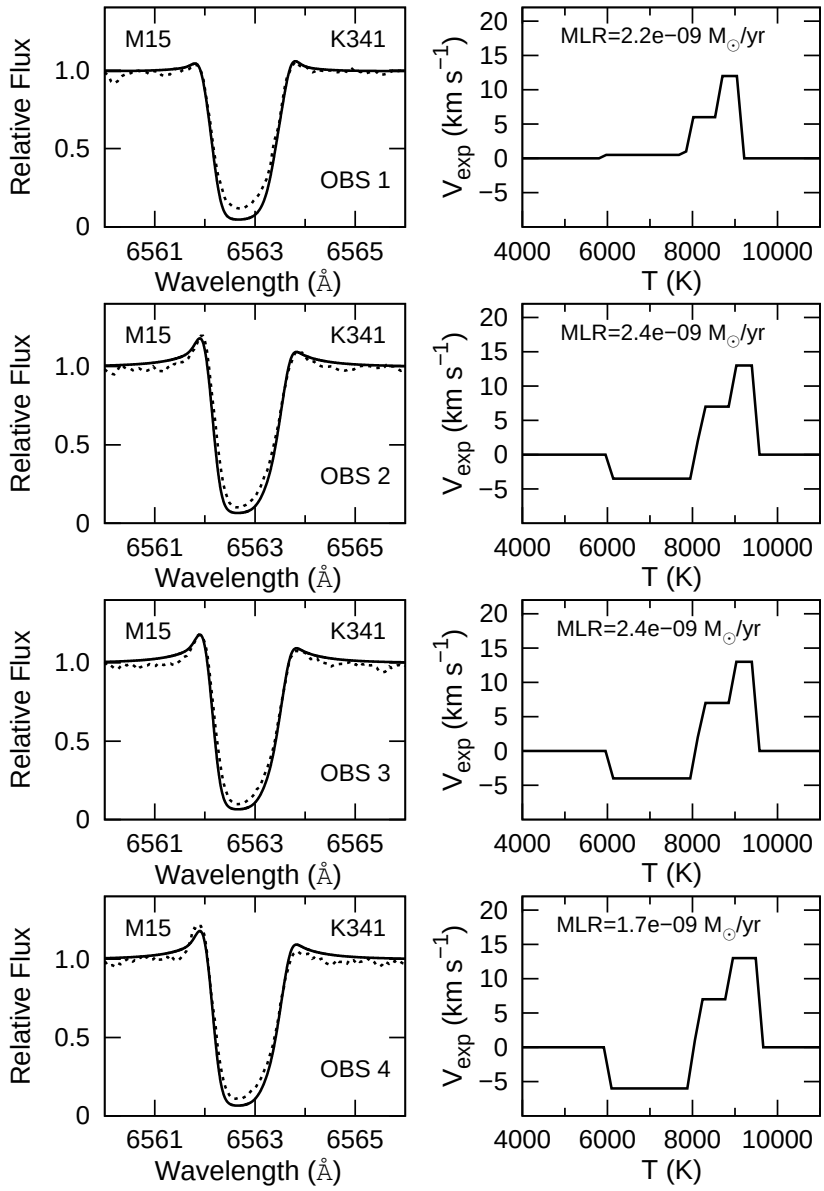

Figure 5.6: *Left panels: Calculated spectra compared to the observations. Right panels: Expansion velocity used to match the line profile as a function of the temperature of the chromosphere. For additional explanation see the caption of Figure 5.4.*

luminosities than other selected RGB stars with Hα emission. This makes it difficult to derive a mass loss rate for these stars. It was not possible to construct an accurate model when emission is not visible in the spectrum, because in our approach the emission wings were used to give the slope of the temperature versus mass column density in the static chromosphere. Thus only the bisector and the core of the Hα line affect the fit. The difference between the observed and calculated profile also derives from the fact that the radius and surface gravity for these stars are quite different (much smaller) than we assumed in each calculation. In order to check the accuracy of the derived mass loss

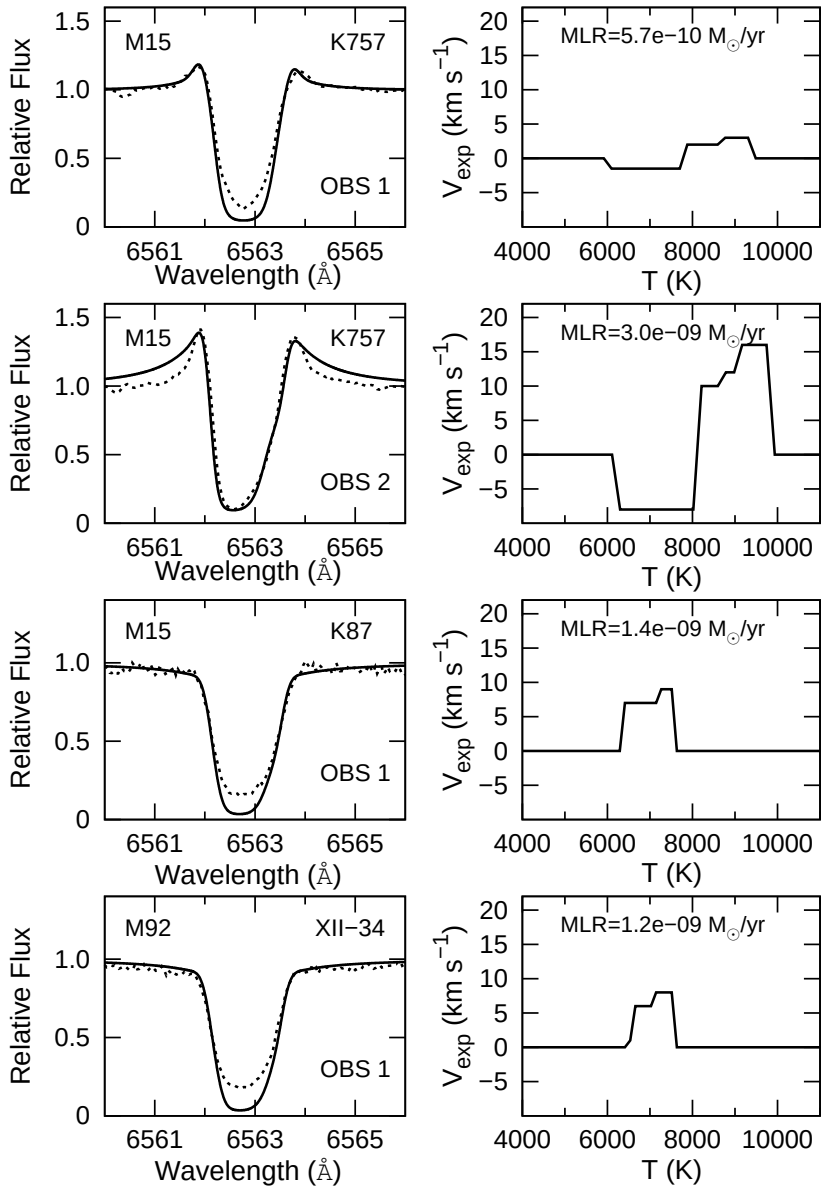

Figure 5.7: *Left panels: Calculated spectra compared to the observations. Note the difference in the profiles between the two observations of K757 and the nearly factor of 6 change in the mass loss rate. Right panels: Expansion velocity used to match the line profile as a function of the temperature. For additional explanation see the caption of Figure 5.4.*

rate, a static, spherical chromosphere was calculated using R=35$R_\odot$ and log g=1.25 −− parameters close to the values for these stars. The same velocity field was applied to this chromosphere as to the others. The mass loss rates do not differ from each other by more than a factor of 2, but the new profiles using the smaller radius do not match the observations very well. Thus, in the final interpretation here I use the model with R=70$R_\odot$.

The Hα core generally forms between T=8000 and 9900 K, which, in our models, is located between 1.4 and 2.0 R_* in the chromosphere. All of the observed Hα profiles

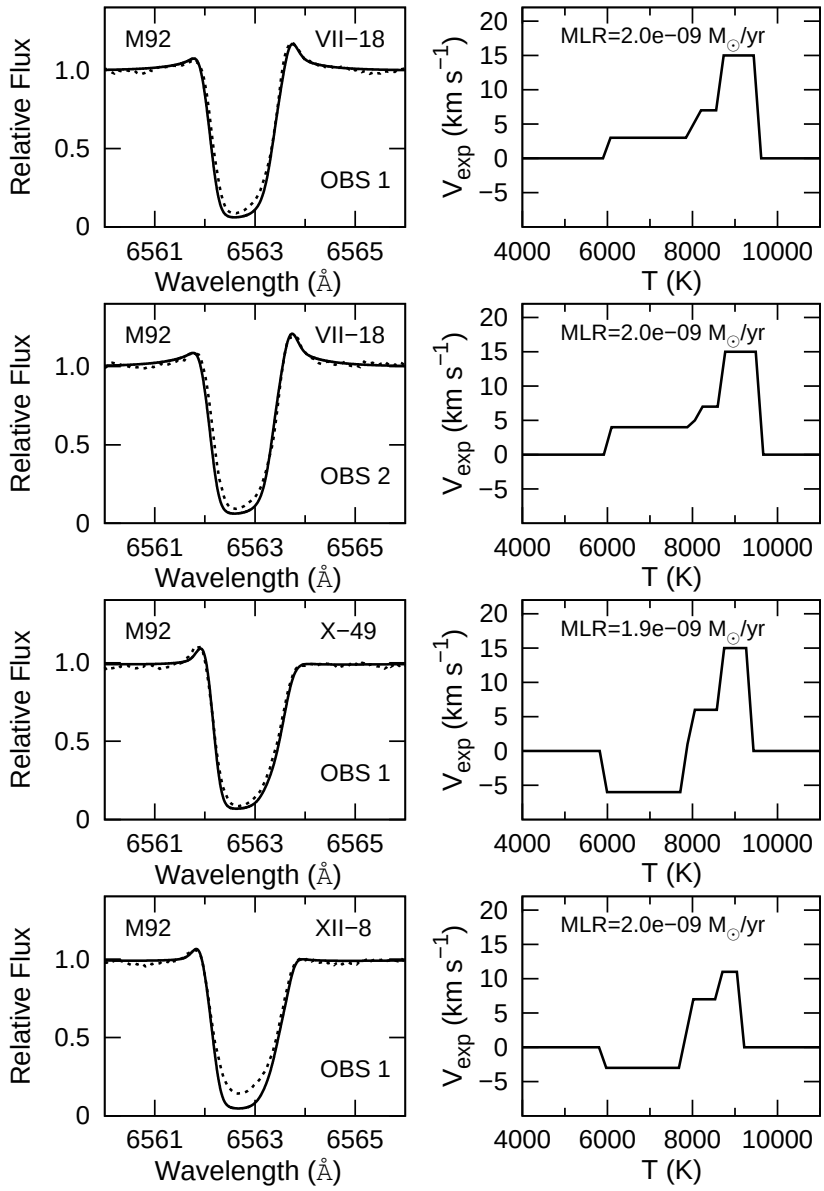

Figure 5.8: *Left panels: Calculated spectra compared to the observations. Right panels: Expansion velocity used to match the line profile as a function of the temperature. Additional explanation can be found in the caption of Figure 5.4.*

have a static or outflowing core. The semi-empirical models thus all require outflow at the top of the atmosphere in order to match the profiles. At the highest temperatures ($T > 10^4$ K), there is no contribution to the Hα profile, hence I have no information on any velocity field that might be present. Thus, I have reduced the velocity to zero. At lower levels in the atmosphere, below T$\sim$8000 K either inflow or outflow occurs. The direction of the velocity field in the model is determined by the asymmetry of the line wing emission. When B<R, an outflowing velocity is required; when B>R, an inflowing velocity is required.

Outflowing velocities used in the modeling vary between 3 and 19 km s^{-1}, which are much smaller than the escape velocity (50−70 km s^{-1}) from this part of the chromosphere (Table 5.2). In our spectra, the Hα core is either at zero velocity with respect to the star, or moving outwards. There are no signs of any inflow in the core itself. Therefore it appears reasonable to assume that the outward velocity continues to increase until the escape velocity is reached. While the material is not escaping from the chromosphere where the Hα core forms, analysis of Mg II lines and the He I λ10830 absorption line of RGB stars in NGC 6752, M13, and metal-poor field giants shows that velocities can reach up to 140 km s^{-1} (Dupree et al., 1992, 1994, 2007, 2009; Smith et al., 2004). These lines are formed higher in the atmosphere than Hα, which suggests that the mechanisms driving the stellar winds become stronger above the top of the chromosphere and escape of material is only possible at distances >2.0 R_*.

The derived mass loss rates can account for the theoretical mass loss of $\sim 0.2-0.4\ M_\odot$ (Fusi Pecci et al., 1993; Christy, 1966) required to explain the period-luminosity relation for RR Lyrae stars, the observed morphologies of the HB in globular clusters, and the maximum luminosity reached by AGB stars. Considering 50 Myr that these stars spend on the RGB, a star will lose about 0.2 $M_\odot$ before reaching the HB, if it has a average 3.0×10^{-9} $M_\odot$ yr^{-1} mass loss rate on the RGB, which is very similar values that I find from these semi-empirical models.

5.3.2 Changes in Time

One star in M13 (L72) and M92 (VII-18) and three stars in M15 (K341, K757, and K969) were observed more than once, which allows us to examine how the mass loss might change between observations. Separate semi-empirical atmospheric models were constructed to match each of the observed profiles. Of these 5 stars, three showed evidence of a difference in the mass loss rate, and two had nearly the same mass loss rate between observations. In the case of K341 (Figure 5.6) the mass loss rate changed only slightly with the respect to the observed spectrum, and these differences are smaller than the error of the mass loss determination. L72 showed less than a factor of 2 change in the mass loss rate over a month time span even though the observed spectra are quite different in the asymmetry of the emission wings (Figure 5.4). Although the atmospheric motions changed, this created only a slight difference in the mass loss rate. A much larger difference occurred in K757 (Figure 5.7), where the core asymmetry became prominent, and the derived mass loss rate increased from 5.7×10^{-10} $M_\odot$ yr^{-1} to 3.0×10^{-9} $M_\odot$ yr^{-1} – by almost a factor of 6. Nearly one and a half years separate these two observations. Such large changes were visible in AGB stars in M15 (Mészáros et al., 2008) near $\log(L/L_\odot) \sim 2.0-2.7$ in 1.5 years. This star, K757, is however on the RGB according to its position on the CMD (Figure 5.1) and was not identified as a dusty AGB star by Boyer et al.

(2006), which demonstrates that large changes in the mass loss rate can occur on the RGB as well.

Of these 5 stars, two showed evidence of pulsation in the spectra. The B/R ratio of emission in the spectra of K341 changed between observations. During the first observation (2005 May) the emission asymmetry signals inflow; in the following 3 observations (2006 May and October) the asymmetry suggests different values of outflow. Although in the case of the first observation the modeled velocity is slightly greater than zero, the emission ratio cannot be modeled with outflow velocities. The Hα core, however, shows an outflow in every observation. I take this as evidence of a pulsation present in the lower chromosphere. Our models show that the pulsation extends outwards into the chromosphere to around 1.4−1.5 R_*; at these levels and below, both inward and outward flows are possible, but the higher parts of the chromosphere (>1.5 R_*) do not participate in the pulsation. It is more likely that pulsation itself helps to drive the mass outflow. The only other star with varying inflow and outflow velocities where the emission forms is K969. The dust-free models of Struck et al. (2004) suggest that a stellar wind may be supported by shock waves which travel through the wind, possibly related to the pulsation in the lower levels of the atmosphere, similar to what is present here in the red giants.

5.3.3 Comparison with Other Models and Mass Loss Relations

The values of the mass loss rates that I find range from 0.6×10^{-9} to 5×10^{-9} ($M_\odot$ yr^{-1}). These values are in general agreement with other calculations for metal-deficient giant stars in the field or in the cluster NGC 2808. Mauas et al. (2006) modeled five very cool stars (T_{eff} <4015 K) and found differences in the mass loss rates amounting to a factor of 38 – with values ranging from 0.1×10^{-9} to 3.8×10^{-9} $M_\odot$ yr^{-1}. This may reflect the sort of episodic change that might lead to dust production. However, because the line cores of Hα in the models do not seem to well match the observed profiles, the derived mass loss rates could be affected. Their velocity profiles also differ from ours. In fact, inward velocities were not required to match the observed Hα emission line profiles, even if they signaled inflow. For line profiles with B>R, they introduced a decelerating velocity field with increasing radius in order to match the profiles. Thus, the zero point of the chromospheric velocity is different.

The literature contains various relationships to estimate the mass loss rates for luminous cool stars. The widely used 'Reimers law' based on dimensional arguments (Reimers, 1975, 1977), derives from a handful of Population I giant stars. This mass loss formula was later revisited by Catelan (2000) and suggested a stronger dependence on luminosity, radius and log g. The SC relationship (Schröder & Cuntz, 2005) is more detailed and includes gravity and effective temperature and assumes that the wind arises from an extended, highly turbulent chromosphere, possibly associated with Alfven waves. They did

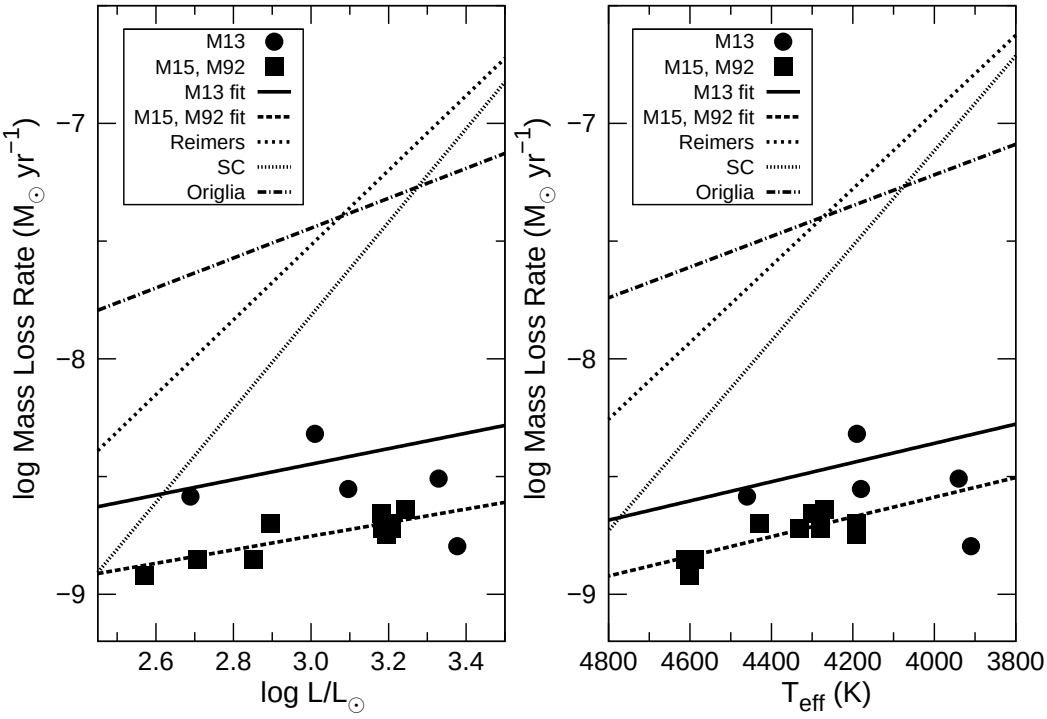

Figure 5.9: *Average mass loss rates calculated in this paper (solid circles and solid squares) as compared to relations proposed by Reimers (1975, 1977), Schröder & Cuntz (2005), denoted by SC, and Origlia et al. (2007). The C parameter introduced by Origlia et al. (2007) was set equal to 1. Mass loss rates for each of the target stars were calculated from the 3 relationships, and the curves shown were fit to the individual points. Our derived mass loss rates from the Hα line profiles are almost a factor of 10 smaller than from existing mass loss approximations. The fits to the mass loss rates for M13, M15, and M92 are shown as given in Section 5.3 of the text. The two coolest stars in M13 showed small outflow velocities and were not included in the fitting procedure.*

not consider extremely metal-deficient stars, such as those in M15, in their calibration. Origlia et al. (2007) presented an empirical (dusty) mass loss formula based the globular cluster 47 Tuc. Dusty RGB stars were identified from mid-IR photometry with *Spitzer*. Mass loss rates were calculated by modeling the emerging spectrum and dust emission with the DUSTY code (Ivezić et al., 1999; Elitzur & Ivezić, 2001). The dependence of the mass loss rate on luminosity is much shallower than suggested by the Reimers relationship.

These rates are shown in Figure 5.9 and listed in Table 5.3, where they differ from our model calculations by an order of magnitude at least. For the faintest stars, below log $(L/L_\odot) = 2.8$ the Schröder-Cuntz (SC) relation predicts the lowest values of the 3 approximations; at higher luminosities the difference between the SC relation and our model calculations increases, amounting to an order of magnitude at the highest luminosities. While the slope of the Origlia relationship with luminosity is similar to ours, the predicted values of the mass loss rate are larger by more than an order of magnitude. Their formulation included a scaling factor, C, which is the product of the gas-to-dust

Table 5.3. Mass Loss Rates (MLR) of Modeled Stars

ID No.	MLR Average ($M_{\odot}yr^{-1}$)	MLR Fit ($M_{\odot}yr^{-1}$)	MLR Reimers[a] ($M_{\odot}yr^{-1}$)	MLR SC[b] ($M_{\odot}yr^{-1}$)	MLR Origlia[c] ($M_{\odot}yr^{-1}$)
M13					
L72	2.8e-09	3.8e-09	4.1e-08	2.1e-08	4.0e-08
L96	4.8e-09	3.6e-09	3.0e-08	1.4e-08	3.6e-08
L592	2.6e-09	2.8e-09	8.8e-09	3.5e-09	2.2e-08
L954	3.1e-09	4.6e-09	1.0e-07	7.1e-08	5.8e-08
L973	1.6e-09	4.8e-09	1.2e-07	9.2e-08	6.2e-08
M15					
K87	1.4e-09	1.4e-09	8.8e-09	3.9e-09	2.2e-08
K341	2.2e-09	2.0e-09	5.2e-08	3.2e-08	4.5e-08
K421	1.9e-09	2.0e-09	5.6e-08	3.5e-08	4.6e-08
K479	2.3e-09	2.1e-09	6.5e-08	4.3e-08	4.9e-08
K757	1.8e-09	2.1e-09	5.7e-08	3.5e-08	4.6e-08
K969	1.4e-09	1.5e-09	1.5e-08	7.1e-09	2.7e-08
M92					
VII-18	2.0e-09	2.1e-09	9.0e-08	4.8e-08	5.5e-08
X-49	1.9e-09	2.0e-09	7.8e-08	4.2e-08	5.2e-08
XII-8	2.0e-09	1.7e-09	2.7e-08	1.0e-08	3.4e-08
XII-34	1.2e-09	1.4e-09	7.9e-09	2.5e-09	2.1e-08

[a]Rate from Reimers (1975, 1977).

[b]Rate from Schröder & Cuntz (2005).

[c]Rate from Origlia et al. (2007).

ratio, the expansion velocity, and the grain density. They set $C = 1$ for 47 Tuc. Our clusters are lower in metallicity, presumably increasing the gas:dust ratio and the expansion velocities are slightly higher than the 10 km s^{-1} taken by Origlia et al. (2007). Thus, for the same grain density, the discrepancy between the dust rates and the modeled Hα rates would increase.

The rates derived for dusty winds from mid-IR photometry are consistently higher than those indicated by the gas. If the dust is produced episodically (Mészáros et al., 2008; Origlia et al., 2007) at these high rates, it is puzzling that anomalously massive outflows have not been detected in the optical spectra. The IR observations led Origlia et al. (2007) to conclude that mass loss in 47 Tuc is ongoing in a fraction of the stars ranging from 16 to 32 percent on the RGB, whereas the Hα spectra and modeling of stars in M13, M15, and M92 shows that all of the stars have outflowing chromospheric material.

A least-squares fit to our mass loss rates as a function of luminosity, temperature and [Fe/H] yields the following form:

$$\dot{M}[M_{\odot}\ yr^{-1}] = 0.092 \times L^{0.16}[L_{\odot}] \times T_{\rm eff}^{-2.02} \times A^{0.37} \tag{5.32}$$

where $A = 10^{[Fe/H]}$. Here I have excluded the 2 most luminous stars of M13 from the fit, because I believe that Hα becomes less sensitive to the mass outflow at the low

temperatures of the metal-rich red giants. The values calculated from this relationship are given in Table 5.3 and shown in Figure 5.9.

5.4 *Spitzer* Stars

Boyer et al. (2006) have observed M15 with the *Spitzer* Space Telescope using the IRAC and MIPS instruments. They concluded that a significant amount of dust ($9 \pm 2 \times 10^{-4} M_{\odot}$) occurs near the center of the cluster and suggested that this dust comes from the mass-loss of the brightest giant stars. Twenty-three stars were identified as dusty IR sources and their IRAC colors indicate that these are AGB stars.

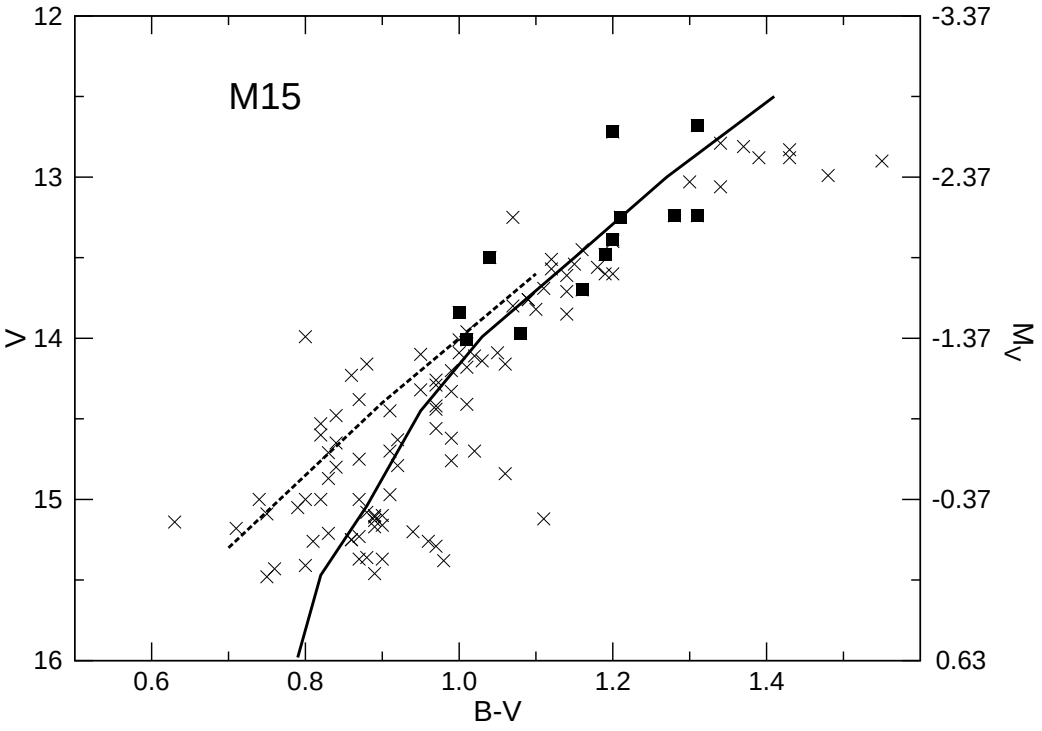

Figure 5.10: *Color-magnitude diagram for all stars observed in 2005 and 2006. The solid line shows the fiducial curve of the RGB and the dashed line shows the fiducial curve of the AGB for M15 taken from observations of Durrell & Harris (1993). Dusty giants identified with Spitzer Space Telescope (Boyer et al., 2006) and observed with Hectochelle, are denoted by squares. The redward "hook" seen among the brightest stars in M15 is not intrinsic to the stars but rather results from saturation of the photographic images (Sneden et al., 2000). Absolute magnitudes are obtained by assuming* $(m - M)_V = 15.37$ *(Harris, 1996).*

I observed 12 of these stars (Table 7.1) and could confirm their cluster membership with radial velocity measurements (Table 7.7) (Mészáros et al., 2008). I noted one source, designated by Boyer et al. (2006) as unidentified (SSTU J212953.33 +120910.7) is associated with K272 at the same coordinates. All of the observed *Spitzer* stars showed blue shifts in Hα . Six of them (K224, K421, K479, K672, K709 and GEB254) have strong Hα emission, but only one (K479) had outflow asymmetry in Hα (B<R). Other stars in the

Spitzer field (K144, K260, K393, K431, K447, K462, K702) were not identified as dusty stars, yet their Hα line emissions and blueshifts are similar to those stars identified by *Spitzer* observations as having an IR excess. Evidently not all stars produce dusty shells. The Hα emission profiles observed here do not seem to be related to a prior phase when the star produced material that cooled down to produce an IR excess.

All twelve *Spitzer* stars have the same colors and luminosities as other RGB stars on the CMD (Figure 5.10) and their bisector velocities also show similar values (Figure 3.13) as other RGB stars at the same luminosity. However the bisector velocity does not appear to correlate with any IRAC colors or magnitudes. The intensity ratio of short wavelength and long wavelength emission peaks (B/R) and the strength of the Hα emission wings are very similar to other stars in this color and luminosity region of the CMD. In this region, where the *Spitzer* sources are located, the differences between the AGB stars and RGB stars are hard to discern spectroscopically.

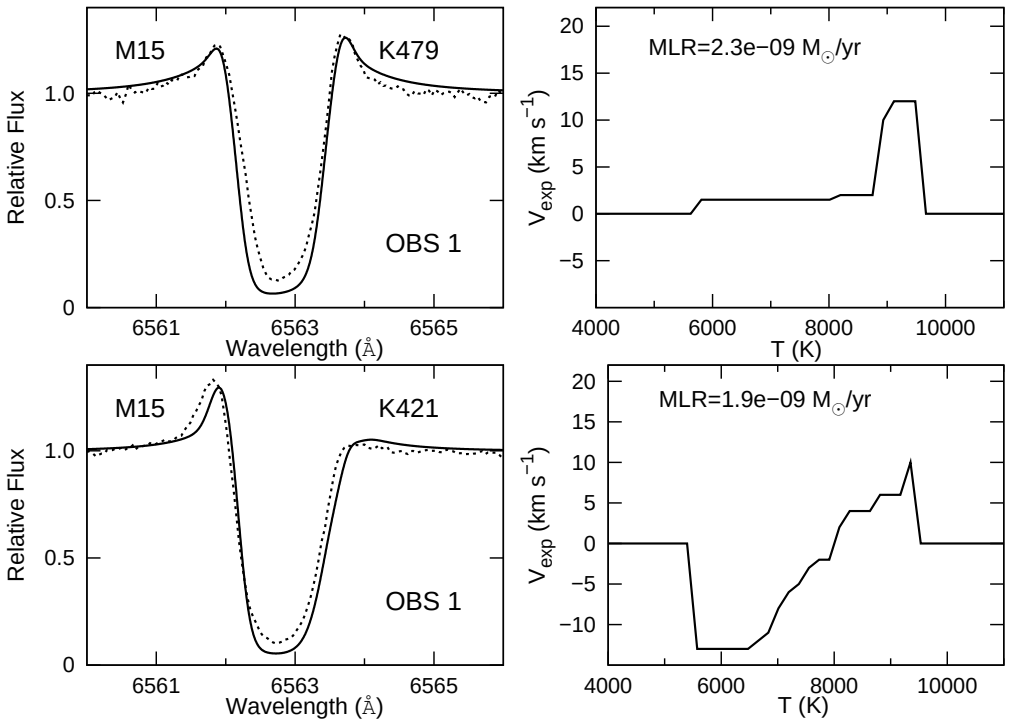

Figure 5.11: *Left panels: Calculated spectra of giant stars identified as having circumstellar material from Spitzer observations (Boyer et al., 2006) compared to the observations. Right panels: The expansion velocity used to match the line profile as a function of temperature. Additional explanation can be found in the caption to Figure 5.4.*

Spitzer showed (Boyer et al., 2006) that only some stars in this region of the CMD have a mid−IR excess. Assuming that the *Spitzer* sources must have had strong stellar winds to produce dust and the current Hα emission profiles are not related to the episode of dust production, one can conclude that the mass loss is not continuous. Origlia et al. (2002) used ISOCAM images to study red giants in globular clusters but the large pixel

size of ISOCAM made it difficult to identify stellar sources. Frequently, several stars were candidates for each mid-IR source in a 15 arcsec square area, and the brightest one was selected. They concluded that strong mass loss occurred only among RGB stars located at the red giant tip [log $(L/L_{\odot})$ >= 3]. Not all of the luminous stars identified in this way had in IR excess indicating dust, suggesting that the mass loss was episodic. The results reported here have no ambiguity in identification, and demonstrate the presence of episodic mass loss over a much greater extent in luminosity. These stars must have passed through several active phases with very strong stellar winds during their lifetimes on the AGB.

Models of two stars in M15, K421 and K479, previously identified as dusty AGB stars by Boyer et al. (2006) were also calculated (Figure 5.11) (Mészáros et al., 2009b). These stars are similar in luminosity, effective temperature, and bisector velocity to other RGB stars included. For these two stars I find no difference in mass loss rate from other red giants. Mass loss rates suggested by the IR excess exceed by more than an order of magnitude the rates inferred from Hα . If the mass loss must be high in order to produce dust, I conclude that the M15 giants are not currently undergoing an episode of dust-production. The dust observed in the dusty RGB stars most likely left the star decades earlier so one does not necessarily expect a correlation between time varying chromospheric phenomena and dusty envelopes.

Chapter 6

Summary

Mass loss plays an important role in stellar evolution. The amount of mass loss strongly depends on the stage of stellar evolution. Red giant stars have significantly higher mass loss rates than stars on the main sequence. Many red giant stars can be found in globular clusters, which appear in the halo of the Milky Way. This helps the investigation of mass loss, because nearly hundreds of red giant stars at the same distance can be observed at the same time. Here, I give an overview of my high resolution spectroscopic observations and semi-empirical models to calculate mass loss rates of red giants stars.

In the first part of this thesis, I briefly explained the stellar evolution and mass loss processes. In the second part I showed my observations with Hectochelle on the Multi Mirror Telescope (MMT), and discussed the results from the statistical investigation of line profiles. In the third part, I gave an overview of how I determined the mass loss rates from detailed line profile modeling.

Observations

Observations of Hα in a total of 297 stars on the red giant branch (RGB) and asymptotic giant branch (AGB) in M13, M15, and M92 were obtained in 2005 May, 2006 May, and 2006 October with the Hectochelle on the MMT (Mészáros et al., 2008, 2009a) with a spectral resolution of about 34,000. Only targets brighter than 15.5 magnitude were selected. Three order separating filters were applied: OB25 (Hα, region used for analysis $\lambda\lambda$ 6475 − 6630), Ca41 (Ca II K, $\lambda\lambda$ 3910 − 3990), and RV31 ($\lambda\lambda$ 5150 − 5300). OB25 and Ca41 filters gave 155 Å centered on the principal spectral features in Hα and 80 Å in Ca II H&K. The basic image reduction were done with the IRAF software package.

Radial Velocity Measurements

To measure accurate radial velocities I chose the cross-correlation method. For stars in M15, the Hα spectra of the targets were cross-correlated against several hundred spectra calculated with the ATLAS code, covering temperatures between 3500 and 7000 K and metallicities between [Fe/H]=−2.5 and +0.5. The region selected for the cross-correlation spanned 6480 Å to 6545 Å purposely omitting the Hα line. For stars in M13 and M92, the spectral region on the RV31 filter between 5150 Å and 5300 Å was chosen (besides the Hα filter), because it contains several hundred narrow photospheric absorption lines, thus the cross-correlation function is narrower than from the Hα region.

Alltogether 6 stars in M15 were observed at least twice and showed velocity changes larger than 2 km s^{-1}, which could indicate these stars are binaries. In M13 and M92, only 2 stars in each showed radial velocity changes. One of them, L72 in M13, is a well-known pulsator, which could acount for the velocity variaton.

Line Statistics

Differences found in the profiles of the Hα line give insight into the atmospheric structure and dynamics. Stars which are physically larger show more emission.

In M15, spectra of 29 stars with Hα emission were obtained in both 2005 and 2006 out of 110 red giants. All but two of these stars showed significant changes in the line emission which either appeared, or vanished, or changed asymmetry. I observed a total of 123 different red giant stars in M13 and found 19 with Hα emission. In M92, I found 9 stars with Hα emission out of 64 objects. For these two clusters, the configurations were chosen to eliminate stars already observed in order to achieve full coverage of the potential targets. The number of stars observed twice for M13 and M92 was very small, so comparison was possible for only two of them in M13 and three in M92. The emission of these stars also changed between observations.

Hectochelle spectra of M13, M15, and M92 show Hα emission to occur on the red giant branch in stars with $T_{eff} < 4500$ K and $\log(L/L_{\odot}) > 2.75$. AGB stars exhibit Hα emission to lower luminosities. Ca II K emission extends to lower luminosities than Hα both on the RGB and AGB. The asymmetry in the Ca II K core in M15, where measurable, may differ from the asymmetry measured in the Hα wings perhaps due to time variability or different line-forming regions.

Considering 3 clusters, spanning [Fe/H]=−1.54 (M13), to [Fe/H]=−2.3 (M15, M92), I find no systematic dependence of the presence of Hα or Ca II K emission from red giants on cluster metallicity. Stars in M15 have Hα emission wings that vary in time so that the magnitude of the faintest giant showing emission changes among the different dates of observation.

The Bisector Velocity

If movement is present in the atmosphere, then the absorption lines become asymmetric due to the Doppler-effect. If this movement in inward, the core of the absorption line will be redshifted, if it is outward, it will be blueshifted. By measuring this shift, I could identify movement in the chromosphere.

Asymmetric Hα cores show that chromospheric material is flowing out from stars brighter than log $(L/L_{\odot}) \sim 2.5$ and the speed of the outflow increases with increasing luminosity. The Ca II K_3 absorption features exhibit higher velocities than Hα suggesting accelerating outflows in the chromospheres. This outflow may represent the onset of mass loss, and the luminosity at which the outflow begins is similar for all metallicities. The sensitivity of Hα to mass motions decreases for $T_{eff} < 4000$ K causing the coolest giants in M13 to exhibit little or no outflow in this line.

However, AGB stars near log $(L/L_{\odot}) \sim 2.0 - 2.7$ have bisector velocities (10−15 km s^{-1}) comparable in value to those at the tip of the RGB and also exhibit larger changes in velocity between observation than the RGB stars (6−8 km s^{-1}). I take this as evidence of more substantial and episodic mass outflow on the AGB. Faster outflows are found in the metal−poor M15 and M92 than the metal−rich M13 objects. While outflow velocities of RGB stars do not depend on cluster metallicity, AGB stars show faster outflows in M15 and M92, than AGB stars in the more metal rich cluster M13. I find no differences in chromospheric signatures in the profiles or the presence of Hα and Ca II that can resolve the 'second-parameter' problem for the paired clusters, M15 and M92 (Mészáros et al., 2009a). Also, bisectors velocities are very similar in both clusters.

Twelve stars identified in Spitzer observations as dusty IR sources and AGB stars (Boyer et al., 2006) have radial velocities consistent with cluster membership. The similarities in Hα line profile characteristics between the *Spitzer* sources and other red giants in M15 suggests the IR emission attributed to circumstellar dust must be produced by an episodic process (Mészáros et al., 2008).

Models for the Hα Line

For the emission line calculations, I changed the parameters at the outer depths of the atmosphere to represent a chromosphere with the temperature increasing linearly with decreasing mass column density (Mészáros et al., 2009b). For every temperature−mass column density distribution, I solved the non-LTE radiative transfer and the statistical and hydrostatic equilibrium equations, using the program PANDORA (Avrett & Loeser, 2003). I computed the non-LTE populations of a 15−level hydrogen atom to get the Hα line. Calculations were carried out in two phases for all models: in the first phase a plane-parallel approximation was used in order to calculate the scale of the atmosphere

and the total hydrogen density. After this, the plane-parallel atmosphere was replaced with a spherical atmosphere with the same stratification, and this spherical model was used to calculate the emergent spectrum. Then, the regions where the core and wings of the Hα line are formed were put in motion. I constructed velocity distributions in order to produce asymmetrical line profiles to match the observed line asymmetries. This velocity field is included when calculating the line source function.

An expanding velocity at the top of the atmosphere was required for every star in order to match the Hα core. The largest outflowing velocity reached 19 km s^{-1}, usually larger by factors up to 10 than indicated by the bisector velocity. In the region where the Hα emission is formed, the velocities can change direction, indicating the presence of pulsation.

Mass Loss rates

Chromospheric modeling of the Hα line in several clusters demonstrates that the mass loss rate increases with increasing luminosity and decreasing effective temperature of stars on the red giant branch. All stars modeled down to 2 magnitudes below the RGB tip show outflowing material suggesting that mass loss is a continuous process. The more metal-rich stars have a higher mass loss rate than the metal-poor stars. We offer a new relationship for mass loss rates in Pop II stars based on these models.

The calculated mass loss rates from the Hα profile give values that are an order of magnitude less than those estimated from the Reimers (1975, 1977), SC (Schröder & Cuntz, 2005), and Origlia et al. (2007) relationships. Differences are larger at higher luminosities. The Hα mass loss rates and the Origlia relationship give a very similar shallow dependence on luminosity. At the top of the RGB, for stars brighter than log $(L/L_{\odot}) = 3.3$, the Hα line may not be adequately sensitive to the mass loss rate; the models suggest lower mass loss rates for these objects.

K757 (M15) shows a factor of 6 mass loss−rate change in a time span of 18 months (from 5.7×10^{-10} M$_{\odot}$ yr^{-1} to 3.0×10^{-9} M$_{\odot}$ yr^{-1}). A smaller change occurred in two other stars, K341 (M15) and L72 (M13), where the mass loss difference was nearly a factor of two. This shows that large changes in the stellar wind can occur in only one and a half years.

Considering 50 Myr that these stars spend on the RGB, with 3.0×10^{-9} M$_{\odot}$ yr^{-1} mass loss rate, a star will lose about 0.2 $M_{\odot}$ before reaching the HB. This is in good agreement of stellar evolution theories.

Two stars previously identified as dusty red giant stars in M15 show no difference in mass loss rate from other red giants. If high rates of mass loss are needed in order to produce dust, we conclude that the M15 giants are not currently undergoing an episode of dust-production.

Összefoglaló

A csillagszél általi tömegvesztés tanulmányozása kulcsfontosságú a csillagfejlődés folyamatának megértéséhez. A tömegvesztés mértéke a csillag fejlődési állapotától függ, és a vörös óriáscsillagok esetében több nagyságrenddel meghaladja a fősorozati csillagoknál mért értéket. Vörös óriáscsillagok nagy számban találhatók a Tejútrendszer halójában elhelyezkedő gömbhalmazokban, mely lehetővé teszi ezen csillagok egyidejű statisztikai vizsgálatát, és elősegíti a tömegvesztés mechanizmusának és mennyiségének jobb megértését. Munkám a tömegvesztés empirikus tanulmányozására irányult, ennek érdekében nagyfelbontású optikai spektroszkópiai méréseket végeztem, melyeket elméleti modellekkel értelmeztem.

Dolgozatom első harmadában ismertettem a csillagfejlődés és tömegvesztés elméleti hátterét, majd bemutattam megfigyeléseimet. A második harmadában részletesen elemeztem a megfigyelésekből származó eredményeket, míg az utolsó részben ismertettem a Hα vonalból meghatározott tömegvesztési ráták mögötti elméleti számításaimat.

Megfigyelések

Összesen 297, vörös óriáságon (RGB) és az asszimptotikus ágon elhelyezkedő csillagról készítettem nagy felbontású spektrumokat az arizonai MMT távcsőre szerelt Hectochelle nevű multiobjektum spektrográffal (Mészáros et al., 2008, 2009a). Az észlelések 2005 és 2006 között három alkalommal történtek az M13, M15 s M92 jelű gömbhalmazokról a Hα-ra centrált OB25-ös, a Ca II H&K-ra centrált Ca41-es, és az RV31-es szűrővel. A Hectochelle felbontása közel 34000, mely lehetővé tette a vonalalak részletes tanulmányozását. A spektrumok redukálása az IRAF programcsomaggal történt.

Radiális sebesség mérés

Radiális sebességek méréséhez a keresztkorrelációs módszert használtam. Az M15 jelű halmazban levő csillagok spektrumát összesen 2280, az ATLAS kóddal generált model spektrumokkal korreláltattam. A model spektrumok effektív hőmérséklete 3500 és 7000 K kózótt egyenletesen elosztva változott, míg a fémtartalom [Fe/H]=-2.5 es $+0.5$ között mozgott. A Hα szűrőben a korrelációhoz választott hullámhossz tartomány 6480 Å és 6545 Å közé lett megválasztva, tehát a Hα vonal a keresztkorreláción kívül esett. Az M13 and M92 jelű halmazokban levő csillagok esetében az RV31 szűrőben észlelt spektrumokat korreláltattam a modelekkel. Ebben a hullámhossz tartományban több száz jól elkülönült és vékony abszorpciós vonal található, ezáltal a kereszt korrelációs függvény csúcsa sokkal keskenyebb és pontosabb sebességeket ad, mint a Hα szűrő esetében.

Egy csillag radiális sebességének változása általában kettősségre, vagy pulzációra utal. Összesen 6 csillag mutatott 2 km s^{-1}-nál nagyobb radiális sebesség változást az M15 halmazban, több észlelés alkalmával. Mind az M13-ban es M92-ben 2−2 csillag radiális sebessége változott az észlelések között, ezek közül az egyik, L72, egy jól ismert pulzáló változócsillag.

A vonalalak tanulmányozása

Emissziós vonalak jelenléte egy aktív, nagy kiterjedésű és forró atmoszférára utal (mely függ a csillag méretétől), ezért a Hα és Ca II H&K vonalakon emissziót kerestem.

Az M15-ben észlelt 110 vörös óriáscsillagból 29 mutatott Hα emissziót. Az óriáscsillagok többszörös megfigyelése során jelentős változásokat észleltem a Hα vonal alakjában (mindössze kettő csillag kivételével), mely rövid időtartamú kromoszférikus változásokra utal. Emiatt még a leghalványabb csillagok által mutatott emisszió is változik. Az emisszió változása valószínűleg kapcsolatban áll a csillagok pulzációjával.

Összesen 123 csillagok észleltem az M13-as gömbhalmazban, melyek közül 19 mutatott Hα emissziót. Az M92-ben 64 csillag közül összesen 9 esetében figyeltem meg az emisszió jelenlétét. A többszörösen észlelt csillagok száma ezen két halmaz esetében nagyon alacsony volt (2 az M13-ban es 3 az M92-ben), de az emissziók erőssége itt is változott.

A vörös óriás ágon lévő csillagok esetben Hα emisszió csak $T_{\rm eff} < 4500$ K és $\log(L/L_\odot) > 2.75$ tartományokban jelenik meg halmaztól függetlenül, mely arra utal, hogy az emisszió mértéke kevésbé függ a csillagok fémtartalmától.

A Ca II emisszió erőssége szintén független az effektív hőmérséklettől, luminozitástól és a halmaz fémességtartalmától. Néhány csillag esetében az M15-ben, a Ca II emisszió ülönböző irányú mozgásokat mutatott az atmoszférában, mint a Hα vonal, mely rövid időtartamú változásokra, vagy bonyolult struktúrájú kromoszférára utal.

A biszektor sebesség

Ha az atmoszférában mozgás jelentkezik, akkor a Doppler-effektus következtében asszimmetrikus abszorpciós vonalprofil jön létre, melynek magja kiáramlás esetén a rövid hullámhosszak felé tolódik el. Ezen eltolódás mérésével a kromoszférában lévő mozgásokra lehet következtetni.

A Hα abszorpciós vonal biszektorából számolt sebesség azt mutatja, hogy csak azon csillagok mutatnak kiáramlást, melyek luminozitása nagyobb, mint $\log(L/L_\odot) > 2.5$, és ezen kiáramlási sebesség növekszik a luminozitással. A Ca II K_3 vonal segítségével mért kiáramlási sebesség azonos luminozitásnál általában nagyobb, mint a Hα-ban mért sebesség, mely egy az atmoszférában kifelé gyorsuló sebességmezőre utal. A legalacsonyabb $T_{\rm eff}$-el rendelkező csillagok az M13-as halmazban azonban csökkenő kiáramlási

sebességet mutatnak, ez egy jobban kiterjedt és ezért megváltozott struktúrájú légkörre utal, melyben a Hα vonal az atmoszféra kevésbé mozgó régiójában keletkezik.

Az aszimptotikus óriás ágon (AGB) lévő csillagok általában nagyobb kiáramlási sebességet mutatnak (10-15 km s^{-1}), mint az azonos látszó fényességű, de a normál vörös óriás ágon (RGB) fekvő társaik (6-8 km s^{-1}). Amíg az RGB-n mért kiáramlási sebességek nem függenek a halmaz fémtartalmától, az M15 és M92-es halmazokban lévő AGB csillagok nagyobb kiáramlási sebességet mutatnak, mint az azonos fejlődési állapotban lévő társaik az M13-ban. A két fémszegény halmazban (M15 és M92) található csillagok Hα vonalalakjai meglepően hasonlítanak egymásra, és nem utalnak különböző erősségű anyagkiáramlásra, ami azt jelzi, hogy a tömegvesztés nem magyarázza a második paraméter problémát e két halmaz esetében (Mészáros et al., 2009a).

A Spitzer űrtávcsővel 2006-ban felfedezett, porburokkal rendelkező AGB és RGB csillagok radiális sebességének segítségével sikerült a halmaztagságot megerősíteni. Ezen csillagok Hα vonalalakja nem különbözik más, hasonló luminozitású és effetkív hőmérsékletű, de porburokkal nem rendelkező csillagok vonalakjától. Ebből következik, hogy ez a tömegkiáramlás, mely felelős az infravörös tartományban sugárzó porburokért, valószínűleg epizodikus (Mészáros et al., 2008).

A Hα vonal modellezése

A tömegkiáramlás mértékének meghatározása céljából elméleti kromoszférikus modellekből rekonstruáltam a Hα vonalat a három halmazból választott néhány RGB csillagra (Mészáros et al., 2009b). Az alap modellekben a kromoszférában csökkenő oszlopsűrűség függvényében lineárisan növekvő hőmérséklettel számoltam. Ezen elméleti számításokat a PANDORA nevű programmal végeztem (Avrett & Loeser, 2003). A modellezés során különböző méretű és hőmérsékletű kromoszférában számoltam egy 15 energia szinttel rendelkező hidrogén atomban keletkező Hα vonalat. A számolás két lépésben történt: első lépésben egy plán-parallel atmoszférát hoztam létre, melyben az oszlopsűrűség- és hőmérsékletből megkaptam a skálamagasságot és a teljes hidrogén sűrűséget a kromoszférában. Ezután a plan-parallel modelt lecseréltem egy szférikus modelre, mely a végső spektrumot eredményezte.

A modellezés során az atmoszférában a termodinamikai egyensúlyt elhagytam, mely egy sokkal pontosabb kozelítést ad a kromoszférában végbemenő fizikai folyamatok leírására. Asszimmetrikus vonalprofilok létrehozása érdekében az emisszió és az abszorpció keletkezésének helyén az atmoszférához egy sebességmezőt rendeltem hozzá.

A számolt spektrumokat összehasonlítottam a megfigyelésekkel, melyek csak akkor mutattak jó egyezést, ha a felső kromoszférában egy kifelé gyorsuló sebességmező volt jelen. A tömegkiáramlási ráta ennek a sebességmezönek a segítségével lett meghatározva. Az így meghatározott tömegvesztés néhányszor 10^{-9} $M_\odot$ $év^{-1}$, mely egy nagyságrenddel

alacsonyabb a Reimers-törvény által jósoltnál.

A tömegvesztés mértéke

A tömegvesztés mértéke enyhén növekszik a luminozitással, csökken az effektív hőmérséklettel, és függ a csillagok átlagos fémtartalmától. Az RGB teteje alatt 2 magnitúdóval is megfigyelhető a tömegvesztés, mely arra utal, hogy a csillagszél az RGB-n való fejlődés során folyamatosan történik. A fémgazdagabb M13-as gömbhalmazban lévő csillagok átlagosan egy kettes faktorral nagyobb tömegvesztési rátával rendelkeznek, mint a fémszegényebb csillagok az M15-ben és az M92-ben.

A számolt tömegvesztési ráták nagyjából egy nagyságrenddel kisebbek, mint amit a Reimers (1975, 1977), SC (Schröder & Cuntz, 2005), és az Origlia et al. (2007) összefüggések jósolnak. Fényesebb csillagok esetében a különbség nagyobb. Az Origlia tömegvesztési ráta hasonlóan függ a luminozitástól, mint az általam számolt értékek. A legfényesebb csillagok az RGB tetején ($\log(L/L_{\odot}) > 3.3$) kisebb tömegvesztést mutatnak, mely arra utal, hogy a Hα vonal már nem érzékeny a csillagszélre ilyen nagy luminozitásoknál.

Az M15-beli K757-es jelű csillag másfél év alatti többszörös észlelése során a tömegvesztési rátában hatszoros különbség mutatkozott, míg más csillagoknál ennél sokkal kisebb (nagyjából kétszeres) változás történt. Ez arra utal, hogy a tömegvesztés jelentős változásokon megy végbe viszonylag rövid, éves időskálán (Mészáros et al., 2009b).

A számolt tömegvesztési értékek átlaga jó egyezésben van a csillagfejlődési elméletekkel, melyek $\sim 0.2\ M_{\odot}$ tömegvesztést jósolnak az RGB-n. Az általam kapott átlagos csillagszél erőssége $3.0{\times}10^{-9}$ $M_{\odot}$ év^{-1}, melyből következik, hogy egy csillag az RGB-n töltött idő alatt (kb. 50 millió év) $\sim 0.2\ M_{\odot}$ tömeget veszít.

A Spitzer űrtávcsővel 2006-ban felfedezett, porburokkal rendelkező AGB csillagok közül kettő Hα vonalának modellezését is elvégeztem. Az így kapott tömegvesztési értékek nem mutatnak különbséget más hasonló fényességű vörös óriás csillagétól. Ez szintén arra utal, hogy a porburkot létrehozó csillagszél epizódikus és valószínűleg az észlelések idején porképződés nem történik.

Acknowledgement

First, I would like to thank to my supervisors whitout whom this thesis could have not been written:

Dr. Andrea K. Dupree: my doctoral and thesis advisor at the Harvard-Smithsonian Center for Astrophysics for helping my work from the moment I arrived to Cambridge to this very day. Her scientific and moral support were essential for me to finish my thesis. I am very greatfull for her precious help and for providing me the opportunity to extend my knowledge by working at CfA and at the MMT Observatory.

Dr. József Vinkó: my advisor at the Department of Optics and Quantum Electronics for encouraging me in my university and PhD studies. I am very greatfull for his increadible help during my relocation to the USA and back to Hungary.

People I wish to acknowledge and have greatly improved my scientific research:

Dr. Eugene H. Avrett: for his tremendous help with PANDORA and advices in theoretical spectrum modeling.

Dr. Andrew Szentgyorgyi: for his help with observations at the MMT, which has greatly improved my understanding of high resolution spectroscopy.

I am greatfull to the following people who helped my research with their precious advices (in alphabetical order): **Balázs Csák, Dr. Gábor Fűrész, Dr. László L. Kiss, Dr. Robert L. Kurucz, Dr. László Szabados, Dr. Gyula M. Szabó, Tamás Szalai, Dr. Károly Szatmáry.**

I wish to thank all of my friends who supported me in my studies and in my personal life (in alphabetical order): **Roland Baksa, Bianka Bozsó, Orsolya Kálmán, Zoltán Keresztes, Dénes Könyves, Csaba Major, Gábor Nemes, Péter Németh, Éva Ocskó, Dr. András Pál, Péter Székely, László Szűcs, Dr. Noémi Tóth, Dr. Elaine Winston,** and many others, whom I might have missed to mention.

I would like to thank to Department of Optics and Quantum Electronics to provide workspace at the University of Szeged and for giving me the possibility to use the resources of the department.

I am grateful to the scientists at CfA who are developing and characterizing Hectochelle: **Dr. Nelson Caldwell, Dr. Daniel G. Fabricant, Dr. Gábor Fűrész, Dr. David W. Latham, and Dr. Andrew Szentgyorgyi**. I also would like to thank **John Roll** and **Maureen A. Conroy** for developing SPICE software, and **Mike Alegria, Perry Berlind, Michael Calkins, John McAfee, and Ale Milone** for their help during the observations.

I was supported in part by a SAO Predoctoral Fellowship, NASA, and the Hungarian OTKA Grant TS049872, T042509 and K76816. This research was also supported in part by the Smithsonian Astrophysical Observatory. Observations reported here were obtained at the MMT Observatory, a joint facility of the Smithsonian Institution and the University of Arizona.

And, last but not least, I would like to thank to my family for their love and undying support in my studies.

Bibliography

Alonso, A., Arribas, S., & Martínez-Roger, C. 1999, A&AS, 140, 261

Alonso, A., Arribas, S., & Martínez-Roger, C. 2001, A&A, 376, 1039

Arp, H. C. 1955, AJ, 60, 317

Auriere, M., & Cordoni, J. P. 1981, A&AS, 46, 347

Avrett, E. H., 1998, Solar Electromagnetic Radiation Study for Solar Cycle 22, ed. J. M. Pap, C. Frölich , & R. K. Ulrich, (Dordrecht:Kluwer), p. 449

Avrett, E. H., & Loeser, R. 2003, in IAU Symp. 210, Modeling of Stellar Atmospheres, ed. W. Weise & N. Piskunov (Dordrecht: Kluwer), A-21

Baldry, I. K., Taylor, M. M., Bedding, T. R., & Booth, A. J. 1997, MNRAS, 289, 979

Bates, B., Catney, M. G., & Keenan, F. P. 1990, MNRAS, 245, 238

Bates, B., Kemp, S. N., & Montgomery, A. S. 1993, A&AS, 97, 937

Bowen, G. H. & Willson, L. A. 1991, ApJ, 375, L53

Brown, A. 1951, ApJ, 113, 344

Boyer, M. L., McDonald, I., van Loon, J. T., Woodward, C. E., Gehrz, R. D., Evans, A., & Dupree, A. K. 2008, AJ, 135, 1395

Boyer, M. L., Woodward, C. E., van Loon, J. T., Gordon, K. D., Evans, A., Gehrz, R. D., Helton, L. A., & Polomski, E. F. 2006, AJ, 132, 1415

Buonanno, R., Corsi, C. E., and Fusi Pecci, F. 1985, A&A, 145, 97

Buonanno, R., Corsi, C. E., Fusi Pecci, F., Richer, H. B., & Fahlman, G. G. 1993, AJ, 105, 184

Buonanno, R., Corsi, C. E., Pulone, L., Fusi Pecci, F., & Bellazzini, M. 1998 A&A, 333, 505

Cacciari, C. et al. 2004, A&A, 413, 343

Cacciari, C., & Freeman, K. C. 1983, ApJ, 268, 185

Caloi, V., & D'Antona, F. 2005, A&A, 435, 987

Cardelli, J. A., Clayton, G. C., & Mathis, J. S. 1989, ApJ, 345, 245

Carney, B. W., Latham, D. W., Stefanik, R. P., Laird, J. B., & Morse, J. A. 2003, AJ, 125, 293

Catelan, M. 2000, ApJ, 531, 826

Catelan, M., Bellazzini, M., Landsman, W. B., Ferraro, F. R., Fusi Pecci, F., & Galleti, S. 2001, AJ, 122, 3171

Cavallo, R. M., & Nagar, N. M. 2000, AJ, 120, 1364

Cho, D. H., & Lee, S. G. 2007, AJ, 133, 2163

Christy, R. F. 1966, ApJ, 144, 108

Coelho, P., Barbuy, B., Meléndez, J., Schiavon, R. P., & Castilho, B. V. 2005, A&A, 443, 735

Cohen, J. G. 1976, ApJ, 203, L127

Cudworth, K. M. 1976, AJ, 81, 975

Cudworth, K. M., & Monet, D. G. 1979, AJ, 84, 774

D'Antona, F., Caloi, V., Montalbán, J., Ventura, P., & Gratton, R. 2002, A&A, 395, 69

D'Antona, F., & Caloi, V. 2008, MNRAS, 390, 693

Drukier, G. A., Cohn, H. N., Lugger, P. M., Slavin, S. D., Berrington, R. C., & Murphy, B. W. 2007, AJ, 133, 1041

Drukier, G. A., Slavin, S. D., Cohn, H. N., Lugger, P. M., Berrington, R. C., Murphy, B. W., & Seitzer, P. O. 1998, AJ, 115, 708

Dupree, A. K. 1986, ARAA, 24, 377

Dupree, A. K., Hartmann, L., & Avrett, E. H. 1984, ApJ, 281, L37

Dupree, A. K., Hartmann, L., Smith, G. H., Rodgers, A. W., Roberts, W. H., & Zucker, D. B. 1994, ApJ, 421, 542

Dupree, A. K., Li, T. Q., & Smith, G. H., 2007, AJ, 134, 1348

Dupree, A. K., Sasselov, D. D. & Lester, J. B. 1992, ApJ, 387, L85

Dupree, A. K., Smith, G. H., & Strader, J. 2009, AJ, submitted

Durrell, P. R., & Harris, W. E. 1993, AJ, 105, 1420

Elitzur, M. and Ivezić, Ž. 2001, MNRAS, 327, 403

Evans, A., Stickel, M., van Loon, J. T., Eyres, S. P. S., Hopwood, M. E. L., & Penny, A. J. 2003, A&A, 408, L9

Faulkner, D. J., Scott, T. R., Wood, P. R., & Wright, A. E. 1991, ApJ, 374, 45

Ferraro, F. R., Paltrinieri, B., Fusi Pecci, F., Cacciari, C., Dorman, B., & Rood, R. T. 1997, ApJ, 484, L145

Freire, P. C., Kramer, M., Lyne, A. G., Camilo, F., Manchester, R. N., & D'Amico, N. 2001, ApJ, 557, L105

Fusi Pecci, F., Ferraro, F. R., Bellazzini, M., Djorgovski, S., Piotto, G., & Buonanno, R. 2001, AJ, 105, 1145

Gebhardt, K., Pryor, C., Williams, T. B., Hesser, J. E., & Stetson, P. B. 1997, AJ, 113, 1026

Gratton, R. G., Pilachowski, C. A., & Sneden, C. 1984, A&A, 132, 11

Harris, W. E. 1996, AJ, 112, 1487

Helling, C., Winters, J. M. & Sedlmayr, E. 2000, A&A, 358, 651

Hurley, J. R., Pols, O. R. & Tout, C. A. 2000, MNRAS, 315, 543

Iben, I., Jr., & Rood, R. T. 1970, ApJ, 161, 587

Ivezić, Ž., Nenkova, M., & Elitzur, M. 1999, User Manual for DUSTY, (Lexington: Univ. Kentucky)

Johnson, C. I., Kraft, R. P., Pilachowski, C. A., Sneden, C., Ivans, I. I. & Benman, G. 2005, PASP, 117, 1308

Kadla, Z. I. 1966, Izv. Glav. Astron. Obs., 181, 93

Kemp, S. N., Bates, B. 1995, A&AS, 112, 513

Kopacki, G., Kołaczkowski, Z., & Pigulski, A. 2003, A&A, 398, 541

Kurucz, R. L. 1993, in ASPC 44: IAU Colloq. 138: Peculiar versus Normal Phenomena in A-type Related Stars, ed. Dworetsky, M. M., Castelli, F., & Faraggiana, R. (San Francisco: ASP), 87

Kustner, F. 1921, Veroeffentlichungen des Astronomisches Institute der Universitaet Bonn, 15, 1

Lee, J. W., & Carney, B. W. 1999, AJ, 118, 1373

Lee, Y. W., Demarque, P., & Zinn, R. 1994, ApJ, 423, 248

Lee, Y-W., et al. 2005, ApJ, 621, L57

Ludendorff, H. 1905, Publikationen des Astrophysikalischen Observatoriums zu Potsdam, 50, 1

Lupton, R. H., Gunn, J. E., & Griffin, R. F. 1987, AJ, 93, 1114

Lyons, M. A., Kemp, S. N., Bates, B., & Shaw, C. R. 1996, MNRAS, 280, 835

Mallia, E. A., & Pagel, B. E. J. 1981, MNRAS, 194, 421

Marshall, J. R., vanLoon, J. Th., Matsuura, M., Wood, P. R., Zijlstra, A. A. & Whitelock, P. A. 2004, MNRAS, 355, 1348

Mauas, P. J. D., Cacciari, C., & Pasquini, L. 2006, A&A, 454, 615

Mauas, P. J. D. 2007, in ASPC 368, Semiempirical Models of Solar and Stellar Active Chromospheres, ed. Heinzel, P., Dorotovič, I., & Rutten, R. J. (San Francisco: ASP), 203

Mayor, M. et al. 1984, A&A, 134, 118

McDonald, I., & van Loon, J. T. 2007, A&A, 476, 1261

McDonald I., van Loon, J. T., Decin, L., Boyer, M. L., Dupree, A. K., Evans A., Gehrz, R. D., & Woodward, C. E. 2009, MNRAS, in press (arXiv:0812.0326)

McLaughlin, D. E., & van der Marel, R. P. 2005, ApJS, 161, 304

Mészáros, Sz., Avrett, E. H., Dupree, A. K.: 2009, AJ, 138, 615

Mészáros, Sz., Dupree, A. K., & Szalai, T. 2009, AJ, 137, 4282

Mészáros, Sz., Dupree, A. K., & Szentgyorgyi, A. H. 2008, AJ, 135, 1117

Nardetto, N., Mourard, D., Kervella, P., Mathias, P., Mérand, A., & Bersier, D. 2006, A&A, 453, 309

Olofsson, H., González Delgado, D., Kerschbaum, F., & Schöier, F. L. 2002, A&A, 391, 1053

Origlia, L., Ferraro, F. R., Fusi Pecci, F., & Rood, R. T. 2002, ApJ, 571, 458

Origlia, L., Rood, R. T., Fabbri, S., Ferraro, F. R., Fusi Pecci, F., & Rich, R. M. 2007, ApJ, 667, L85

Perryman, M. A. C. et al. 1995, A&A, 304, 69

Peterson, R. C. 1981, ApJ, 248, L31

Peterson, R. C. 1982, ApJ, 258, 499

Peterson, R. C., Rood, R. T., & Crocker, D. A. 1995, ApJ, 453, 214

Peterson, R. C., Seitzer, P., & Cudworth, K. M. 1989, ApJ, 347, 251

Petterson, O. K. L., Cottrell, P. L., Albrow, M. D., & Fokin, A. 2005, MNRAS, 362, 1167

Pilachowski, C. A., Sneden, C., Kraft, R. P., & Langer, G. E. 1996, AJ, 112, 545

Piotto, G., Bedin, L. R., Anderson, J., King, I. R., Cassisi, S., Milone, A. P., Villanova, S., Pietrinferni, A., & Renzini, A. 2007, ApJ, 661, L53

Recio-Blanco, A., Aparicio, A., Piotto, G., de Angeli, F., & Djorgovski, S. G. 2006, A&A, 452, 875

Reimers, D. 1975, Mem. Soc. R. Sci Liége, 8, 369

Reimers, D. 1977, A&A, 61, 217

Renzini, A. 1981, in Phys. Proc. in Red Giants, I. Iben & A. Renzini, eds. (Dordrecht: Reidel), p. 431 (Dordrecht: Reidel), 319

Russeva, T., & Russev, R. 1980, IBVS, 1769

Sandage, A. 1970, ApJ, 162, 841

Sandage, A., & Walker, M. F. 1966, ApJ, 143, 313

Sandage, A., & Wallerstein, G. 1960, ApJ, 131, 598

Sandage, A., & Wildey, R. 1967, ApJ, 150, 469

Sarajedini, A. 1997, AJ, 113, 682

Sarajedini, A., Chaboyer, B., & Demarque, P. 1997, PASP, 109, 1321

Schröder, K. P., & Cuntz, M. 2005 ApJ, 630, L73

Searle, L., & Zinn, R. 1978, ApJ, 225, 357

Shetrone, M. D. 1994, PASP, 106, 161

Sills, A., & Pinsonneault, M. H. 2000, ApJ, 540, 489

Skrutskie, M.F. et al. 2006, AJ, 131, 1163

Smith, G. H., & Dupree, A. K. 1988, AJ, 95, 1547

Smith, G. H., Dupree, A. K., & Strader, J. 2004, PASP, 116, 819

Smith, G. H., Woodsworth, A. W., & Hesser, J. E. 1995, MNRAS, 273, 632

Sneden, C., Kraft, R. P., Shetrone, M. D., Smith, G. H., Langer, G. E., & Prosser, C. F. 1997, AJ, 114, 1964

Sneden, C., Pilachowski, C. A., & Kraft, R. P. 2000, AJ, 120, 1351

Soderberg, A. M., Pilachowski, C. A., Barden, S. C., and Willmarth, D., & Sneden, C. 1999, PASP, 111, 1233

Soker, N., Rappaport, S., & Fregeau, J. 2001, ApJ, 563, L87

Struck, C., Smith, D. C., Willson, L. A., Turner, G., & Bowen, G. H. 2004, MNRAS, 353, 559

Stetson, P. B., Vandenberg, D. A., & Bolte, M. 1996, PASP, 108, 560

Sweigart, A. V. 1997, ApJ, 474, L23

Sweigart, A. V., Greggio, L., & Renzini, A. 1990, ApJ, 364, 527

Szentgyorgyi, A. H., Cheimets, P., Eng, R, Fabricant, D. G., Geary, J. C., Hartmann, L., Pieri, M. R., & Roll, J. B. 1998, in Proc. SPIE Vol. 3355, Optical Astronomical Instrumentation, ed. Sandro D'Odorico, 242

Taylor, J. H., & Cordes, J. M. 1993, ApJ, 411, 674

Vandenberg, D. A., Bolte, M., & Stetson, P. B. 1990, AJ, 100, 445

van der Marel, R. P., Gerssen, J., Guhathakurta, P., Peterson, R. C., & Gebhardt, K. 2002, AJ, 124, 3255

van Loon, J. T., Stanimirović, S., Evans, A., & Muller, E. 2006, MNRAS, 365, 1277

Wachter, A. and Schröder, K.-P. and Winters, J. M. and Arndt, T. U., & Sedlmayr, E. 2002, A&A, 384, 452

Wachter, A., Winters, J. M., Schröder, K., & Sedlmayr, E. 2008, A&A, in press (arXiv:0805.3656)

Zarro, D. M. & Rodgers, A. W. 1983, ApJS, 53, 815

Chapter 7

Appendix

Table 7.1. Photometric Data of Observed Cluster Members in M15

ID No. [a]	*RA*(2000) [b]	Dec(2000) [b]	B	V	J	H	K	B−V	V−K	Obs. [c]
B5 [d]	21 29 08.43	+12 09 11.8	14.63	13.51	11.368	10.726	10.645	1.12	2.87	1,3,4
B6 [d]	21 29 12.36	+12 10 49.8	14.69	13.54	11.411	10.775	10.656	1.15	2.88	1,2,3,4
B16 [d]	21 29 53.12	+12 12 31.1	14.85	13.76	11.732	11.154	11.029	1.09	2.73	3
B30 [d]	21 30 44.13	+12 11 22.6	14.80	13.69	11.496	10.927	10.807	1.11	2.88	1,2,3,4
C3 [e]	21 29 13.06	+12 11 15.0	15.49	14.65	12.698	12.156	12.039	0.84	2.61	1,2,3,4
C20 [e]	21 29 52.32	+12 19 39.7	16.35	15.46	13.646	13.089	12.991	0.89	2.47	1,2,3,4
C35 [e]	21 30 49.28	+12 07 31.2	15.77	15.14	13.398	12.965	12.855	0.63	2.29	1
GEB 254 [f]	21 29 58.15	+12 09 46.7	14.55 [g]	13.24 [g]	9.560	9.964	9.777	1.31	3.46	4,5
GEB 289 [f]	21 29 59.37	+12 10 02.9	14.54 [g]	13.50 [g]	11.079	10.449	10.311	1.04	3.12	3,5
K12	21 29 30.77	+12 06 32.7	15.84	15.05	13.386	12.886	12.851	0.79	2.20	1,2,3,4
K21	21 29 33.12	+12 12 51.0	15.74	15.00	13.323	12.834	12.726	0.74	2.27	2,3,4
K22	21 29 33.53	+12 04 55.3	15.42	14.41	12.482	11.938	11.809	1.01	2.60	1,2,3,4
K26	21 29 34.62	+12 03 19.2	15.87	15.00	13.197	12.693	12.566	0.87	2.43	1,2,3,4
K27	21 29 35.08	+12 06 03.7	15.84	15.09	13.451	12.994	12.894	0.75	2.20	2,3,4
K31	21 29 35.87	+12 08 27.3	16.04	15.21	13.529	13.006	12.882	0.83	2.33	2,3,4
K42	21 29 38.00	+12 11 58.2	16.10	15.23	13.452	12.925	12.887	0.87	2.34	3,4
K47	21 29 38.72	+12 11 53.0	15.13	14.11	12.152	11.588	11.488	1.02	2.62	1,2
K56	21 29 40.04	+12 16 00.2	16.27	15.37	13.651	13.107	12.966	0.90	2.40	1,2,3,4
K60	21 29 41.25	+12 07 19.4	16.07	15.26	13.532	12.991	12.928	0.81	2.33	3,4
K64	21 29 42.96	+12 09 53.4	16.11	15.25	13.504	13.003	12.884	0.86	2.37	1,2,3,4
K69	21 29 43.77	+12 08 33.3	15.36	14.45	12.501	11.969	11.854	0.91	2.60	1,2,4
K70	21 29 43.59	+12 15 47.4	15.27	14.32	12.338	11.746	11.653	0.95	2.67	1
K77	21 29 44.65	+12 07 30.8	14.92	13.82	11.752	11.148	11.026	1.10	2.79	1,2,3,4
K87	21 29 45.81	+12 08 45.5	14.87	13.80	11.776	11.225	11.075	1.07	2.73	4
K89	21 29 46.07	+12 11 31.5	15.35	14.53	12.564	12.055	11.955	0.82	2.58	2,3,4
K92	21 29 46.70	+12 03 20.7	16.14	15.20	13.359	12.848	12.791	0.94	2.41	1,2,3,4
K105	21 29 47.39	+12 09 04.7	16.26	15.29	13.477	13.023	12.940	0.97	2.35	1,4
K112	21 29 47.78	+12 11 30.7	15.96	15.08	13.167	12.654	12.592	0.88	2.49	4
K114	21 29 47.87	+12 08 45.4	14.99	13.85	11.781	11.245	11.080	1.14	2.77	3
K129	21 29 48.63	+12 11 45.8	15.23	14.26	12.292	11.725	11.620	0.97	2.64	3
K133	21 29 48.84	+12 10 25.3	15.99	15.10	13.435	13.014	12.898	0.89	2.20	2,3
K136	21 29 49.13	+12 09 03.7	15.80	15.00	13.217	12.811	12.707	0.80	2.29	4
K137	21 29 49.45	+12 08 27.0	16.36	15.38	13.628	13.134	13.059	0.98	2.32	3
K144	21 29 49.79	+12 11 05.9	14.40	13.06	10.745	10.053	9.944	1.34	3.12	2,4
K145	21 29 49.80	+12 12 29.9	16.24	15.36	13.557	13.090	12.957	0.88	2.40	1,2,3
K146	21 29 49.94	+12 08 05.3	14.69	13.57	11.427	10.843	10.726	1.12	2.84	2
K151	21 29 50.14	+12 07 52.2	16.00	15.11	13.303	12.757	12.699	0.89	2.61	3
K152	21 29 50.16	+12 06 40.7	16.11	15.25	13.553	12.999	12.877	0.86	2.37	1,2,3
K153	21 29 49.92	+12 18 12.1	16.23	15.48	13.684	13.195	13.067	0.75	2.41	1,3,4
K158	21 29 50.29	+12 09 02.8	15.04	14.16	12.380	11.879	11.806	0.88	2.35	2
K202	21 29 51.89	+12 06 38.9	16.06	15.17	13.420	12.906	12.838	0.89	2.33	3
K224	21 29 52.31	+12 10 51.5	14.59	13.39	11.235	10.672	10.515	1.20	2.88	1,2,3,5
K238	21 29 52.65	+12 10 44.0	14.52	13.24	11.041	10.429	10.305	1.28	2.94	4,5
K255	21 29 53.12	+12 12 31.1	14.85	13.76	11.732	11.154	11.029	1.09	2.73	1,2
K260	21 29 53.31	+12 09 34.0	14.79	13.99	12.486	12.125	12.053	0.80	1.94	1,2
K272	21 29 53.57	+12 09 10.7	14.67	13.48	11.307	10.736	10.606	1.19	2.87	3,5
K288	21 29 53.79	+12 10 20.3	14.85	13.71	11.667	11.120	10.966	1.14	2.74	1,3
K328	21 29 54.73	+12 08 59.2	14.86	13.70	11.591	11.065	10.906	1.16	2.80	2,4,5
K337	21 29 55.05	+12 02 48.5	15.75	14.76	12.863	12.311	12.200	0.99	2.56	2,3,4
K341	21 29 54.93	+12 13 22.5	14.18	12.81	10.455	9.796	9.695	1.37	3.12	1,2,3,4

Table 7.1 (cont'd)

ID No. [a]	*RA*(2000) [b]	Dec(2000) [b]	B	V	J	H	K	B−V	V−K	Obs. [c]
K361	21 29 55.29	+12 09 13.7	14.97	13.96	12.029	11.475	11.364	1.01	2.60	3
K393	21 29 55.73	+12 11 33.8	14.46	13.25	11.042	10.452	10.315	1.21	2.94	1,2
K421	21 29 56.18	+12 10 17.9	13.92	12.72	10.414	9.781	9.649	1.20	3.07	3,5
K431	21 29 56.18	+12 12 33.8	14.33	13.03	10.759	10.144	10.039	1.30	2.99	1,2,3
K447	21 29 56.45	+12 10 29.4	14.32	13.25	11.132	10.613	10.468	1.07	2.78	2
K462	21 29 56.67	+12 09 46.3	14.45	12.90	10.534	9.860	9.722	1.55	3.18	2
K476	21 29 56.72	+12 13 10.5	15.55	14.63	12.714	12.202	12.130	0.92	2.50	2
K479	21 29 56.79	+12 10 27.0	13.99	12.68	10.276	9.678	9.524	1.31	3.16	4,5
K482	21 29 56.94	+12 08 44.7	15.25	14.38	12.632	12.195	12.071	0.87	2.31	3
K506	21 29 57.43	+12 08 21.5	15.62	14.75	12.848	12.299	12.232	0.87	2.52	4
K550	21 29 58.03	+12 11 54.2	16.00	15.10	13.357	12.833	12.742	0.90	2.36	2,3,4
K567	21 29 58.33	+12 09 12.8	14.46	13.25	11.129	10.508	10.414	1.21	2.84	3,5
K582	21 29 58.60	+12 08 08.0	15.32	14.48	12.829	12.370	12.305	0.84	2.18	1
K583	21 29 58.57	+12 09 21.4	14.26	12.83	10.315	9.726	9.569	1.43	3.26	1
K647	21 29 59.46	+12 08 35.6	14.79	13.60	11.388	10.807	10.686	1.19	2.91	4
K654	21 29 59.53	+12 11 52.6	16.06	15.16	13.350	12.861	12.785	0.90	2.38	4
K672	21 29 59.81	+12 11 10.7	14.84	13.84	11.837	11.290	11.211	1.00	2.63	3,5
K677	21 29 59.99	+12 06 26.6	15.82	15.00	13.330	12.824	12.811	0.82	2.19	3,4
K691	21 30 00.03	+12 13 39.5	15.64	14.80	12.859	12.321	12.217	0.84	2.58	1,2
K702	21 30 00.34	+12 10 50.9	14.47	12.99	10.609	10.080	9.910	1.48	3.08	1,2
K709	21 30 00.38	+12 07 36.4	14.75	13.61	11.535	10.944	10.847	1.14	2.76	3,4
K736	21 30 00.63	+12 09 28.4	15.02	14.01	12.063	11.474	11.346	1.01	2.66	3,5
K757	21 30 00.91	+12 08 57.1	14.31	12.88	10.383	9.759	9.605	1.43	3.28	1,2
K800	21 30 01.65	+12 12 30.3	16.23	15.12	13.029	12.575	12.761	1.11	2.36	1
K825	21 30 02.25	+12 11 21.5	14.13	12.79	10.227	9.582	9.433	1.34	3.36	3
K846	21 30 02.78	+12 06 55.7	15.05	13.97	11.918	11.388	11.247	1.08	2.72	1,4,5
K853	21 30 02.74	+12 10 43.9	14.27	12.88	10.469	9.860	9.727	1.39	3.15	1,2
K866	21 30 03.09	+12 10 21.8	15.72	14.70	12.885	12.322	12.269	1.02	2.43	3
K875	21 30 03.17	+12 13 28.7	15.05	14.10	12.180	11.659	11.506	0.95	2.60	1,2
K879	21 30 03.50	+12 03 12.5	15.22	14.16	12.205	11.615	11.527	1.06	2.63	1,2
K902	21 30 04.00	+12 08 57.8	15.90	14.84	13.003	12.483	12.364	1.06	2.48	3,4
K906	21 30 04.09	+12 07 27.1	16.24	15.37	13.560	13.046	13.009	0.87	2.36	3
K919	21 30 04.32	+12 10 56.2	14.80	13.60	11.459	10.893	10.757	1.20	2.84	1,2
K925	21 30 04.62	+12 08 53.7	15.61	14.62	12.733	12.231	12.067	0.99	2.55	1,2
K926	21 30 04.65	+12 07 40.5	15.89	15.18	13.591	13.186	13.107	0.71	2.07	4
K932	21 30 04.75	+12 11 10.3	15.14	14.09	12.099	11.534	11.438	1.05	2.65	4
K947	21 30 05.18	+12 13 20.3	15.26	14.29	12.311	11.724	11.613	0.97	2.68	2
K954	21 30 05.54	+12 08 55.3	15.32	14.33	12.357	11.835	11.719	0.99	2.61	4
K969	21 30 06.37	+12 06 59.3	14.61	13.45	11.364	10.829	10.700	1.16	2.75	1,4
K979	21 30 06.96	+12 07 46.5	15.09	14.23	12.454	11.978	11.898	0.86	2.33	1
K989	21 30 07.30	+12 10 50.7	16.02	15.13	13.556	13.078	12.950	0.89	2.18	3
K993	21 30 07.40	+12 10 33.1	15.01	14.01	11.964	11.399	11.264	1.00	2.75	1
K1010	21 30 08.42	+12 09 42.1	15.88	14.97	13.167	12.630	12.545	0.91	2.43	4
K1014	21 30 08.95	+12 08 49.1	15.61	14.70	13.003	12.483	12.364	0.91	2.34	3
K1029	21 30 09.71	+12 13 42.4	14.74	13.56	11.349	10.739	10.601	1.18	2.96	1,2
K1030	21 30 09.78	+12 12 54.4	15.17	14.14	12.109	11.538	11.401	1.03	2.74	1,2
K1033	21 30 09.89	+12 10 52.5	15.41	14.44	12.447	11.882	11.773	0.97	2.67	1,2
K1040	21 30 10.49	+12 10 06.2	14.60	13.40	11.151	10.562	10.438	1.20	2.96	3
K1049	21 30 11.31	+12 01 48.5	15.53	14.56	12.604	12.038	11.934	0.97	2.63	1
K1054	21 30 11.38	+12 08 41.2	15.19	14.20	12.181	11.626	11.517	0.99	2.68	1,2

Table 7.1 (cont'd)

ID No. [a]	*RA*(2000) [b]	Dec(2000) [b]	B	V	J	H	K	B−V	V−K	Obs. [c]
K1056	21 30 11.69	+12 10 33.7	15.71	14.79	12.907	12.384	12.227	0.92	2.56	4
K1069	21 30 14.26	+12 09 23.4	15.42	14.60	12.660	12.125	12.006	0.82	2.60	4
K1073	21 30 14.95	+12 10 20.7	15.19	14.18	12.127	11.593	11.465	1.01	2.72	1,2,3,4
K1074	21 30 15.23	+12 11 34.5	16.22	15.26	13.406	12.910	12.786	0.96	2.47	1,3,4
K1079	21 30 15.66	+12 08 22.9	15.09	14.09	12.061	11.517	11.408	1.00	2.68	1,2
K1083	21 30 15.78	+12 16 59.6	16.19	15.43	13.566	13.053	12.987	0.76	2.44	1,2,3
K1084	21 30 16.06	+12 13 34.3	15.39	14.42	12.415	11.860	11.772	0.97	2.65	1,2,3
K1097	21 30 21.04	+12 13 00.8	16.21	15.41	13.631	13.127	13.025	0.80	2.39	1,2,3,4
K1106	21 30 22.71	+12 17 59.6	15.54	14.71	12.719	12.163	12.044	0.83	2.67	2,3
K1136	21 30 31.78	+12 08 54.8	15.70	14.87	13.005	12.483	12.329	0.83	2.54	1,2,3,4

[a]Kustner (1921) is the identification for the majority of the stars denoted by K.

[b]2MASS coordinates (Skrutskie et al., 2006).

[c]Observations: 1: 2005 May 22; 2: 2006 May 11; 3: 2006 October 4; 4: 2006 October 7; 5: Dusty giants identified by Boyer et al. (2006).

[d]Brown (1951).

[e]Cudworth (1976).

[f]Gebhardt et al. (1997).

[g]B and V magnitudes are taken from Auriere & Cordoni (1981).

Note. — The visual photometry is taken from Cudworth (1976); J,H,K photometry is taken from the 2MASS Catalog (Skrutskie et al., 2006).

Table 7.2. Photometric Data of Observed Cluster Members in M13

ID No. [a]	RA(2000) [b]	Dec(2000) [b]	B	V	J	H	K	B−V	V−K	Obs. [c]
III-65 [d]	16 41 39.091	+36 23 51.40	16.04	15.22	13.690	13.220	13.071	0.82	2.15	1,3,5
K188 [e]	16 40 42.982	+36 27 41.88	14.44	13.39	11.410	10.784	10.704	1.05	2.69	1,3,5
K210 [e]	16 40 56.378	+36 22 18.51	15.21	14.33	12.580	12.028	11.966	0.88	2.36	1,3,5
K220 [e]	16 41 02.608	+36 26 15.81	15.74	14.98	13.353	12.899	12.833	0.76	2.15	1,2,4,5,6
K223 [e]	16 41 05.075	+36 28 20.85	15.56	14.71	13.093	12.565	12.494	0.85	2.22	2,4,6
K224 [e]	16 41 06.155	+36 25 22.71	15.36	14.52	12.834	12.312	12.225	0.84	2.30	2,4,6
K228 [e]	16 41 06.488	+36 28 13.69	14.37	13.31	11.318	10.722	10.606	1.06	2.70	1,3,5
K246 [e]	16 41 40.816	+36 34 11.49	15.06	14.13	12.308	11.781	11.657	0.93	2.47	2,4
K272 [e]	16 41 18.271	+36 20 49.67	16.25	15.47	13.884	13.434	13.329	0.78	2.14	1,3,5
K342 [e]	16 41 28.578	+36 21 49.75	15.84	15.02	13.472	12.957	12.896	0.82	2.12	1,2,3,4,5,6
K366 [e]	16 41 30.138	+36 35 28.46	15.66	14.86	13.143	12.631	12.565	0.80	2.30	1,2,4,5,6
K422 [e]	16 41 36.438	+36 17 08.17	14.99	14.02	12.195	11.652	11.568	0.97	2.45	1,2,3,4,5,6
K517 [e]	16 41 48.191	+36 35 41.36	16.13	15.37	13.725	13.275	13.194	0.76	2.18	1,3,5
K549 [e]	16 41 51.909	+36 19 35.08	15.60	14.72	13.092	12.537	12.472	0.88	2.25	2,3,4,6
K585 [e]	16 41 57.474	+36 19 55.90	15.72	14.84	13.174	12.628	12.609	0.88	2.23	2,4,6
K647 [e]	16 42 11.164	+36 18 22.56	15.61	14.71	13.019	12.540	12.488	0.90	2.22	1,2,3,4,5,6
K650 [e]	16 42 12.779	+36 29 21.13	15.67	14.83	13.169	12.679	12.637	0.84	2.19	2,4,6
K652 [e]	16 42 13.584	+36 28 36.56	15.88	15.08	13.471	12.969	12.924	0.80	2.16	2,4,6
K656 [e]	16 42 14.820	+36 27 19.94	14.16	13.04	10.935	10.314	10.191	1.12	2.85	1,5
K658 [e]	16 42 16.507	+36 26 13.77	15.69	14.71	13.020	12.537	12.453	0.98	2.26	1,2,3,4,5,6
K666 [e]	16 42 18.896	+36 30 15.61	15.70	14.86	13.187	12.671	12.606	0.84	2.25	2,4,6
K674 [e]	16 42 21.270	+36 33 53.35	15.06	14.26	12.680	12.230	12.147	0.80	2.11	1,3,5
K695 [e]	16 42 35.704	+36 19 54.80	15.81	14.92	13.251	12.771	12.722	0.89	2.20	1,3,5
L4	16 41 09.668	+36 26 44.88	15.66	14.82	13.174	12.660	12.568	0.84	2.25	2,4,6
L12	16 41 13.895	+36 25 02.68	15.75	14.95	13.360	12.840	12.825	0.80	2.13	1,2,3,4,5,6
L13	16 41 13.592	+36 30 33.40	15.67	14.82	13.145	12.634	12.564	0.85	2.26	1,2,5
L18	16 41 15.218	+36 29 24.01	14.71	13.78	11.853	11.290	11.206	0.93	2.57	1,3,5
L19	16 41 15.509	+36 31 02.84	16.03	15.34	13.661	13.169	13.115	0.69	2.23	1,2,3,5
L20	16 41 15.705	+36 27 50.07	15.58	14.74	13.090	12.615	12.532	0.84	2.21	2,3,4,6
L22	16 41 15.834	+36 33 17.78	15.74	14.93	13.271	12.739	12.690	0.81	2.24	2,3,4,6
L26	16 41 17.006	+36 25 47.96	14.59	13.58	11.676	11.088	10.991	1.01	2.59	1,2,3,4,5,6
L29	16 41 17.724	+36 29 29.90	15.35	14.51	12.785	12.283	12.186	0.84	2.32	2,4,6
L31	16 41 18.311	+36 26 40.79	15.57	14.74	13.091	12.589	12.506	0.83	2.23	2,4,6
L32	16 41 18.633	+36 28 43.41	15.89	15.12	13.489	13.003	12.937	0.77	2.18	1,3,5
L34	16 41 18.822	+36 28 23.29	15.78	14.96	13.365	12.822	12.777	0.82	2.18	2,4,6
L38	16 41 19.230	+36 27 14.48	15.54	14.72	13.036	12.529	12.446	0.82	2.27	2,4,6
L43	16 41 19.832	+36 24 38.20	14.58	13.59	11.845	11.281	11.191	0.99	2.40	1,2,3,4,5,6
L70	16 41 23.537	+36 30 17.34	13.71	12.12	9.394	8.659	8.527	1.59	3.59	1,3,5
L72	16 41 24.086	+36 25 30.66	13.62	12.32	10.018	9.353	9.242	1.30	3.08	1,2,3,5
L80	16 41 24.529	+36 30 49.23	15.64	14.87	13.274	12.768	12.714	0.77	2.16	2,4,6
L91	16 41 26.770	+36 23 25.62	15.62	14.77	13.107	12.578	12.551	0.85	2.22	2,4,6
L93	16 41 26.841	+36 25 28.66	15.64	14.85	13.262	12.720	12.654	0.79	2.20	2
L95	16 41 27.071	+36 26 50.83	15.57	14.76	13.106	12.594	12.516	0.81	2.24	2,4,6
L96	16 41 27.092	+36 28 00.29	13.79	12.52	10.236	9.575	9.460	1.27	3.06	1,3,5
L101	16 41 27.357	+36 29 30.49	15.84	15.09	13.555	13.067	13.027	0.75	2.06	2,4,6
L102	16 41 27.299	+36 32 22.63	15.64	14.82	13.147	12.644	12.563	0.82	2.26	1,2,3,4,5,6
L109	16 41 28.156	+36 25 27.47	14.27	13.32	11.444	10.888	10.809	0.95	2.51	1,3,5
L110	16 41 28.268	+36 23 00.54	15.37	14.50	12.812	12.320	12.227	0.87	2.27	1,2,3,4,5,6
L115	16 41 28.252	+36 30 01.73	15.51	14.72	13.032	12.554	12.493	0.79	2.23	2,4,6
L137	16 41 29.702	+36 32 13.64	15.44	14.58	12.904	12.359	12.315	0.86	2.27	1,2,3,4,5,6

Table 7.2 (cont'd)

ID No. [a]	RA(2000) [b]	Dec(2000) [b]	B	V	J	H	K	B−V	V−K	Obs. [c]
L140	16 41 30.134	+36 26 35.49	14.92	14.24	12.715	12.267	12.242	0.68	2.00	1,3,5
L158	16 41 30.535	+36 29 43.48	13.89	12.70	10.505	9.827	9.727	1.19	2.97	1,3,5
L168	16 41 30.829	+36 30 13.08	14.52	13.62	11.846	11.327	11.261	0.90	2.36	1,3,5
L169	16 41 31.072	+36 25 58.74	13.94	12.78	10.650	9.988	9.891	1.16	2.89	1,5
L180	16 41 31.499	+36 26 15.25	15.57	14.80	13.261	12.786	12.676	0.77	2.12	2,4,6
L199	16 41 32.538	+36 24 42.44	13.59	12.20	9.779	9.057	8.944	1.39	3.26	1,3,5
L219	16 41 33.276	+36 32 28.55	15.41	14.55	12.828	12.296	12.221	0.86	2.33	2,4,6
L239	16 41 33.875	+36 30 27.11	15.62	14.78	13.127	12.579	12.536	0.84	2.24	2
L250	16 41 34.488	+36 26 36.56	13.72	12.37	10.037	9.356	9.211	1.35	3.16	1,3,5
L252	16 41 34.355	+36 30 13.42	13.89	12.67	10.437	9.773	9.643	1.22	3.03	1,3,5
L255	16 41 34.275	+36 32 41.10	16.10	15.37	13.814	13.353	13.336	0.73	2.03	1,3,5
L271	16 41 35.152	+36 24 03.18	15.68	14.87	13.153	12.659	12.631	0.81	2.24	2,4,6
L316	16 41 36.295	+36 25 10.40	13.81	12.58	10.302	9.652	9.513	1.23	3.07	1,3,5
L327	16 41 36.667	+36 27 20.73	14.53	13.78	12.044	11.604	11.479	0.75	2.30	2,4,6
L330	16 41 36.875	+36 24 25.95	15.59	14.78	13.123	12.639	12.598	0.81	2.18	2,4,6
L345	16 41 37.057	+36 28 48.45	14.09	12.88	10.789	10.192	10.063	1.21	2.82	2,4,6
L373	16 41 37.731	+36 29 29.42	14.94	14.20	12.700	12.268	12.170	0.74	2.03	1,3,5
L384	16 41 38.065	+36 27 49.41	13.76	12.48	10.323	9.661	9.541	1.28	2.94	2,4,6
L395	16 41 38.293	+36 25 32.77	15.72	14.93	13.366	12.866	12.802	0.79	2.13	2,4,6
L403	16 41 38.695	+36 22 40.09	14.24	13.19	11.169	10.548	10.433	1.05	2.76	1,3,5
L414	16 41 38.702	+36 25 38.03	13.61	12.14	9.622	8.883	8.736	1.47	3.40	1,3,5
L423	16 41 38.629	+36 30 36.93	15.17	14.31	12.539	12.015	11.938	0.86	2.37	1,3,5
L436	16 41 39.024	+36 26 35.27	14.28	13.43	11.518	10.980	10.865	0.85	2.57	1,3,5
L444	16 41 39.396	+36 24 01.39	15.52	14.72	13.076	12.569	12.517	0.80	2.20	2,4,6
L465	16 41 39.619	+36 27 38.15	13.81	12.50	10.370	9.712	9.583	1.31	2.92	1,3,5
L469	16 41 39.451	+36 32 02.97	15.46	14.61	12.929	12.414	12.337	0.85	2.27	1,3,5
L530	16 41 40.522	+36 31 36.50	15.37	14.59	12.926	12.407	12.322	0.78	2.27	2,4,6
L549	16 41 41.088	+36 27 55.00	13.65	12.58	10.543	10.093	9.996	1.07	2.58	1,3,5
L592	16 41 41.895	+36 28 18.46	14.16	13.10	11.130	10.530	10.423	1.06	2.68	2,4,6
L598	16 41 41.960	+36 26 51.85	13.64	12.00	9.276	8.493	8.335	1.64	3.67	1,3,5
L637	16 41 42.567	+36 29 57.65	15.57	14.69	13.052	12.580	12.482	0.88	2.21	2,4,6
L648	16 41 42.776	+36 30 56.21	15.29	14.65	13.373	13.023	12.786	0.64	1.86	2,4,6
L691	16 41 43.946	+36 24 41.93	15.62	14.88	13.312	12.791	12.713	0.74	2.17	2,4,6
L719	16 41 44.308	+36 29 21.13	15.45	14.69	13.114	12.634	12.614	0.76	2.08	1,2,4,5,6
L726	16 41 44.784	+36 23 27.39	14.66	13.68	11.765	11.218	11.104	0.98	2.58	1,3,5
L745	16 41 44.862	+36 30 51.47	13.82	12.54	10.161	9.471	9.351	1.28	3.19	1,3,5
L756	16 41 45.308	+36 26 45.01	14.65	13.84	12.072	11.556	11.515	0.81	2.33	1,3,5
L773	16 41 45.451	+36 30 11.41	14.21	13.21	11.241	10.638	10.554	1.00	2.66	1,3,5
L828	16 41 46.613	+36 30 05.01	15.72	14.97	13.385	12.912	12.871	0.75	2.10	2,4,6
L835	16 41 47.032	+36 25 57.67	13.56	12.09	9.625	8.902	8.763	1.47	3.33	1,3,5
L846	16 41 47.086	+36 29 13.78	15.30	14.59	13.225	12.698	12.798	0.71	1.79	2,4,6
L863	16 41 47.682	+36 29 08.15	14.16	12.98	11.029	10.353	10.229	1.18	2.75	1,3,5
L867	16 41 48.055	+36 25 05.91	15.56	14.78	13.107	12.626	12.579	0.78	2.20	2,4,6
L869	16 41 48.143	+36 23 36.28	15.46	14.62	12.944	12.439	12.405	0.84	2.22	2,4,6
L883	16 41 48.042	+36 31 39.29	15.51	14.69	13.005	12.536	12.481	0.82	2.21	2,4,6
L920	16 41 49.340	+36 25 12.51	14.58	13.72	11.949	11.442	11.362	0.86	2.36	1,3,5
L954	16 41 50.310	+36 24 15.70	13.63	12.09	9.468	8.730	8.568	1.54	3.52	1,3,5
L955	16 41 50.376	+36 23 41.76	14.82	13.92	12.026	11.469	11.382	0.90	2.54	2,4
L961	16 41 50.245	+36 29 43.19	14.30	13.39	11.570	11.032	10.973	0.91	2.42	1,3,5
L965	16 41 50.679	+36 26 07.63	15.48	14.66	13.009	12.557	12.449	0.82	2.21	2,4,6

Table 7.2 (cont'd)

ID No. [a]	RA(2000) [b]	Dec(2000) [b]	B	V	J	H	K	B−V	V−K	Obs. [c]
L973	16 41 50.928	+36 28 54.55	13.65	12.04	9.357	8.591	8.452	1.61	3.59	1,3,5
L987	16 41 51.960	+36 24 33.75	15.20	15.07	14.816	14.796	14.865	0.13	0.21	1,5
L1005	16 41 52.624	+36 28 26.63	15.57	14.81	13.124	12.690	12.575	0.76	2.24	2,4,6
L1009	16 41 53.225	+36 25 23.47	15.40	14.59	12.978	12.453	12.407	0.81	2.18	2,4,6
L1011	16 41 53.459	+36 24 37.61	15.52	14.73	13.053	12.559	12.499	0.79	2.23	2,4,6
L1023	16 41 54.114	+36 26 09.27	14.11	12.99	11.005	10.384	10.285	1.12	2.71	1,3,5
L1024	16 41 54.361	+36 27 13.90	15.62	14.87	13.185	12.659	12.567	0.75	2.30	2,4,6
L1025	16 41 54.217	+36 30 14.43	16.02	15.26	13.644	13.175	13.052	0.76	2.21	2,4,6
L1032	16 41 54.949	+36 27 42.12	14.73	13.81	11.994	11.445	11.345	0.92	2.47	1,3,5
L1043	16 41 55.434	+36 33 26.69	14.33	13.49	11.793	11.288	11.229	0.84	2.26	1,3,5
L1048	16 41 56.598	+36 30 02.78	15.22	14.23	12.472	11.914	11.846	0.99	2.38	1,3,5
L1050	16 41 57.420	+36 23 15.44	15.20	14.29	12.500	11.973	11.893	0.91	2.40	1,3,5
L1065	16 41 58.890	+36 29 09.42	15.46	14.64	12.927	12.415	12.349	0.82	2.29	2,4,6
L1073	16 42 00.855	+36 23 33.86	13.89	12.88	10.826	10.233	10.130	1.01	2.75	1,3,5
L1077	16 42 01.015	+36 28 12.81	16.00	15.31	13.746	13.264	13.186	0.69	2.12	2,4,6
L1080	16 42 01.795	+36 23 22.71	15.60	14.76	13.101	12.625	12.536	0.84	2.22	2,4,6
L1091	16 42 02.557	+36 32 32.68	15.63	14.79	13.150	12.633	12.558	0.84	2.23	2,4,6
L1097	16 42 03.408	+36 30 18.25	15.32	14.40	12.691	12.136	12.061	0.92	2.34	1,5
L1102	16 42 04.984	+36 31 36.54	16.24	15.45	13.842	13.382	13.259	0.79	2.19	1,3,5
L1103	16 42 05.812	+36 22 34.24	15.96	15.22	13.737	13.276	13.204	0.74	2.02	2,4,6
L1114	16 42 09.859	+36 22 26.18	14.86	14.12	12.430	11.969	11.905	0.74	2.22	1,3,5
L1115	16 42 09.432	+36 33 59.16	15.88	15.02	13.415	12.948	12.913	0.86	2.11	1,3,5
L1118	16 42 10.939	+36 24 33.22	15.76	14.84	13.138	12.658	12.617	0.92	2.22	1,2,3,4,5,6

[a]Ludendorff (1905) is the identification for the majority of the stars denoted by L.

[b]2MASS coordinates (Skrutskie et al., 2006)

[c]Observations: 1: 2006 March 14 (OB25), 2: 2006 May 10 (OB25), 3: 2006 March 16 (RV31), 4: 2006 May 10 (RV31), 5: 2006 March 16 (Ca41), 6: 2006 May 10 (Ca41).

[d]Arp (1955)

[e]Kadla (1966)

Note. — The visual photometry is taken from Cudworth & Monet (1979), J,H,K photometry is taken from the 2MASS Catalog (Skrutskie et al., 2006).

Table 7.3. Photometric Data of Observed Cluster Members in M92

ID No. [a]	RA(2000) [b]	Dec(2000) [b]	B	V	J	H	K	B−V	V−K	Obs. [c]
I-14	17 17 28.77	+43 10 02.8	15.47	14.74	13.155	12.644	12.592	0.73	2.148	1,2,3,4,5
I-40	17 17 22.68	+43 08 50.5	15.51	14.78	13.258	12.777	12.640	0.73	2.140	1,3,4
I-67	17 17 21.24	+43 08 27.0	14.24	13.32	11.406	10.870	10.766	0.92	2.554	1,3,4
I-68	17 17 21.73	+43 08 15.8	15.36	14.61	13.243	12.825	12.661	0.75	1.949	2,5
II-6	17 17 50.37	+43 13 46.0	15.89	15.14	13.541	13.002	12.992	0.75	2.148	1,2,3,4,5
II-24	17 17 22.05	+43 12 03.4	15.32	14.54	12.867	12.335	12.273	0.78	2.267	2,5
II-39	17 17 21.66	+43 11 03.2	15.20	14.38	12.623	12.115	12.000	0.82	2.380	2,5
II-53	17 17 13.07	+43 09 48.3	13.53	12.35	10.311	9.700	9.600	1.18	2.750	1,2,3,4,5
II-77	17 17 20.35	+43 10 28.3	14.95	14.21	12.453	12.014	11.890	0.74	2.320	1,3,4
II-120	17 17 18.92	+43 09 29.8	15.33	14.59	13.001	12.583	12.447	0.74	2.143	2,5
II-121	17 17 18.24	+43 09 31.3	14.50	13.79	12.129	11.687	11.594	0.71	2.196	1,3,4
III-4	17 17 19.68	+43 14 42.3	14.91	14.18	12.542	12.069	11.985	0.73	2.195	1,2,3,4,5
III-11	17 17 19.09	+43 12 54.7	15.92	15.23	13.642	13.192	13.135	0.69	2.095	1,2,3,4,5
III-65	17 17 14.13	+43 10 46.2	13.68	12.49	10.273	9.674	9.571	1.19	2.919	1,3,4
III-96	17 17 11.23	+43 10 10.3	15.77	15.08	13.618	13.110	13.105	0.69	1.975	2,5
III-109	17 17 07.22	+43 10 34.1	15.65	14.93	13.613	13.085	13.087	0.72	1.843	2,5
IV-2	17 16 58.84	+43 15 11.6	14.49	13.58	11.692	11.109	11.023	0.91	2.557	2,5
IV-10	17 16 57.73	+43 14 11.6	14.37	13.42	11.534	10.968	10.865	0.95	2.555	1,3,4
IV-13	17 17 03.99	+43 13 57.9	16.07	15.38	13.848	13.345	13.268	0.69	2.112	2,5
IV-40	17 17 00.33	+43 11 47.8	14.74	13.94	12.123	11.609	11.555	0.80	2.385	1,3,4
IV-79	17 17 00.82	+43 10 25.2	14.39	13.47	11.571	11.006	10.920	0.92	2.550	1,3,4
IV-94	17 17 05.88	+43 10 17.2	14.02	13.06	11.155	10.626	10.507	0.96	2.553	1,3,4
IV-114	17 16 59.63	+43 13 30.9	14.74	13.87	12.036	11.497	11.400	0.87	2.470	1,3,4
V-69	17 16 54.72	+43 10 26.3	15.36	14.60	13.003	12.524	12.433	0.76	2.167	1,3,4
V-78	17 16 56.53	+43 10 31.5	15.08	14.48	12.941	12.500	12.410	0.60	2.070	2,5
VI-18	17 16 37.72	+43 08 41.2	14.63	13.77	11.976	11.443	11.399	0.86	2.371	1,2,3,4,5
VII-10	17 16 34.28	+43 07 36.3	14.54	13.70	11.948	11.407	11.340	0.84	2.360	1,2 3,4,5
VII-18	17 16 37.49	+43 06 15.6	13.49	12.19	9.885	9.228	9.123	1.30	3.067	1,2,3,4,5
VII-39	17 16 43.95	+43 07 31.9	15.22	14.48	12.811	12.334	12.214	0.74	2.266	1,3,4
VII-66	17 16 48.67	+43 06 24.1	15.81	15.09	13.602	13.075	13.081	0.72	2.009	2,5
VII-67	17 16 47.91	+43 06 16.0	15.42	14.70	13.085	12.532	12.481	0.72	2.219	1,3,4
VII-79	17 16 51.18	+43 06 43.5	14.94	14.21	12.440	11.951	11.843	0.73	2.367	1,3,4
VII-80	17 16 51.88	+43 06 37.2	14.63	13.92	12.203	11.724	11.610	0.71	2.310	2,5
VII-122	17 16 57.38	+43 07 23.7	13.47	12.29	10.280	9.683	9.565	1.18	2.725	1,3,4
VII-123	17 16 56.59	+43 07 23.0	15.08	14.32	12.932	12.408	12.338	0.76	1.982	2,5
VIII-12	17 16 43.31	+43 04 16.1	15.47	14.76	13.091	12.618	12.504	0.71	2.256	1,2,3,4,5
VIII-24	17 16 50.35	+43 05 53.1	14.87	14.13	12.446	11.969	11.908	0.74	2.222	1,3,4
VIII-43	17 16 56.01	+43 04 47.9	15.37	14.62	12.980	12.481	12.412	0.75	2.208	2,5
VIII-44	17 16 55.52	+43 05 03.5	14.89	14.06	12.342	11.795	11.688	0.83	2.372	1,3,4
IX-2	17 16 55.20	+43 01 58.9	15.46	14.69	13.066	12.549	12.515	0.77	2.175	1,3,4
IX-6	17 16 59.68	+43 01 05.8	15.47	14.65	12.947	12.434	12.361	0.82	2.289	1,2,3,4,5
IX-10	17 17 03.95	+43 02 03.1	15.38	14.64	12.987	12.466	12.409	0.74	2.231	1,2,4,5
IX-12	17 16 52.84	+43 03 29.5	15.13	14.54	13.158	12.740	12.715	0.59	1.825	1,2,3,4,5
IX-49	17 17 00.44	+43 05 11.7	14.73	13.89	12.048	11.545	11.423	0.84	2.467	1,2,4,5
IX-77	17 17 05.77	+43 05 45.7	14.98	14.19	12.490	11.970	11.896	0.79	2.294	1,3,4
IX-89	17 17 06.47	+43 06 02.9	14.92	14.18	12.457	11.931	11.829	0.74	2.351	2,5
X-3	17 17 12.22	+43 02 20.9	15.36	14.63	12.965	12.453	12.393	0.73	2.237	2,5
X-28	17 17 15.52	+43 04 59.4	15.34	14.62	12.975	12.480	12.355	0.72	2.265	2,5
X-49	17 17 12.80	+43 05 42.0	13.35	12.16	10.002	9.330	9.232	1.19	2.928	1,3,4
X-65	17 17 11.41	+43 06 02.7	15.14	14.42	12.819	12.413	12.295	0.72	2.125	2,5

Table 7.3 (cont'd)

ID No. [a]	RA(2000) [b]	Dec(2000) [b]	B	V	J	H	K	B−V	V−K	Obs. [c]
XI-13	17 17 23.78	+43 04 41.4	15.36	14.82	13.556	13.285	13.125	0.54	1.695	2,5
XI-14	17 17 22.21	+43 04 50.0	14.68	13.81	11.988	11.436	11.359	0.87	2.451	1,3,4
XI-19	17 17 18.75	+43 04 51.0	13.92	12.87	10.856	10.312	10.179	1.05	2.691	1,3,4
XI-29	17 17 21.03	+43 06 12.8	15.02	14.40	13.081	12.636	12.545	0.62	1.855	2,5
XI-38	17 17 17.93	+43 05 44.0	15.35	14.59	12.982	12.512	12.416	0.76	2.174	1,3
XI-70	17 17 17.90	+43 06 50.9	14.86	14.11	12.376	11.831	11.768	0.75	2.342	1,3,4
XI-80	17 17 14.67	+43 06 24.9	14.04	13.04	10.966	10.382	10.286	1.00	2.754	1,3,4
XII-5	17 17 37.01	+43 06 45.8	15.64	14.88	13.226	12.684	12.664	0.76	2.216	1,2,3,4,5
XII-7	17 17 34.12	+43 06 16.1	15.38	14.63	13.031	12.522	12.437	0.75	2.193	1,3,4
XII-8	17 17 31.72	+43 05 41.5	13.82	12.76	10.726	10.126	10.041	1.06	2.719	1,3,4
XII-18	17 17 22.38	+43 06 56.3	15.08	14.36	12.940	12.495	12.392	0.72	1.968	2,5
XII-31	17 17 22.72	+43 07 47.4	14.80	13.95	12.179	11.680	11.560	0.85	2.39	2,5
XII-34	17 17 21.57	+43 07 40.9	14.34	13.45	11.601	11.066	10.994	0.89	2.456	1,3,4
XII-45	17 17 20.61	+43 07 26.0	14.84	14.08	12.308	11.769	11.686	0.76	2.394	2,5

[a]Sandage & Walker (1966)

[b]2MASS coordinates (Skrutskie et al., 2006)

[c]Observations: 1: 2006 May 7 (OB25), 2: 2006 May 9 (OB25), 3: 2006 May 7 (RV31), 4: 2006 May 8 (Ca41), 5: 2006 May 9 (Ca41).

Note. — The visual photometry is taken from Cudworth (1976), J,H,K photometry is taken from the 2MASS Catalog (Skrutskie et al., 2006).

Table 7.4. Physical Parameters of Cluster Members in M15

ID No.	M_V	$(B-V)_0$	$(V-K)_0$	P [a]	T_{eff} (K)	$logL/L_\odot$	$R/R_\odot$
B5	−1.86	1.02	2.595	99	4490	2.850	42.9
B6	−1.83	1.05	2.605	98	4480	2.840	42.6
B16	−1.61	0.99	2.455	0	4610	2.724	35.2
B30	−1.68	1.01	2.605	99	4480	2.780	39.7
C3	−0.72	0.74	2.335	97	4730	2.348	21.7
C20	+0.09	0.79	2.195	97	4870	2.004	13.8
C35	−0.23	0.53	2.015	0	5090	2.109	14.2
GEB 254	−2.13	1.21	3.195	···	4080	3.052	65.5
GEB 289	−1.87	0.94	2.845	···	4300	2.864	47.5
K12	−0.32	0.69	1.925	99	5200	2.135	14.0
K21	−0.37	0.64	1.995	72	5110	2.163	15.0
K22	−0.96	0.91	2.325	96	4740	2.443	24.1
K26	−0.37	0.77	2.155	92	4920	2.182	16.5
K27	−0.28	0.65	1.925	88	5200	2.119	13.8
K31	−0.16	0.73	2.055	76	5040	2.086	14.1
K42	−0.14	0.77	2.065	85	5020	2.079	14.1
K47	−1.26	0.92	2.345	99	4720	2.566	28.0
K56	+0.00	0.80	2.125	93	4950	2.030	13.7
K60	−0.11	0.71	2.055	86	5040	2.066	13.8
K64	−0.12	0.76	2.095	75	4990	2.074	14.2
K69	−0.92	0.81	2.325	99	4740	2.427	23.6
K70	−1.05	0.85	2.395	3	4670	2.490	26.2
K77	−1.55	1.00	2.515	99	4560	2.711	35.4
K87	−1.57	0.97	2.455	99	4610	2.708	34.5
K89	−0.84	0.72	2.305	99	4760	2.392	22.5
K92	−0.17	0.84	2.135	95	4940	2.100	14.9
K105	−0.08	0.87	2.075	89	5010	2.056	13.8
K112	−0.29	0.78	2.215	94	4850	2.158	16.6
K114	−1.52	1.04	2.495	99	4580	2.695	34.5
K129	−1.11	0.87	2.365	99	4700	2.509	26.4
K133	−0.27	0.79	1.925	82	5200	2.115	13.7
K136	−0.37	0.70	2.015	53	5090	2.165	15.2
K137	+0.01	0.88	2.045	93	5050	2.016	13.0
K144	−2.31	1.24	2.845	99	4300	3.083	61.1
K145	−0.01	0.78	2.125	83	4950	2.034	13.8
K146	−1.80	1.02	2.565	99	4520	2.820	40.9
K151	−0.26	0.79	2.335	92	4730	2.164	17.5
K152	−0.12	0.76	2.095	76	4990	2.074	14.2
K153	+0.11	0.65	2.135	62	4940	1.988	13.1
K158	−1.21	0.78	2.075	99	5010	2.508	23.2
K202	−0.20	0.79	2.055	64	5040	2.102	14.4
K224	−1.98	1.10	2.605	99	4480	2.900	45.6
K238	−2.13	1.18	2.665	99	4390	2.972	51.6
K255	−1.61	0.99	2.455	99	4610	2.724	35.2
K260	−1.38	0.70	1.665	99	5590	2.536	19.3
K272	−1.89	1.09	2.595	99	4460	2.862	44.1
K288	−1.66	1.04	2.465	99	4600	2.746	36.2
K328	−1.67	1.06	2.525	99	4550	2.760	37.6
K337	−0.61	0.89	2.285	92	4780	2.297	20.0

Table 7.4 (cont'd)

ID No.	M_V	$(B-V)_0$	$(V-K)_0$	P [a]	T_{eff} (K)	$logL/L_\odot$	$R/R_\odot$
K341	−2.56	1.27	2.845	99	4300	3.183	68.6
K361	−1.41	0.91	2.325	99	4740	2.623	29.6
K393	−2.12	1.11	2.665	99	4430	2.967	50.4
K421	−2.65	1.10	2.795	99	4330	3.207	69.5
K431	−2.34	1.20	2.715	99	4390	3.066	57.5
K447	−2.12	0.97	2.505	99	4570	2.937	45.7
K462	−2.47	1.45	2.905	99	4260	3.161	68.1
K476	−0.74	0.82	2.225	98	4840	2.340	20.5
K479	−2.69	1.21	2.885	99	4270	3.244	74.6
K482	−0.99	0.77	2.035	99	5060	2.415	20.5
K506	−0.62	0.77	2.245	99	4820	2.295	19.6
K550	−0.27	0.80	2.085	93	5000	2.133	15.1
K567	−2.32	1.11	2.565	99	4520	3.028	51.9
K582	−0.89	0.74	1.905	99	5230	2.361	18.0
K583	−2.54	1.33	2.985	99	4200	3.210	74.2
K647	−1.77	1.09	2.635	99	4460	2.821	42.0
K654	−0.21	0.80	2.105	89	4980	2.112	14.9
K672	−1.53	0.90	2.355	99	4710	2.676	31.9
K677	−0.37	0.72	1.915	98	5220	2.154	14.2
K691	−0.57	0.74	2.305	99	4760	2.284	19.9
K702	−2.38	1.38	2.805	99	4330	3.102	61.6
K709	−1.76	1.04	2.485	99	4590	2.789	38.2
K736	−1.36	0.91	2.385	99	4680	2.613	30.0
K757	−2.49	1.33	3.005	99	4190	3.195	73.2
K800	−0.25	1.01	2.085	65	5000	2.125	15.0
K825	−2.58	1.24	3.085	99	4140	3.253	80.2
K846	−1.40	0.98	2.445	99	4620	2.638	31.7
K853	−2.49	1.29	2.875	99	4280	3.162	67.6
K866	−0.67	0.92	2.155	86	4920	2.302	19.0
K875	−1.27	0.85	2.325	99	4740	2.567	27.8
K879	−1.21	0.96	2.355	98	4710	2.547	27.5
K902	−0.53	0.96	2.205	97	4860	2.253	18.4
K906	+0.00	0.77	2.085	88	5000	2.025	13.4
K919	−1.77	1.10	2.565	99	4520	2.808	40.3
K925	−0.75	0.89	2.275	96	4790	2.351	21.2
K926	−0.19	0.61	1.795	84	5390	2.070	12.1
K932	−1.28	0.95	2.375	99	4690	2.579	28.8
K947	−1.08	0.87	2.405	99	4660	2.504	26.7
K954	−1.04	0.89	2.335	99	4730	2.476	25.1
K969	−1.92	1.06	2.475	99	4590	2.851	41.1
K979	−1.14	0.76	2.055	99	5040	2.478	22.2
K989	−0.24	0.79	1.905	73	5230	2.101	13.3
K993	−1.36	0.90	2.475	99	4590	2.627	31.7
K1010	−0.40	0.81	2.155	97	4920	2.194	16.8
K1014	−0.67	0.81	2.065	98	5020	2.291	18.0
K1029	−1.81	1.08	2.685	99	4420	2.848	44.1
K1030	−1.23	0.93	2.465	99	4600	2.574	29.7
K1033	−0.93	0.87	2.395	99	4670	2.442	24.8
K1040	−1.97	1.10	2.685	99	4420	2.912	47.5

Table 7.4 (cont'd)

ID No.	M_V	$(B-V)_0$	$(V-K)_0$	P [a]	T_{eff} (K)	$logL/L_\odot$	$R/R_\odot$
K1049	−0.81	0.87	2.355	0	4710	2.387	22.9
K1054	−1.17	0.89	2.405	99	4660	2.540	27.9
K1056	−0.58	0.82	2.285	94	4780	2.285	19.7
K1069	−0.77	0.72	2.325	99	4740	2.367	22.1
K1073	−1.19	0.91	2.445	99	4620	2.554	28.8
K1074	−0.11	0.86	2.195	88	4870	2.084	15.1
K1079	−1.28	0.90	2.405	99	4660	2.584	29.3
K1083	+0.06	0.66	2.165	66	4910	2.012	13.7
K1084	−0.95	0.87	2.375	99	4690	2.447	24.7
K1097	+0.04	0.70	2.115	50	4970	2.013	13.3
K1106	−0.66	0.73	2.395	96	4670	2.334	21.9
K1136	−0.50	0.73	2.265	79	4800	2.250	18.8

[a]Membership probability from proper motion observations (Cudworth, 1976).

Table 7.5. Physical Parameters of Cluster Members in M13

ID No.	M_V	$(B-V)_0$	$(V-K)_0$	P [a]	T_{eff} (K)	$logL/L_\odot$	$R/R_\odot$
III-65	+0.74	0.80	2.095	99	5010	1.750	9.7
K188	−1.09	1.03	2.635	99	4470	2.575	31.5
K210	−0.15	0.86	2.305	99	4790	2.138	16.6
K220	+0.50	0.74	2.095	99	5010	1.846	10.8
K223	+0.23	0.83	2.165	99	4900	1.964	13.0
K224	+0.04	0.82	2.245	99	4790	2.052	15.0
K228	−1.17	1.04	2.645	99	4470	2.609	32.8
K246	−0.35	0.91	2.415	0	4680	2.237	19.5
K272	+0.99	0.76	2.085	99	5000	1.649	8.7
K342	+0.54	0.80	2.065	99	5020	1.826	10.5
K366	+0.38	0.78	2.245	99	4810	1.916	12.7
K422	−0.46	0.95	2.395	99	4670	2.277	20.5
K517	+0.89	0.74	2.125	99	4950	1.694	9.3
K549	+0.24	0.86	2.195	99	4870	1.965	13.2
K585	+0.36	0.86	2.175	99	4890	1.914	12.3
K647	+0.23	0.88	2.165	99	4900	1.964	13.0
K650	+0.35	0.82	2.135	99	4940	1.912	12.0
K652	+0.60	0.78	2.105	98	4970	1.808	10.5
K656	−1.44	1.10	2.795	99	4330	2.750	41.1
K658	+0.23	0.96	2.205	99	4860	1.970	13.3
K666	+0.38	0.82	2.195	99	4870	1.909	12.3
K674	−0.22	0.78	2.055	99	5030	2.129	14.9
K695	+0.44	0.87	2.145	99	4920	1.877	11.6
L4	+0.34	0.82	2.195	99	4870	1.925	12.6
L12	+0.47	0.78	2.075	99	5010	1.855	10.9
L13	+0.34	0.83	2.205	99	4860	1.926	12.6
L18	−0.70	0.91	2.515	99	4560	2.395	24.6
L19	+0.86	0.67	2.175	99	4890	1.714	9.8
L20	+0.26	0.82	2.155	99	4910	1.951	12.7
L22	+0.45	0.79	2.185	99	4880	1.879	11.9
L26	−0.90	0.99	2.535	99	4540	2.479	27.4
L29	+0.03	0.82	2.265	99	4790	2.059	15.2
L31	+0.26	0.81	2.175	99	4890	1.954	12.9
L32	+0.64	0.75	2.125	99	4950	1.794	10.5
L34	+0.48	0.80	2.125	99	4950	1.858	11.3
L38	+0.24	0.80	2.215	99	4850	1.968	13.3
L43	−0.89	0.97	2.345	99	4710	2.440	24.3
L70	−2.36	1.57	3.535	99	3910	3.345	99.9
L72	−2.16	1.28	3.025	99	4180	3.096	65.7
L80	+0.39	0.75	2.105	99	4970	1.892	11.6
L91	+0.29	0.83	2.165	99	4900	1.940	12.6
L93	+0.37	0.77	2.145	99	4920	1.905	12.0
L95	+0.28	0.79	2.185	99	4880	1.920	12.4
L96	−1.96	1.25	3.005	99	4190	3.010	59.1
L101	+0.61	0.73	2.005	99	5090	1.790	9.8
L102	+0.34	0.80	2.205	99	4860	1.926	12.6
L109	−1.16	0.93	2.455	99	4610	2.568	29.3
L110	+0.02	0.85	2.215	99	4850	2.056	14.7
L115	+0.24	0.77	2.175	99	4890	1.962	13.0

Table 7.5 (cont'd)

ID No.	M_V	$(B-V)_0$	$(V-K)_0$	P [a]	T_{eff} (K)	$logL/L_\odot$	$R/R_\odot$
L137	+0.10	0.84	2.215	99	4850	2.024	14.1
L140	−0.24	0.66	1.945	99	5170	2.123	14.0
L158	−1.78	1.17	2.915	99	4250	2.915	51.5
L168	−0.86	0.88	2.305	99	4750	2.421	23.3
L169	−1.70	1.14	2.835	99	4310	2.863	47.2
L180	+0.32	0.75	2.065	99	5017	1.914	11.6
L199	−2.28	1.37	3.205	99	4080	3.196	77.3
L219	+0.07	0.84	2.275	99	4780	2.045	14.9
L239	+0.30	0.82	2.185	99	4880	1.939	12.7
L250	−2.11	1.33	3.105	99	4130	3.098	67.4
L252	−1.81	1.20	2.975	99	4210	2.942	54.2
L255	+0.89	0.71	1.975	99	5130	1.674	8.5
L271	+0.39	0.79	2.185	99	4880	1.903	12.1
L316	−1.90	1.21	3.015	99	4190	2.989	57.7
L327	−0.70	0.73	2.245	99	4810	2.348	20.9
L330	+0.30	0.79	2.125	99	4950	1.930	12.2
L345	−1.60	1.19	2.765	99	4360	2.807	43.2
L373	−0.28	0.72	1.975	99	5130	2.142	14.5
L384	−2.00	1.26	2.885	99	4270	2.995	56.0
L395	+0.45	0.77	2.075	99	5000	1.863	11.0
L403	−1.29	1.03	2.705	99	4400	2.670	36.2
L414	−2.34	1.45	3.345	99	4000	3.266	87.2
L423	−0.17	0.84	2.315	99	4740	2.147	17.1
L436	−1.05	0.83	2.515	99	4560	2.535	28.9
L444	+0.24	0.78	2.145	99	4920	1.957	12.7
L465	−1.98	1.29	2.865	99	4290	2.982	54.6
L469	+0.13	0.83	2.215	99	4850	2.012	14.0
L530	+0.11	0.76	2.215	99	4850	2.020	14.1
L549	−1.90	1.05	2.525	99	4550	2.877	43.0
L592	−1.38	1.04	2.625	99	4460	2.689	36.0
L598	−2.48	1.62	3.615	99	3880	3.425	111.0
L637	+0.21	0.86	2.155	99	4910	1.971	13.0
L648	+0.17	0.62	1.805	99	5360	1.943	10.5
L691	+0.40	0.72	2.115	99	4960	1.889	11.6
L719	+0.21	0.74	2.025	99	5070	1.953	11.9
L726	−0.80	0.96	2.525	99	4550	2.437	25.9
L745	−1.94	1.26	3.135	99	4110	3.039	63.6
L756	−0.64	0.79	2.275	99	4780	2.329	20.7
L773	−1.27	0.98	2.605	99	4480	2.641	33.8
L828	+0.49	0.73	2.045	99	5040	1.843	10.6
L835	−2.39	1.45	3.275	99	4040	3.263	85.1
L846	+0.11	0.69	1.735	99	5470	1.960	10.3
L863	−1.50	1.16	2.695	99	4410	2.751	39.6
L867	+0.30	0.76	2.145	99	4920	1.933	12.4
L869	+0.14	0.82	2.165	99	4900	2.000	13.5
L883	+0.21	0.80	2.155	99	4910	1.971	13.0
L920	−0.76	0.84	2.305	99	4750	2.382	22.3
L954	−2.39	1.52	3.465	99	3940	3.329	96.6
L955	−0.56	0.88	2.485	99	4580	2.333	22.7

Table 7.5 (cont'd)

ID No.	M_V	$(B-V)_0$	$(V-K)_0$	P [a]	T_{eff} (K)	$logL/L_\odot$	$R/R_\odot$
L961	−1.09	0.89	2.365	99	4690	2.524	26.9
L965	+0.18	0.80	2.155	99	4910	1.983	13.2
L973	−2.44	1.59	3.535	99	3910	3.377	103.0
L987	+0.59	0.11	0.155	99	8940	1.746	3.0
L1005	+0.33	0.74	2.185	99	4880	1.927	12.5
L1009	+0.11	0.79	2.125	99	4950	2.006	13.3
L1011	+0.25	0.77	2.175	99	4890	1.958	12.9
L1023	−1.49	1.10	2.655	99	4440	2.739	38.5
L1024	+0.39	0.73	2.245	99	4810	1.912	12.6
L1025	+0.78	0.74	2.155	99	4910	1.743	10.0
L1032	−0.67	0.90	2.415	99	4650	2.365	22.8
L1043	−0.99	0.82	2.205	99	4860	2.458	23.3
L1048	−0.25	0.97	2.325	99	4730	2.181	17.8
L1050	−0.19	0.89	2.345	99	4710	2.160	17.6
L1065	+0.16	0.80	2.235	99	4830	2.003	13.9
L1073	−1.60	0.99	2.695	99	4410	2.791	41.5
L1077	+0.83	0.67	2.065	98	5020	1.710	9.2
L1080	+0.28	0.82	2.165	99	4900	1.944	12.6
L1091	+0.31	0.82	2.175	99	4890	1.934	12.5
L1097	−0.08	0.90	2.285	99	4770	2.107	16.1
L1102	+0.97	0.77	2.135	99	4940	1.664	9.0
L1103	+0.74	0.72	1.965	99	5140	1.733	9.0
L1114	−0.36	0.72	2.165	99	4900	2.200	17.0
L1115	+0.54	0.84	2.055	99	5030	1.825	10.4
L1118	+0.36	0.90	2.165	99	4900	1.912	12.2

[a]Membership probability from proper motion observations (Cudworth & Monet, 1979).

Table 7.6. Physical Parameters of Cluster Members in M92

ID No.	M_V	$(B-V)_0$	$(V-K)_0$	P [a]	T_{eff} (K)	$logL/L_\odot$	$R/R_\odot$
I-14	+0.10	0.71	2.093	99	4980	2.006	13.5
I-40	+0.14	0.71	2.085	99	4990	1.989	13.2
I-67	−1.32	0.90	2.499	99	4570	2.640	33.4
I-68	−0.03	0.73	1.894	99	5240	2.033	12.6
II-6	+0.50	0.73	2.093	99	4980	1.846	11.3
II-24	−0.10	0.76	2.212	99	4850	2.103	16.0
II-39	−0.26	0.80	2.325	99	4730	2.185	18.4
II-53	−2.29	1.16	2.695	99	4410	3.067	58.6
II-77	−0.43	0.72	2.265	99	4790	2.243	19.2
II-120	−0.05	0.72	2.088	99	4990	2.065	14.4
II-121	−0.85	0.69	2.141	99	4930	2.393	21.6
III-4	−0.46	0.71	2.140	99	4930	2.237	18.0
III-11	+0.59	0.67	2.040	99	5050	1.803	10.4
III-65	−2.15	1.17	2.864	99	4290	3.050	60.7
III-96	+0.44	0.67	1.920	99	5200	1.848	10.4
III-109	+0.29	0.70	1.788	99	5390	1.893	10.1
IV-2	−1.06	0.89	2.502	99	4570	2.536	29.6
IV-10	−1.22	0.93	2.500	99	4570	2.600	31.9
IV-13	+0.74	0.67	2.057	97	5030	1.745	9.8
IV-40	−0.70	0.78	2.330	99	4730	2.362	22.6
IV-79	−1.17	0.90	2.495	99	4570	2.579	31.1
IV-94	−1.58	0.94	2.498	99	4570	2.744	37.6
IV-114	−0.77	0.85	2.415	99	4650	2.405	24.6
V-69	−0.04	0.74	2.112	99	4960	2.065	14.6
V-78	−0.16	0.58	2.015	99	5080	2.100	14.5
VI-18	−0.87	0.84	2.316	99	4740	2.428	24.3
VII-10	−0.94	0.82	2.305	99	4750	2.454	24.9
VII-18	−2.45	1.28	3.012	99	4190	3.208	76.3
VII-39	−0.16	0.72	2.211	92	4850	2.127	16.4
VII-66	+0.45	0.70	1.954	99	5160	1.848	10.5
VII-67	+0.06	0.70	2.164	99	4900	2.032	14.4
VII-79	−0.43	0.71	2.312	99	4750	2.251	19.7
VII-80	−0.72	0.69	2.255	99	4800	2.358	21.9
VII-122	−2.35	1.16	2.670	99	4430	3.086	59.3
VII-123	−0.32	0.74	1.927	99	5190	2.153	14.8
VIII-12	+0.12	0.69	2.201	99	4860	2.014	14.3
VIII-24	−0.51	0.72	2.167	99	4900	2.260	18.7
VIII-43	−0.02	0.73	2.153	99	4910	2.062	14.9
VIII-44	−0.58	0.81	2.317	99	4740	2.312	21.3
IX-2	+0.05	0.75	2.120	99	4950	2.030	14.1
IX-6	+0.01	0.80	2.234	99	4830	2.063	15.4
IX-10	+0.00	0.72	2.176	99	4890	2.058	14.9
IX-12	−0.10	0.57	1.770	99	5410	2.047	12.0
IX-49	−0.75	0.82	2.412	99	4650	2.396	24.3
IX-77	−0.45	0.77	2.239	99	4820	2.247	19.1
IX-89	−0.46	0.72	2.296	99	4760	2.260	19.9
X-3	−0.01	0.71	2.182	99	4880	2.063	15.1
X-28	−0.02	0.70	2.210	99	4850	2.071	15.4
X-49	−2.48	1.17	2.873	99	4280	3.184	71.2

Table 7.6 (cont'd)

ID No.	M_V	$(B-V)_0$	$(V-K)_0$	P [a]	T_{eff} (K)	$logL/L_\odot$	$R/R_\odot$
X-65	−0.22	0.70	2.070	99	5010	2.131	15.5
XI-13	+0.18	0.52	1.640	99	5620	1.923	9.7
XI-14	−0.83	0.85	2.396	99	4660	2.425	25.1
XI-19	−1.77	1.03	2.636	99	4460	2.847	44.5
XI-29	−0.24	0.60	1.800	99	5370	2.107	13.1
XI-38	−0.05	0.74	2.119	99	4950	2.070	14.8
XI-70	−0.53	0.73	2.287	99	4770	2.287	20.4
XI-80	−1.60	0.98	2.699	99	4410	2.792	42.7
XII-5	+0.24	0.74	2.161	95	4910	1.960	13.2
XII-7	−0.01	0.73	2.138	99	4930	2.056	14.6
XII-8	−1.88	1.04	2.664	99	4430	2.896	47.7
XII-18	−0.28	0.70	1.913	99	5210	2.135	14.4
XII-31	−0.69	0.83	2.335	99	4720	2.359	22.6
XII-34	−1.19	0.87	2.401	99	4660	2.570	29.6
XII-45	−0.56	0.74	2.339	99	4720	2.307	21.3

[a]Membership probability from proper motion observations (Cudworth, 1976).

Table 7.7. Radial Velocity of Cluster Members in M15

ID No.	$v_{\rm rad,1}$ [a] (km s^{-1})	$v_{\rm rad,2}$ [a] (km s^{-1})	$v_{\rm rad,3}$ [a] (km s^{-1})	$v_{\rm rad,4}$ [a] (km s^{-1})
B5	-109.1 ± 0.3	···	-102.3 ± 0.4	-108.4 ± 0.3
B6	-113.8 ± 0.3	-113.3 ± 0.3	-112.4 ± 0.3	-113.3 ± 0.4
B16	···	···	-103.4 ± 0.4	···
B30	-104.2 ± 0.3	-105.7 ± 0.3	-102.8 ± 0.4	-104.2 ± 0.3
C3	-102.3 ± 0.5	-101.3 ± 0.4	-101.2 ± 0.5	-101.1 ± 0.5
C20	-108.0 ± 0.6	-109.6 ± 0.7	-108.6 ± 0.6	-108.6 ± 0.7
C35	-106.8 ± 0.6	···	···	···
GEB 254	···	···	···	-100.7 ± 0.3
GEB 289	···	···	-100.4 ± 0.5	···
K12	-107.6 ± 0.8	-107.0 ± 0.6	-107.2 ± 0.8	-107.0 ± 0.9
K21	···	-112.0 ± 0.7	-111.0 ± 0.8	-112.9 ± 0.7
K22	-101.7 ± 0.4	-101.2 ± 0.3	-102.1 ± 0.4	-102.0 ± 0.4
K26	-104.0 ± 0.5	-104.0 ± 0.4	-104.0 ± 0.5	-103.7 ± 0.5
K27	···	-107.4 ± 0.6	-106.9 ± 0.7	-107.2 ± 0.8
K31	···	-105.3 ± 0.4	-105.5 ± 0.5	-105.8 ± 0.6
K42	···	···	-104.5 ± 0.7	-104.3 ± 0.8
K47	-102.9 ± 0.7	-102.0 ± 0.4	···	···
K56	-104.7 ± 0.7	-104.4 ± 0.5	-105.4 ± 0.7	-104.3 ± 0.7
K60	···	···	-109.5 ± 0.5	-109.2 ± 0.6
K64	-107.8 ± 0.8	-108.6 ± 0.6	-108.8 ± 0.7	-108.9 ± 0.7
K69	-102.7 ± 0.6	-103.1 ± 0.5	···	-103.1 ± 0.6
K70	-109.2 ± 0.4	···	···	···
K77	-104.7 ± 0.4	-103.7 ± 0.3	-104.2 ± 0.4	-104.3 ± 0.4
K87	···	···	···	-108.3 ± 0.4
K89	···	-109.5 ± 0.4	-109.8 ± 0.5	-109.8 ± 0.6
K92	-107.5 ± 0.9	-106.7 ± 0.3	-106.5 ± 0.5	-106.1 ± 0.6
K105	-112.3 ± 0.5	···	···	-112.2 ± 0.6
K112	···	···	···	-100.3 ± 0.5
K114	···	···	-113.2 ± 0.4	···
K129	···	···	-102.5 ± 0.4	···
K133	···	-104.3 ± 0.5	-104.6 ± 0.7	···
K136	···	···	···	-111.0 ± 0.7
K137	···	···	-111.5 ± 0.6	···
K144	···	-108.6 ± 0.3	···	-110.9 ± 0.3
K145	-110.7 ± 0.6	-110.7 ± 0.4	-111.1 ± 0.6	···
K146	···	-101.3 ± 0.3	···	···
K151	···	···	-94.1 ± 0.5	···
K152	-100.8 ± 0.6	-100.0 ± 0.4	-100.7 ± 0.4	···
K153	-110.3 ± 0.6	···	-109.9 ± 0.8	-111.0 ± 0.7
K158	···	-110.5 ± 0.5	···	···
K202	···	···	-99.4 ± 0.7	···
K224	-106.6 ± 0.3	-106.7 ± 0.3	-106.8 ± 0.4	···
K238	···	···	···	-102.0 ± 0.3
K255	-102.4 ± 0.3	-101.9 ± 0.4	···	···
K260	-96.5 ± 1.4	-98.7 ± 0.9	···	···
K272	···	···	-106.2 ± 0.4	···
K288	-105.2 ± 0.4	···	-104.4 ± 0.4	···
K328	···	-102.9 ± 0.3	···	-102.4 ± 0.4
K337	···	-107.2 ± 0.4	-107.8 ± 0.6	-107.8 ± 0.6

Table 7.7 (cont'd)

ID No.	$v_{\rm rad,1}$ [a] (km s^{-1})	$v_{\rm rad,2}$ [a] (km s^{-1})	$v_{\rm rad,3}$ [a] (km s^{-1})	$v_{\rm rad,4}$ [a] (km s^{-1})
K341	-111.8 ± 0.2	-111.3 ± 0.3	-110.9 ± 0.3	-110.9 ± 0.3
K361	···	···	-108.6 ± 0.5	···
K393	-96.4 ± 0.3	···	···	···
K421	···	···	-111.7 ± 0.3	···
K431	-107.0 ± 0.3	-105.8 ± 0.3	-107.1 ± 0.4	···
K447	···	-105.2 ± 0.3	···	···
K462	···	-113.4 ± 0.3	···	···
K476	···	-109.1 ± 0.5	···	···
K479	···	···	···	-122.5 ± 0.4
K482	···	···	-110.2 ± 0.5	···
K506	···	···	···	-103.5 ± 0.5
K550	···	-111.1 ± 0.5	-110.2 ± 0.7	-110.2 ± 0.7
K567	···	···	-93.42 ± 0.4	···
K582	-99.4 ± 0.7	···	···	···
K583	-109.2 ± 0.3	···	···	···
K647	···	···	···	-116.8 ± 0.4
K654	···	···	···	-109.5 ± 0.7
K672	···	···	-106.9 ± 0.5	···
K677	···	···	-104.9 ± 0.8	-105.2 ± 0.9
K691	-109.4 ± 0.4	-109.6 ± 0.4	···	···
K702	-116.7 ± 0.2	-117.9 ± 0.3	···	···
K709	···	···	-101.7 ± 0.4	-99.8 ± 0.4
K736	···	···	-99.7 ± 0.4	···
K757	-117.4 ± 0.3	-111.2 ± 0.3	···	···
K800	-104.4 ± 0.8	···	···	···
K825	···	···	-101.4 ± 0.4	···
K846	-105.5 ± 0.3	···	···	-104.6 ± 0.4
K853	-108.3 ± 0.3	-109.2 ± 0.3	···	···
K866	···	···	-109.6 ± 0.7	···
K875	-111.2 ± 0.4	-110.7 ± 0.4	···	···
K879	-103.8 ± 0.4	-104.2 ± 0.3	···	···
K902	···	···	-108.4 ± 0.6	-109.0 ± 0.7
K906	···	···	-106.3 ± 0.6	···
K919	-111.1 ± 0.3	-112.4 ± 0.3	···	···
K925	-108.4 ± 0.5	-108.1 ± 0.4	···	···
K926	···	···	···	-108.1 ± 1.0
K932	···	···	···	-107.8 ± 0.5
K947	···	-116.8 ± 0.4	···	···
K954	···	···	···	-104.1 ± 0.5
K969	-110.8 ± 0.4	···	···	-108.8 ± 0.5
K979	-111.2 ± 0.6	···	···	···
K989	···	···	-109.3 ± 0.6	···
K993	-112.7 ± 0.3	···	···	···
K1010	···	···	···	-108.3 ± 0.8
K1014	···	···	-115.4 ± 0.5	···
K1029	-101.6 ± 0.4	-102.1 ± 0.3	···	···
K1030	-100.1 ± 0.3	-101.1 ± 0.3	···	···
K1033	-111.4 ± 0.4	-111.7 ± 0.3	···	···
K1040	···	···	-100.2 ± 0.3	···

Table 7.7 (cont'd)

ID No.	$v_{\rm rad,1}$ [a] (km s^{-1})	$v_{\rm rad,2}$ [a] (km s^{-1})	$v_{\rm rad,3}$ [a] (km s^{-1})	$v_{\rm rad,4}$ [a] (km s^{-1})
K1049	-106.5 ± 0.7	···	···	···
K1054	-105.9 ± 0.4	-106.5 ± 0.4	···	···
K1056	···	···	···	-103.5 ± 0.6
K1069	···	···	···	-102.4 ± 0.4
K1073	-118.8 ± 0.4	-120.3 ± 0.4	-119.9 ± 0.5	-119.9 ± 0.5
K1074	-106.7 ± 0.5	···	-106.9 ± 0.6	-107.5 ± 0.7
K1079	-104.4 ± 0.4	-106.2 ± 0.3	···	···
K1083	-107.1 ± 0.6	-106.2 ± 0.6	-106.5 ± 0.7	···
K1084	-106.3 ± 0.4	-105.0 ± 0.4	-103.7 ± 0.5	···
K1097	-109.9 ± 0.5	-110.6 ± 0.5	-108.5 ± 0.6	-108.8 ± 0.6
K1106	···	-107.1 ± 0.4	-106.0 ± 0.5	···
K1136	-103.8 ± 0.5	-105.3 ± 0.4	-106.8 ± 0.5	-105.5 ± 0.6

[a]Observations: 1: 2005 May 22, 2: 2006 May 11, 3: 2006 October 4, 4: 2006 October 7.

Note. — Data taken on 2006 May 11 and on 2006 October 7 were corrected with a velocity offset of +1.9 km s^{-1} and +0.9 km s^{-1} respectively.

Table 7.8. Hα Bisector Velocity of Cluster Members in M15

ID No.	$v_{\rm bis,1}$ [a] (km s^{-1})	$v_{\rm bis,2}$ [a] (km s^{-1})	$v_{\rm bis,3}$ [a] (km s^{-1})	$v_{\rm bis,4}$ [a] (km s^{-1})
B5	-4.2 ± 1.1	···	-4.7 ± 0.7	-3.3 ± 0.7
B6	-1.8 ± 0.7	-4.2 ± 0.7	-6.1 ± 1.0	-5.5 ± 1.1
B16	···	···	-2.7 ± 0.7	···
B30	-4.1 ± 0.9	-2.5 ± 1.3	-2.5 ± 0.4	-2.4 ± 0.9
C3	-1.8 ± 1.0	-1.2 ± 0.7	-0.9 ± 0.5	$+0.3 \pm 0.7$
C20	$+0.5 \pm 1.3$	-0.4 ± 1.8	-0.5 ± 1.0	-0.2 ± 2.0
C35	-2.2 ± 0.6	···	···	···
GEB 254	···	···	···	-8.5 ± 0.9
GEB 289	···	···	-3.3 ± 0.6	···
K12	-0.5 ± 1.0	-1.7 ± 0.7	-0.6 ± 0.5	-2.5 ± 1.2
K21	···	-1.0 ± 0.8	-0.9 ± 0.4	-1.7 ± 0.5
K22	$+0.9 \pm 1.1$	-1.0 ± 1.0	-1.8 ± 0.3	$+0.1 \pm 0.6$
K26	$+0.1 \pm 0.8$	$+0.2 \pm 0.2$	$+0.0 \pm 1.5$	$+0.1 \pm 1.2$
K27	···	$+1.2 \pm 0.8$	-1.5 ± 0.8	-1.2 ± 0.5
K31	···	$+0.9 \pm 1.1$	-2.3 ± 0.6	-1.4 ± 1.3
K42	···	···	-0.4 ± 0.6	$+0.7 \pm 0.8$
K47	-1.5 ± 0.7	-0.7 ± 0.4	···	···
K56	-2.2 ± 0.9	$+2.1 \pm 0.7$	$+0.0 \pm 0.8$	-1.7 ± 0.9
K60	···	···	$+0.4 \pm 0.7$	$+1.0 \pm 0.4$
K64	$+0.5 \pm 1.0$	$+1.7 \pm 1.3$	-0.6 ± 0.5	$+0.2 \pm 0.6$
K69	-0.6 ± 0.5	-0.3 ± 0.3	···	$+0.4 \pm 0.7$
K70	-0.3 ± 0.8	···	···	···
K77	-1.8 ± 0.6	-1.8 ± 0.6	-2.1 ± 0.6	-2.2 ± 0.5
K87	···	···	···	-3.9 ± 1.3
K89	···	-0.7 ± 0.7	-1.6 ± 0.5	-0.8 ± 0.5
K92	-1.7 ± 1.2	$+1.1 \pm 0.5$	$+0.5 \pm 0.7$	-1.0 ± 1.2
K105	-2.7 ± 1.5	···	···	-2.0 ± 1.2
K112	···	···	···	$+0.9 \pm 1.6$
K114	···	···	-1.7 ± 0.4	···
K129	···	···	$+0.1 \pm 0.4$	···
K133	···	-0.8 ± 0.6	$+0.5 \pm 1.6$	···
K136	···	···	···	-2.9 ± 0.8
K137	···	···	$+1.5 \pm 1.3$	···
K144	···	-5.3 ± 1.3	···	-5.7 ± 0.9
K145	$+0.3 \pm 0.9$	-0.2 ± 0.6	-0.4 ± 1.2	···
K146	···	-2.5 ± 0.6	···	···
K151	···	···	$+0.9 \pm 0.8$	···
K152	-0.4 ± 1.0	-0.9 ± 0.8	$+0.2 \pm 1.1$	···
K153	$+0.0 \pm 1.0$	···	$+0.7 \pm 1.2$	-0.4 ± 1.5
K158	···	-11.1 ± 1.0	···	···
K202	···	···	$+0.1 \pm 0.8$	···
K224	-2.9 ± 0.4	-4.0 ± 0.6	-4.5 ± 0.9	···
K238	···	···	···	-3.1 ± 0.6
K255	-1.1 ± 1.8	-1.0 ± 0.5	···	···
K260	-3.0 ± 1.2	-10.6 ± 0.9	···	···
K272	···	···	-3.0 ± 1.6	···
K288	-0.91 ± 0.82	···	-2.7 ± 0.6	···
K328	···	-2.4 ± 0.6	···	-3.3 ± 1.3
K337	···	$+0.1 \pm 0.6$	-0.4 ± 1.2	$+2.9 \pm 1.6$

Table 7.8 (cont'd)

ID No.	$v_{\rm bis,1}$ [a] (km s^{-1})	$v_{\rm bis,2}$ [a] (km s^{-1})	$v_{\rm bis,3}$ [a] (km s^{-1})	$v_{\rm bis,4}$ [a] (km s^{-1})
K341	-3.2 ± 0.6	-6.9 ± 1.0	-6.2 ± 0.6	-6.3 ± 0.9
K361	···	···	-1.9 ± 0.4	···
K393	-2.0 ± 0.9	···	···	···
K421	···	···	-4.3 ± 0.7	···
K431	-4.2 ± 0.8	-5.0 ± 1.3	-5.7 ± 1.1	···
K447	···	-2.0 ± 0.6	···	···
K462	···	-3.6 ± 0.7	···	···
K476	···	-0.2 ± 0.5	···	···
K479	···	···	···	-0.7 ± 0.7
K482	···	···	-6.2 ± 1.2	···
K506	···	···	···	-0.6 ± 1.9
K550	···	-1.3 ± 1.1	$+1.6 \pm 0.4$	$+1.6 \pm 0.6$
K567	···	···	-5.7 ± 1.1	···
K582	-13.2 ± 1.6	···	···	···
K583	-6.0 ± 1.3	···	···	···
K647	···	···	···	-6.2 ± 0.8
K654	···	···	···	$+0.1 \pm 0.7$
K672	···	···	-4.6 ± 0.9	···
K677	···	···	-1.1 ± 1.5	-4.6 ± 1.9
K691	-1.2 ± 0.5	-0.6 ± 0.5	···	···
K702	-6.1 ± 0.8	-3.9 ± 0.9	···	···
K709	···	···	-3.1 ± 0.6	-4.2 ± 1.0
K736	···	···	-2.1 ± 0.3	···
K757	-2.8 ± 0.5	-8.9 ± 1.1	···	···
K800	$+1.6 \pm 0.6$	···	···	···
K825	···	···	$+0.2 \pm 0.9$	···
K846	-1.8 ± 0.5	···	···	-3.3 ± 1.2
K853	-1.8 ± 0.5	-2.2 ± 0.8	···	···
K866	···	···	-1.3 ± 0.4	···
K875	-7.2 ± 1.0	-4.4 ± 0.4	···	···
K879	-1.3 ± 0.5	-0.5 ± 0.6	···	···
K902	···	···	-0.4 ± 0.4	$+0.8 \pm 0.5$
K906	···	···	-0.9 ± 0.4	···
K919	-2.4 ± 0.5	-2.6 ± 0.8	···	···
K925	-0.7 ± 0.7	-0.4 ± 0.8	···	···
K926	···	···	···	$+0.6 \pm 0.7$
K932	···	···	···	-1.5 ± 1.2
K947	···	-1.0 ± 1.1	···	···
K954	···	···	···	-0.6 ± 0.8
K969	-4.0 ± 0.6	···	···	-1.7 ± 0.3
K979	-6.7 ± 1.3	···	···	···
K989	···	···	-0.4 ± 1.0	···
K993	-2.4 ± 0.9	···	···	···
K1010	···	···	···	-2.3 ± 1.6
K1014	···	···	$+1.1 \pm 0.9$	···
K1029	-2.9 ± 1.1	-3.0 ± 1.0	···	···
K1030	-1.3 ± 0.5	-2.6 ± 0.6	···	···
K1033	-0.9 ± 0.5	$+0.6 \pm 0.7$	···	···
K1040	···	···	-6.3 ± 1.4	···

Table 7.8 (cont'd)

ID No.	$v_{\rm bis,1}$ [a] (km s^{-1})	$v_{\rm bis,2}$ [a] (km s^{-1})	$v_{\rm bis,3}$ [a] (km s^{-1})	$v_{\rm bis,4}$ [a] (km s^{-1})
K1049	-1.2 ± 1.8	···	···	···
K1054	-1.5 ± 0.4	-1.1 ± 0.6	···	···
K1056	···	···	···	-0.4 ± 1.0
K1069	···	···	···	-1.5 ± 0.8
K1073	-3.6 ± 0.8	-0.7 ± 0.7	$+0.0 \pm 0.8$	-1.9 ± 0.9
K1074	-0.1 ± 0.9	···	-0.5 ± 1.6	-0.6 ± 1.1
K1079	-1.4 ± 0.4	-0.9 ± 0.7	···	···
K1083	-0.8 ± 1.6	-1.6 ± 1.6	$+1.5 \pm 1.2$	···
K1084	-0.7 ± 0.8	-0.6 ± 0.6	-1.1 ± 0.5	···
K1097	$+2.5 \pm 0.8$	$+0.6 \pm 0.8$	-1.0 ± 0.7	-1.1 ± 0.6
K1106	···	-0.2 ± 0.7	-1.7 ± 1.5	···
K1136	-1.0 ± 1.4	-0.2 ± 0.7	$+0.9 \pm 0.7$	-1.3 ± 1.0

[a]Observations: 1: 2005 May 22; 2: 2006 May 11; 3: 2006 October 4; 4: 2006 October 7.

Table 7.9. Radial and Hα Bisector Velocity of Observed Stars in M13

ID No.	$v_{\rm rad,1}$ [a] (km s^{-1})	$v_{\rm rad,2}$ [a] (km s^{-1})	$v_{\rm rad,3}$ [a] (km s^{-1})	$v_{\rm rad,4}$ [a] (km s^{-1})	$v_{\rm bis,1}$ [b] (km s^{-1})	$v_{\rm bis,2}$ [b] (km s^{-1})
III-65	-246.0 ± 0.4	···	-245.9 ± 0.2	···	$+0.5 \pm 2.5$	···
K188	-244.9 ± 0.3	···	-245.2 ± 0.2	···	-1.4 ± 1.0	···
K210	-250.8 ± 0.2	···	-249.9 ± 0.3	···	-0.0 ± 0.6	···
K220	-244.0 ± 0.3	-243.6 ± 0.2	···	-242.9 ± 0.2	$+0.4 \pm 1.4$	$+1.5 \pm 0.7$
K223	···	-242.6 ± 0.2	···	-242.0 ± 0.2	···	$+0.2 \pm 0.9$
K224	···	-247.6 ± 0.2	···	-247.2 ± 0.2	···	-0.7 ± 1.0
K228	-249.6 ± 0.3	···	-249.7 ± 0.2	···	-1.8 ± 0.8	···
K246	···	-249.2 ± 0.2	···	-249.2 ± 0.2	···	-0.9 ± 0.4
K272	-245.0 ± 0.4	···	-245.2 ± 0.3	···	-1.9 ± 1.5	···
K342	-256.2 ± 0.3	-255.6 ± 0.2	-256.6 ± 0.2	-256.0 ± 0.2	-2.0 ± 1.5	$+0.2 \pm 0.3$
K366	-249.4 ± 0.3	-249.1 ± 0.3	···	-248.8 ± 0.2	$+0.6 \pm 1.3$	-1.4 ± 0.4
K422	-247.4 ± 0.2	-246.6 ± 0.2	-247.8 ± 0.2	-246.7 ± 0.2	-0.3 ± 1.0	$+0.1 \pm 0.5$
K517	-247.4 ± 0.3	···	-248.4 ± 0.4	···	-1.3 ± 0.7	···
K549	···	-252.0 ± 0.2	-253.1 ± 0.2	-252.2 ± 0.2	···	-0.8 ± 0.6
K585	···	-247.3 ± 0.3	···	-247.2 ± 0.2	···	$+0.1 \pm 0.4$
K647	-246.2 ± 0.2	-245.8 ± 0.2	-246.6 ± 0.2	-246.0 ± 0.2	-0.8 ± 0.9	-0.1 ± 0.4
K650	···	-253.2 ± 0.2	···	-253.5 ± 0.2	···	$+0.9 \pm 0.5$
K652	···	-241.2 ± 0.2	···	-241.7 ± 0.2	···	$+0.8 \pm 0.8$
K656	-244.0 ± 0.3	···	···	···	-0.9 ± 0.5	···
K658	-253.2 ± 0.3	-252.0 ± 0.2	-252.8 ± 0.2	-252.1 ± 0.2	-4.2 ± 0.7	$+0.9 \pm 0.7$
K666	···	-248.1 ± 0.2	···	-248.3 ± 0.2	···	-1.1 ± 1.2
K674	-252.3 ± 0.3	···	-252.3 ± 0.2	···	-1.5 ± 0.7	···
K695	-248.5 ± 0.4	···	-248.6 ± 0.2	···	$+1.1 \pm 0.6$	···
L4	···	-257.0 ± 0.2	···	-256.7 ± 0.2	···	-0.5 ± 0.9
L12	-249.6 ± 0.3	-248.9 ± 0.2	-249.4 ± 0.2	-248.6 ± 0.2	-0.8 ± 0.6	$+1.0 \pm 0.8$
L13	-243.0 ± 0.3	-242.8 ± 0.2	···	···	-0.6 ± 1.0	$+0.7 \pm 0.4$
L18	-251.1 ± 0.2	···	-251.8 ± 0.2	···	$+3.1 \pm 1.0$	···
L19	-241.7 ± 0.3	-242.0 ± 0.3	-242.6 ± 0.2	···	$+0.7 \pm 0.8$	-0.2 ± 0.6
L20	···	-249.3 ± 0.2	-250.0 ± 0.2	-248.9 ± 0.2	···	-0.5 ± 1.3
L22	···	-245.9 ± 0.2	-245.9 ± 0.2	-245.0 ± 0.2	···	$+0.3 \pm 0.9$
L26	-242.5 ± 0.2	-242.8 ± 0.2	-242.7 ± 0.2	-242.0 ± 0.2	-0.8 ± 0.4	-0.9 ± 0.5
L29	···	-238.7 ± 0.2	···	-239.3 ± 0.1	···	$+1.0 \pm 0.7$
L31	···	-245.8 ± 0.2	···	-245.2 ± 0.2	···	$+1.5 \pm 1.0$
L32	-249.8 ± 0.3	···	-250.6 ± 0.2	···	-0.6 ± 1.2	···
L34	···	-239.8 ± 0.2	···	-239.2 ± 0.2	···	$+1.2 \pm 0.4$
L38	···	-246.3 ± 0.2	···	-246.2 ± 0.2	···	-0.2 ± 0.8
L43	-257.0 ± 0.3	-257.1 ± 0.2	-257.7 ± 0.2	-256.4 ± 0.2	$+0.5 \pm 0.4$	-0.5 ± 0.3
L70	-238.0 ± 0.3	···	-238.4 ± 0.2	···	$+0.4 \pm 0.3$	···
L72	-245.4 ± 0.3	-247.5 ± 0.3	-245.1 ± 0.2	···	-5.0 ± 0.6	-5.7 ± 0.8
L80	···	-234.8 ± 0.2	···	-224.1 ± 3.4	···	$+0.2 \pm 0.6$
L91	···	-253.9 ± 0.2	···	-253.9 ± 0.2	···	-0.4 ± 1.1
L93	···	-243.4 ± 0.2	···	···	···	$+0.3 \pm 0.5$
L95	···	-249.0 ± 0.2	···	-249.1 ± 0.2	···	$+1.0 \pm 0.7$
L96	-237.9 ± 0.4	···	-237.3 ± 0.2	···	-6.1 ± 0.9	···
L101	···	-238.2 ± 0.3	···	-237.6 ± 0.2	···	$+1.7 \pm 0.6$
L102	-244.3 ± 0.3	-244.0 ± 0.2	-245.1 ± 0.2	-243.6 ± 0.2	$+0.7 \pm 1.7$	$+0.5 \pm 0.5$
L109	-248.2 ± 0.2	···	-249.1 ± 0.2	···	-4.6 ± 0.6	···
L110	-242.8 ± 0.3	-242.5 ± 0.2	-243.0 ± 0.2	-242.4 ± 0.2	-1.7 ± 1.0	-0.2 ± 0.5
L115	···	-243.8 ± 0.2	···	-243.3 ± 0.2	···	-0.5 ± 0.3

Table 7.9 (cont'd)

ID No.	$v_{\rm rad,1}$ [a] (km s^{-1})	$v_{\rm rad,2}$ [a] (km s^{-1})	$v_{\rm rad,3}$ [a] (km s^{-1})	$v_{\rm rad,4}$ [a] (km s^{-1})	$v_{\rm bis,1}$ [b] (km s^{-1})	$v_{\rm bis,2}$ [b] (km s^{-1})
L137	-247.8 ± 0.3	-246.8 ± 0.2	-247.7 ± 0.2	-246.7 ± 0.2	$+0.6 \pm 1.6$	$+0.4 \pm 0.7$
L140	-240.4 ± 0.2	···	-240.6 ± 0.2	···	-1.7 ± 0.6	···
L158	-247.3 ± 0.3	···	-247.5 ± 0.2	···	-3.7 ± 0.9	···
L168	-247.9 ± 0.3	···	-248.4 ± 0.2	···	-3.2 ± 0.6	···
L169	-247.3 ± 0.3	···	···	···	-4.4 ± 0.6	···
L180	···	-248.5 ± 0.3	···	-248.2 ± 0.2	···	$+0.6 \pm 0.5$
L199	-250.7 ± 0.3	···	-250.8 ± 0.2	···	-0.5 ± 0.6	···
L219	···	-245.7 ± 0.2	···	-245.2 ± 0.2	···	$+1.6 \pm 0.7$
L239	···	-240.7 ± 0.2	···	···	···	-0.1 ± 0.6
L250	-250.7 ± 0.3	···	-250.8 ± 0.2	···	-4.0 ± 0.8	···
L252	-239.4 ± 0.3	···	-239.8 ± 0.2	···	-3.1 ± 0.5	···
L255	-250.5 ± 0.4	···	-251.1 ± 0.2	···	-1.3 ± 1.2	···
L271	···	-250.3 ± 0.2	···	-249.8 ± 0.2	···	-0.0 ± 0.6
L316	-239.7 ± 0.3	···	-240.2 ± 0.2	···	-4.2 ± 0.7	···
L327	···	-247.4 ± 0.3	···	-247.6 ± 0.2	···	-0.3 ± 0.5
L330	···	-243.7 ± 0.2	···	-243.5 ± 0.2	···	$+0.2 \pm 0.4$
L345	···	-249.6 ± 0.3	···	-249.1 ± 0.2	···	-2.5 ± 0.9
L373	-248.6 ± 0.3	···	-248.3 ± 0.2	···	-0.4 ± 1.3	···
L384	···	-245.0 ± 0.3	···	-245.3 ± 0.2	···	-1.9 ± 0.6
L395	···	-254.0 ± 0.2	···	-254.1 ± 0.2	···	-0.1 ± 0.9
L403	-249.8 ± 0.3	···	-249.9 ± 0.2	···	-1.4 ± 0.8	···
L414	-240.6 ± 0.3	···	-240.6 ± 0.2	···	-6.7 ± 0.9	···
L423	-239.9 ± 0.3	···	-239.5 ± 0.2	···	$+0.5 \pm 1.0$	···
L436	-234.6 ± 0.2	···	-234.6 ± 0.1	···	$+0.3 \pm 0.7$	···
L444	···	-239.1 ± 0.3	···	-239.0 ± 0.2	···	$+0.1 \pm 0.6$
L465	-251.5 ± 0.3	···	-251.4 ± 0.2	···	-4.2 ± 0.7	···
L469	-243.1 ± 0.3	···	-243.5 ± 0.2	···	$+0.9 \pm 0.9$	···
L530	···	-239.4 ± 0.2	···	-238.9 ± 0.2	···	-0.4 ± 0.5
L549	-255.8 ± 0.3	···	-255.5 ± 0.2	···	-1.2 ± 0.6	···
L592	···	-243.4 ± 0.2	···	-243.2 ± 0.2	···	-2.6 ± 0.3
L598	-257.3 ± 0.3	···	-257.7 ± 0.3	···	$+1.9 \pm 1.0$	···
L637	···	-245.1 ± 0.2	···	-245.0 ± 0.2	···	$+0.3 \pm 1.0$
L648	···	-247.3 ± 0.2	···	-246.8 ± 0.3	···	-0.4 ± 1.1
L691	···	-243.5 ± 0.2	···	-242.9 ± 0.2	···	$+2.0 \pm 0.9$
L719	-254.1 ± 0.3	-245.2 ± 0.2	···	-245.7 ± 0.2	-4.0 ± 0.9	$+0.7 \pm 0.7$
L726	-245.8 ± 0.2	···	-245.8 ± 0.2	···	$+0.4 \pm 0.3$	···
L745	-245.0 ± 0.3	···	-245.9 ± 0.2	···	-3.4 ± 0.8	···
L756	-262.7 ± 0.3	···	-262.9 ± 0.2	···	$+1.1 \pm 0.3$	···
L773	-238.2 ± 0.3	···	-239.2 ± 0.2	···	-5.9 ± 0.7	···
L828	···	-248.7 ± 0.2	···	-248.8 ± 0.2	···	-0.2 ± 0.6
L835	-261.1 ± 0.3	···	-261.4 ± 0.2	···	$+0.1 \pm 0.8$	···
L846	···	-242.0 ± 0.2	···	-241.7 ± 0.2	···	-0.6 ± 0.7
L863	-250.8 ± 0.3	···	-251.0 ± 0.2	···	-0.7 ± 0.2	···
L867	···	-249.0 ± 0.2	···	-248.4 ± 0.2	···	$+1.2 \pm 1.0$
L869	···	-248.4 ± 0.3	···	-248.9 ± 0.2	···	$+1.4 \pm 0.5$
L883	···	-244.0 ± 0.2	···	-243.9 ± 0.2	···	-0.1 ± 1.1
L920	-247.9 ± 0.2	···	-249.5 ± 0.2	···	-2.2 ± 0.8	···
L954	-251.8 ± 0.3	···	-252.0 ± 0.3	···	-1.8 ± 0.6	···
L955	···	-243.2 ± 0.2	···	-243.0 ± 0.2	···	$+0.4 \pm 0.4$

Table 7.9 (cont'd)

ID No.	$v_{\rm rad,1}$ [a] (km s^{-1})	$v_{\rm rad,2}$ [a] (km s^{-1})	$v_{\rm rad,3}$ [a] (km s^{-1})	$v_{\rm rad,4}$ [a] (km s^{-1})	$v_{\rm bis,1}$ [b] (km s^{-1})	$v_{\rm bis,2}$ [b] (km s^{-1})
L961	-259.2 ± 0.3	···	-259.1 ± 0.2	···	-5.4 ± 0.7	···
L965	···	-234.5 ± 0.2	···	-235.4 ± 0.2	···	-0.7 ± 0.6
L973	-245.7 ± 0.3	···	-245.9 ± 0.3	···	-1.9 ± 0.4	···
L987	-252.8 ± 0.3	···	···	···	$+0.4 \pm 1.1$	···
L1005	···	-237.8 ± 0.2	···	-238.3 ± 0.3	···	$+0.3 \pm 0.6$
L1009	···	-253.5 ± 0.2	···	-253.9 ± 0.2	···	$+0.6 \pm 0.9$
L1011	···	-249.7 ± 0.2	···	-250.1 ± 0.2	···	-0.2 ± 0.3
L1023	-247.5 ± 0.3	···	-247.4 ± 0.2	···	-0.9 ± 0.6	···
L1024	···	-244.8 ± 0.2	···	-244.6 ± 0.6	···	-0.8 ± 0.5
L1025	···	-257.1 ± 0.2	···	-257.1 ± 0.2	···	-1.2 ± 0.7
L1032	-249.0 ± 0.3	···	-249.0 ± 0.2	···	-0.6 ± 0.9	···
L1043	-246.5 ± 0.3	···	-247.0 ± 0.2	···	-6.8 ± 1.4	···
L1048	-251.3 ± 0.3	···	-251.7 ± 0.2	···	$+0.3 \pm 0.5$	···
L1050	-248.1 ± 0.2	···	-249.0 ± 0.2	···	-0.7 ± 1.0	···
L1065	···	-239.3 ± 0.2	···	-239.2 ± 0.2	···	-0.3 ± 0.3
L1073	-252.6 ± 0.3	···	-252.8 ± 0.2	···	-4.3 ± 1.1	···
L1077	···	-254.5 ± 0.2	···	-254.6 ± 0.3	···	$+1.4 \pm 0.8$
L1080	···	-242.1 ± 0.2	···	-242.0 ± 0.2	···	$+0.7 \pm 0.9$
L1091	···	-249.9 ± 0.2	···	-249.9 ± 0.2	···	$+0.4 \pm 0.9$
L1097	-258.5 ± 0.3	···	···	···	-0.2 ± 0.5	···
L1102	-249.5 ± 0.4	···	-250.5 ± 0.3	···	$+3.4 \pm 1.3$	···
L1103	···	-253.2 ± 0.3	···	-252.9 ± 0.2	···	-0.1 ± 0.5
L1114	-258.0 ± 0.2	···	-258.5 ± 0.3	···	-0.3 ± 0.9	···
L1115	-243.0 ± 0.3	···	-243.5 ± 0.4	···	-0.7 ± 1.3	···
L1118	-240.2 ± 0.3	-240.2 ± 0.2	-241.3 ± 0.2	-240.5 ± 0.2	-1.1 ± 1.0	$+0.4 \pm 0.7$

[a]Observations: 1: 2006 March 14 (OB25), 2: 2006 May 10 (OB25), 3: 2006 March 16 (RV31), 4: 2006 May 10 (RV31).

[b]Observations: 1: 2006 March 14; 2: 2006 May 10.

Table 7.10. Radial and Hα Bisector Velocity of Observed Stars in M92

ID No.	$v_{\rm rad,1}$ [a] (km s^{-1})	$v_{\rm rad,2}$ [a] (km s^{-1})	$v_{\rm rad,3}$ [a] (km s^{-1})	$v_{\rm bis,1}$ [b] (km s^{-1})	$v_{\rm bis,2}$ [b] (km s^{-1})
I-14	-124.2 ± 0.3	-124.0 ± 0.2	-123.9 ± 0.2	-0.5 ± 1.2	$+0.6 \pm 0.5$
I-40	-125.2 ± 0.2	···	-124.6 ± 0.2	$+0.5 \pm 0.5$	···
I-67	-120.9 ± 0.2	···	-120.2 ± 0.2	-1.8 ± 0.4	···
I-68	···	-129.7 ± 0.2	···	···	$+0.0 \pm 0.6$
II-6	-122.6 ± 0.3	-123.1 ± 0.3	-121.8 ± 0.2	$+2.5 \pm 0.7$	-1.8 ± 0.8
II-24	···	-121.4 ± 0.2	···	$+1.4 \pm 0.2$	···
II-39	···	-120.5 ± 0.2	···	-0.7 ± 0.6	···
II-53	-124.0 ± 0.2	-116.3 ± 0.6	-123.5 ± 0.1	-6.3 ± 0.9	-7.1 ± 1.1
II-77	-117.9 ± 0.2	···	-117.4 ± 0.2	$+1.2 \pm 0.6$	···
II-120	···	-115.1 ± 0.2	···	···	-0.8 ± 0.7
II-121	-109.0 ± 0.2	···	-108.2 ± 0.2	-2.8 ± 0.7	···
III-4	-121.2 ± 0.2	-120.4 ± 0.2	-120.3 ± 0.1	$+0.1 \pm 0.6$	-0.4 ± 0.5
III-11	-121.4 ± 0.4	-120.0 ± 0.3	-120.1 ± 0.2	$+0.3 \pm 0.8$	-0.5 ± 1.4
III-65	-118.5 ± 0.2	···	-118.0 ± 0.1	-5.8 ± 0.8	···
III-96	···	-114.9 ± 0.3	···	···	$+1.2 \pm 0.7$
III-109	···	-124.4 ± 0.3	···	···	$+0.9 \pm 0.7$
IV-2	···	-125.2 ± 0.2	···	···	-1.9 ± 0.3
IV-10	-119.9 ± 0.2	···	-119.6 ± 0.1	-0.4 ± 0.4	···
IV-13	···	-124.1 ± 0.3	···	···	-0.4 ± 0.7
IV-40	-117.8 ± 0.2	···	-117.6 ± 0.2	-2.3 ± 0.6	···
IV-79	-121.0 ± 0.2	···	-120.1 ± 0.2	-0.9 ± 1.0	···
IV-94	-118.9 ± 0.2	···	-118.3 ± 0.1	-2.3 ± 0.3	···
IV-114	-116.6 ± 0.2	···	-116.5 ± 0.2	-0.6 ± 0.7	···
V-69	-119.8 ± 0.3	···	-119.1 ± 0.2	$+0.7 \pm 0.7$	···
V-78	···	-126.0 ± 0.3	···	···	-0.8 ± 1.7
VI-18	-125.7 ± 0.2	-125.1 ± 0.2	-125.6 ± 0.6	-0.6 ± 0.4	-2.1 ± 0.2
VII-10	-120.4 ± 0.2	-120.3 ± 0.2	-120.2 ± 0.2	-2.4 ± 1.0	-1.4 ± 0.6
VII-18	-118.5 ± 0.2	-117.7 ± 0.2	-118.5 ± 0.1	-3.0 ± 1.0	-2.8 ± 0.8
VII-39	-109.1 ± 0.2	···	-108.4 ± 0.2	-0.3 ± 0.5	···
VII-66	···	-112.0 ± 0.3	···	···	$+1.3 \pm 0.7$
VII-67	-127.8 ± 0.3	···	-127.2 ± 0.2	-0.7 ± 0.5	···
VII-79	-116.1 ± 0.2	···	-115.8 ± 0.2	$+0.3 \pm 0.5$	···
VII-80	···	-125.3 ± 0.3	···	···	-2.2 ± 0.5
VII-122	-124.4 ± 0.2	···	-124.0 ± 0.1	-4.4 ± 0.7	···
VII-123	···	-122.6 ± 0.2	···	···	$+0.5 \pm 0.5$
VIII-12	-121.5 ± 0.3	-121.7 ± 0.3	-121.2 ± 0.1	$+2.1 \pm 0.6$	$+0.9 \pm 0.7$
VIII-24	-118.3 ± 0.2	···	-117.9 ± 0.2	-3.3 ± 0.8	···
VIII-43	···	-123.5 ± 0.2	···	···	$+0.8 \pm 0.4$
VIII-44	-119.1 ± 0.2	···	-118.4 ± 0.1	-0.5 ± 0.7	···
IX-2	-125.4 ± 0.2	···	-124.9 ± 0.2	$+0.7 \pm 0.4$	···
IX-6	-125.6 ± 0.2	-125.1 ± 0.2	-125.0 ± 0.2	-0.5 ± 0.8	$+0.2 \pm 0.8$
IX-10	-124.0 ± 0.2	-123.2 ± 0.2	···	$+0.6 \pm 0.5$	-0.4 ± 0.4
IX-12	-120.0 ± 0.6	-120.3 ± 0.6	-119.4 ± 0.3	-13.7 ± 0.9	-15.9 ± 1.3
IX-49	-128.3 ± 0.2	-127.6 ± 0.2		-0.9 ± 1.0	$+0.5 \pm 0.4$
IX-77	-131.9 ± 0.2	···	-131.4 ± 0.1	-0.9 ± 0.5	···
IX-89	···	-116.4 ± 0.2	···	···	$+0.1 \pm 0.6$
X-3	···	-123.9 ± 0.2	···	···	-0.3 ± 0.8
X-28	···	-118.1 ± 0.2	···	···	$+0.2 \pm 0.5$
X-49	-130.0 ± 0.2	···	-129.3 ± 0.1	-6.9 ± 0.8	···

Table 7.10 (cont'd)

ID No.	$v_{\rm rad,1}$ [a] (km s^{-1})	$v_{\rm rad,2}$ [a] (km s^{-1})	$v_{\rm rad,3}$ [a] (km s^{-1})	$v_{\rm bis,1}$ [b] (km s^{-1})	$v_{\rm bis,2}$ [b] (km s^{-1})
X-65	···	−121.9 ± 0.3	···	···	−2.2 ± 0.6
XI-13	···	−122.1 ± 0.7	···	···	−2.4 ± 0.9
XI-14	−120.6 ± 0.9	···	−120.9 ± 0.2	−0.0 ± 0.3	···
XI-19	−117.2 ± 0.1	···	−116.9 ± 0.1	−2.3 ± 1.2	···
XI-29	···	−119.8 ± 0.4	···	···	−2.3 ± 0.5
XI-38	−110.8 ± 0.3	···	−116.5 ± 0.2	−0.4 ± 0.9	···
XI-70	−129.4 ± 0.2	···	−128.6 ± 0.2	+0.4 ± 0.9	···
XI-80	−126.2 ± 0.2	···	−125.4 ± 0.1	−1.7 ± 0.4	···
XII-5	−119.8 ± 0.3	−119.3 ± 0.2	−118.8 ± 0.2	−0.5 ± 1.3	+0.4 ± 1.0
XII-7	−125.6 ± 0.2	···	−124.7 ± 0.2	+0.4 ± 0.4	···
XII-8	−118.7 ± 0.2	···	−118.2 ± 0.1	−5.6 ± 0.8	···
XII-18	···	−124.8 ± 0.3	···	−1.3 ± 0.4	···
XII-31	···	−116.1 ± 0.2	···	···	+0.0 ± 0.6
XII-34	−116.0 ± 0.2	···	−115.4 ± 0.2	−2.3 ± 1.3	···
XII-45	···	−118.8 ± 0.1	···	···	−0.6 ± 0.4

[a]Observations: 1: 2006 May 7 (OB25), 2: 2006 May 9 (OB25), 3: 2006 May 7 (RV31)

[b]Observations: 1: 2006 March 14; 2: 2006 May 10.